

Magneto-structural Transition and Magnetic Field Induced Effects in Fe-Rh Based Pseudobinary Alloys

By

M. A. Manekar

PHYS 03200704012

Raja Ramanna Centre for Advanced Technology, Indore

*A thesis submitted to the
Board of Studies in Physical Sciences*

*In partial fulfillment of requirements
For the Degree of*

DOCTOR OF PHILOSOPHY

of

HOMI BHABHA NATIONAL INSTITUTE



June, 2012

Homi Bhabha National Institute

Recommendations of the Viva Voce Board

As members of the Viva Voce Board, we certify that we have read the dissertation prepared by M. A. Manekar entitled **Magneto-structural Transition and Magnetic Field Induced Effects in Fe-Rh Based Pseudobinary Alloys** and recommend that it may be accepted as fulfilling the dissertation requirement for the Degree of Doctor of Philosophy.



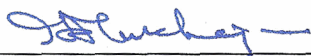
Date: 4.4.2013

Chairman: Dr. P. K. Gupta



Date: 4.4.2013

Guide: Dr. S. B. Roy



Date: 4/4/2013

Member 1: Dr. R. Mukhopadhyay



Date: 4/4/13

Member 2: Dr. G. S. Lodha




Date: 4/4/2013

External Examiner: Prof. E. V. Sampathkumaran

Final approval and acceptance of this dissertation is contingent upon the candidates submission of the final copies of the dissertation to HBNI.

I hereby certify that I have read this dissertation prepared under my direction and recommend that it may be accepted as fulfilling the dissertation requirement.

Date: 4.4.2013

Guide: 
Dr. S. B. Roy

Place: RRAT, Indore

STATEMENT BY AUTHOR

This dissertation has been submitted in partial fulfillment of requirements for an advanced degree at Homi Bhabha National Institute (HBNI) and is deposited in the Library to be made available to borrowers under rules of the HBNI.

Brief quotations from this dissertation are allowable without special permission, provided that accurate acknowledgement of source is made. Requests for permission for extended quotation from or reproduction of this manuscript in whole or in part may be granted by the Competent Authority of HBNI when in his or her judgment the proposed use of the material is in the interests of scholarship. In all other instances, however, permission must be obtained from the author.

M. A. Manekar
M. A. Manekar

DECLARATION

I, hereby declare that the investigation presented in the thesis has been carried out by me. The work is original and has not been submitted earlier as a whole or in part for a degree / diploma at this or any other Institution / University.


M. A. Manekar

DEDICATIONS

पूर्वजांच्या पूर्णत्वासाठी समर्पित ।

ACKNOWLEDGEMENTS

Writing the acknowledgements section of the thesis is probably more difficult than the actual thesis. Mixed thoughts get crowded and the overall emotion is more of a relief than of any achievement. The difficulty in writing this section is due to the fact that anybody who gets hold of this thesis is *definitely* going to read the acknowledgements. The compulsion on the author is to appear socially *nice* in such cases, which further adds to the difficulty. After spending a lot of time on framing an appropriate acknowledgement section, I have finally decided to express my authentic feelings instead of using the formal language which we all come across during such occasions.

First, I would like to thank my guide Dr. S. B. Roy whose role in my life has been of particular importance, as it has brought out a particular dormant aspect of my personality. His presence was necessary to teach me the value of *self-expression*: this thesis being only a small part of the overall learning process. The realization I had while interacting with him was about how to be assertive without being aggressive, which is a useful tool for dealing with denials. Hopefully, I could pursue the problem in this thesis with a similar conviction.

The other people surrounding me have made me aware of certain important sociological phenomena like *independence*, *dependence*, *interdependence* and *codependency*. My sincere acknowledgments to all of them for offering a different perspective of life and taking me one step closer. Thank you all.

While it is customary to mention the names of all the people who were of great help, I am sure that none of them would like to be acknowledged in a formal manner. There were many of them who went out of their way to trace some difficult journal, or to just listen patiently what I wanted to say or were just *there* when needed. Their belief that something good will come out of their help towards me, however

insignificant that may appear to someone else or even themselves, has really motivated me. They all know who they are and may actually be offended if I explicitly mention their names.

My present colleagues, Smt. Parul Arora, Shri Jagdish Chandra, Dr. L. S. Sharath Chandra, Shri Ashim Chakraborty, Dr. M. K. Chattopadhyay, Shri A. Chouhan, Dr. Ashish Khandelwal, Shri Md. Matin, Shri R. K. Meena, Shri S. Nath, Dr. V. K. Sharma, Shri Nageshwar Singh, Shri Shyam Sundar, and Dr. K. J. S. Sokhey have created a healthy competitive environment in our lab which has acted as a catalyst for a person like me to be able to bring this thesis to its present status. Their involvement in the lab is a great stimulant to everyone.

My sincere thanks to all the members of the committee, which monitored my work over these years. The chairman, Dr. P. K. Gupta and other members Dr. R. Mukhopadhyay and Dr. G. S. Lodha have spared some portion of their valuable time only for my betterment.

Finally, I thank all the collaborators who work in other laboratories, but were a part of the experiments. Dr. C. Mukherjee, Dr. Tapas Ganguli and Smt. Pragya Tiwari are more than just professional collaborators and are always willing to solve problems out of their own interest. The cryogenics section (now known as Cryo-engineering and Cryo-module Development Section) also needs a separate mention as this work would not have been possible without the liquid Helium and Nitrogen that they produce.

There is a special thanks for the entire \LaTeX community for teaching the world the art of beautiful typesetting. The community is a living example of how wonderful creativity can be achieved by sharing the knowledge which should be *free* as in freedom.

Contents

	Page
Contents	i
Synopsis	iv
List of Publications	xvii
List of Figures	xix
List of Tables	xxiv
1 Introduction	1
1.1 Phenomenology of first order phase transitions	1
1.1.1 Ehrenfest scheme of classification	1
1.1.2 Landau theory of phase transitions	5
1.2 Hysteresis across a disorder influenced first order transition	11
1.3 The Fe-Rh alloy system	14
2 Experimental methods	18
2.1 Sample preparation and characterization	18
2.1.1 Arc-melting	18
2.1.2 X-ray diffraction	20
2.1.3 Energy dispersive spectroscopy	21
2.2 Measurement of physical properties	23

2.2.1	SQUID magnetometer	23
2.2.2	Vibrating Sample Magnetometer	25
2.2.3	Linear strain	26
2.2.4	ac susceptibility	27
2.2.5	Magnetic force microscopy	28
3	Local imaging of phase coexistence and metastability in $\text{Fe}_{48}\text{Rh}_{52}$ alloy	33
3.1	Introduction	33
3.2	Results and discussion	35
3.2.1	Imaging of phase coexistence	35
3.2.2	Time evolution of the magneto-structural transition	37
3.3	Summary	43
4	Nucleation and growth dynamics across first order phase transition in $\text{Fe}_{0.975}\text{Ni}_{0.025}\text{Rh}$	45
4.1	Introduction	45
4.2	Phase coexistence and metastability	47
4.3	Avrami model of nucleation and growth	51
4.3.1	Isothermal case	52
4.3.2	Temperature driven transition	54
4.4	Identification of phase fraction	56
4.5	Summary	62
5	Modeling of minor hysteresis loops in $\text{Fe}_{0.955}\text{Ni}_{0.045}\text{Rh}$	64
5.1	Introduction	64
5.2	Hysteresis and phase coexistence	65
5.3	General features of minor hysteresis loops	68
5.4	The Preisach model of hysteresis	70

5.5	Modeling of minor hysteresis loops	72
5.6	Deviations from the Preisach model	78
5.7	Summary	80
6	Thermomagnetic history effects in the multi-functional properties of Fe-Rh based alloys	82
6.1	Introduction	82
6.2	Thermomagnetic history effects in magnetization measurements . . .	83
6.3	Influence of history effects on the functional properties	96
6.3.1	Magnetocaloric effect in $\text{Fe}_{48}\text{Rh}_{52}$	96
6.3.2	Large refrigerant capacity in $\text{Fe}_{0.975}\text{Ni}_{0.025}\text{Rh}$	101
6.3.3	Thermomagnetic history effects in giant magnetostriction of $\text{Fe}_{0.955}\text{Ni}_{0.045}\text{Rh}$	109
6.4	Summary	113
7	Glassy dynamics in magnetization across the first order phase transition in $\text{Fe}_{0.955}\text{Ni}_{0.045}\text{Rh}$	115
7.1	Introduction	115
7.2	Thermomagnetic irreversibility in magnetization	117
7.3	Time dependence of magnetization in $\text{Fe}_{0.955}\text{Ni}_{0.045}\text{Rh}$	119
7.4	Metastabilities of two kinds in $\text{Fe}_{0.955}\text{Ni}_{0.045}\text{Rh}$	123
7.5	Competition between growth and arrest in $\text{Fe}_{0.955}\text{Ni}_{0.045}\text{Rh}$	124
7.6	Summary	127
8	Summary and future outlook	129
8.1	Summary	129
8.2	Future outlook	131
	Bibliography	133

Synopsis

The work presented in this thesis is based on the study of physical properties of Fe-Rh and related pseudobinary alloys, which show interesting functionalities governed by a temperature and magnetic field induced first order magneto-structural phase transition. The nearly equiatomic Fe-Rh alloy is known to undergo a first order phase transition during heating from an antiferromagnetic to ferromagnetic state slightly above room temperature and a second order transition from the ferromagnetic to paramagnetic state at about 675 K.¹ The alloy system initially generated interest because magnetization measurements showed an anomalously large magnetic moment in the ferromagnetic phase.¹ The magnetization measurements indicated that the Rh atom must be carrying a magnetic moment in the ferromagnetic phase,¹ which was later verified by neutron scattering experiments² and ab-initio calculations.^{3,4}

The Fe-Rh alloy has a CsCl type crystal structure in the low-temperature antiferromagnetic phase. The same structure is retained in the high-temperature ferromagnetic phase with a 1% discontinuous increase of volume.⁵ The discontinuous volume change can also be induced by the application of magnetic field.⁵ It was reported that the ferromagnetic phase had an excess entropy, which was attributed to the increase in magnetic entropy over the lattice entropy.⁶ The magnetic and electrical transport properties of the nearly equiatomic alloys showed that the antiferromagnetic to ferromagnetic transition temperature T_N and the transition field H_M are extremely sensitive to the Rh concentration.⁷ Addition of small amount of Ni and Pd

shifts the antiferromagnetic to ferromagnetic transition to lower temperatures and magnetic fields.⁸ The magnetic transition which is coupled to a structural change prompted pump-probe experiments using femtosecond laser pulses to determine if the lattice distortion drives the magnetic transition or vice-versa.^{9,10} It was shown in these measurements that the instability in the magnetic lattice drives the structural transition.

While most of the attention was focused on the microscopic origin of the temperature and magnetic field induced antiferromagnetic to ferromagnetic transition and the exact nature of the magnetic structure in both the phases, the technological importance of the alloy was also explored. A technologically important functionality like the giant magnetocaloric effect was reported near room temperature.^{11,12} A large adiabatic temperature change of more than 12 K for a magnetic field excursion of nearly 2 T was observed.¹¹ The other functionalities that were observed near room temperature were the giant elastocaloric effect,¹³ giant magnetostriction,¹⁴ and giant magnetoresistance.¹⁵ Artificial structures made from FeRh/FePt have been proposed for thermally assisted magnetic recording media.¹⁶ We now believe that such wide range of functionalities of this alloy system arises due to the underlying first order magneto-structural phase transition close to room temperature.

It was reported earlier that though the Fe-Rh alloy shows a wide range of important functional properties, some functionalities like the giant magnetocaloric effect vanish after the first field cycle.^{12,17,18} In this work we solve this long-standing problem and show that the possible role of phase coexistence (and associated metastability) across the first order magneto-structural transition in tuning the functional properties of this material has largely gone unnoticed. Such phase coexistence and associated metastability across the first order magneto-structural transition in Fe-Rh alloys give rise to interesting thermomagnetic history effects. We also argue that such thermomagnetic history effects that arise across a disorder influenced first order transition

are actually generic to any other first order transition induced by both temperature and magnetic field and are not limited to only the Fe-Rh system. We clearly show that the vanishing of the giant magnetocaloric effect in Fe-Rh was a misinterpretation of the thermomagnetic history effects which are expected to occur across any first order transition driven by two variables like temperature and magnetic field. Our work presented in the thesis highlights that, apart from having a large value of the functional property (e.g. magnetocaloric effect or magnetostriction), it is necessary to understand the nucleation and growth mechanism across a first order phase transition, if such materials are to be used for reproducible technological applications under multiple temperature or magnetic field cycles. With this brief introduction to the statement of the problem, we now summarize the layout of the proposed thesis.

Chapter 1 of the thesis deals with a brief review on the phenomenology of first order phase transitions,^{19,20} as most of our work presented here is based on the understanding of first order phase transitions. The Ehrenfest scheme of classification of phase transitions and some features of the Landau theory of phase transitions are discussed. The origin of hysteresis across a first order transition is discussed within the framework of the Landau theory and the limits of metastability (supercooling and superheating) are understood.²⁰ The influence of disorder on a first order phase transition and in particular on the nature of the hysteresis loop across a first order phase transition are also discussed qualitatively.²¹ A review of existing literature on the Fe-Rh alloy system is carried out. The chapter then concludes by mentioning the plan of the rest of the thesis and highlighting the motivation behind this work.

Chapter 2 discusses the experimental methods used for obtaining the results presented in this work. The samples were prepared using argon arc melting furnace, and were then characterized using x-ray diffraction, and a scanning electron microscope equipped with energy dispersive spectroscopy. The ac susceptibility as a function of temperature in the range from 78 K to 350 K was measured with a homemade

apparatus using liquid nitrogen as cryogen. The dc magnetization as a function of applied magnetic field and temperature was measured using a commercial SQUID magnetometer and a vibrating sample magnetometer. Linear strain as a function of temperature and magnetic field was measured in two homemade set-ups which were developed earlier in our laboratory.²² Phase coexistence across the magneto-structural transition in the parent Fe-Rh alloy was imaged on a sub-micrometre length scale using magnetic force microscopy. The working principles of each of these instruments are discussed in this chapter.

Chapter 3 focuses on our work on the local imaging (a feature size of a few tens of nano metres) of the first order magneto-structural transition in the parent Fe₄₈Rh₅₂ alloy using magnetic force microscopy. Magnetic force microscopy offers a unique tool for imaging the topography and magnetic information simultaneously as the measurements are performed over the same scan area in two different passes (or scans).²³ The measurements were performed at a single temperature (~ 298 K) on the same sample which was exposed to different temperature histories. Bulk magnetization measurements as a function of temperature on a separate piece of the same sample showed the onset of the antiferromagnetic to ferromagnetic transition slightly below 300 K. The first imaging measurement was performed on the sample which was obtained from the annealing furnace after slow cooling from 1100 °C. With this temperature history, the sample has a coexistence of the ferromagnetic and antiferromagnetic phases as seen from the hysteresis in temperature dependent magnetization measurements (Manekar et al., Europhys. Lett. **80**, 17004 (2007)). The magnetic force microscope directly imaged this phase coexistence on the submicrometre scale. The topographic signal and the magnetic information could be clearly separated out during the measurement. This lack of correlation between the surface and the magnetic clusters is expected as the sample was mechanically polished before mounting it on the measurement platform. The sample was then dipped directly in liquid nitrogen

and brought back to the temperature of measurement. With this temperature history, the sample is mostly in the antiferromagnetic state and very close to the onset of the antiferromagnetic to ferromagnetic transition (Manekar et al., Europhys. Lett. **80**, 17004 (2007)). The nucleation and growth of the ferromagnetic clusters within the largely antiferromagnetic matrix was then imaged as a function of time by scanning periodically over the same scan area of the sample. The formation of newer nuclei of the ferromagnetic phase and their growth at the existing nucleation centres could be imaged directly. The changes in the topography (signifying the lattice change across the transition) were accompanied with the changes in the magnetic structure at the same location. The explicit imaging of the correlation between the elastic and electronic degrees of freedom in our sample enabled us to show, that a model explaining multiscale phase coexistence in manganites which show colossal magnetoresistance,²⁴ can be applied to other systems as well irrespective of the nature of underlying microscopic interaction (Manekar et al., Europhys. Lett. **80**, 17004 (2007)). The phase coexistence and metastability are shown to be generic features related to any first order phase transition.

Chapter 4 builds on the results presented in **Chapter 3** and attempts to generalize the concepts of nucleation and growth mechanism during a crystallization process²⁵ to the first order magnetic transitions which are driven by temperature and magnetic field. The sample used for this study was $(\text{Fe}_{0.975}\text{Ni}_{0.025})_{50}\text{Rh}_{50}$. The presence of phase coexistence and metastable states across the first order antiferromagnetic to ferromagnetic transition in this sample was inferred from bulk measurements viz. temperature dependent ac susceptibility and bulk magnetization as a function of temperature and magnetic field. The minor hysteresis loops technique²⁶ is used to track and study the phase coexistence of the two competing phases across the phase transition. Magnetic relaxation measurements show the metastable nature of the phase being transformed. The magnetic relaxation measurements across the tem-

perature and field driven transitions show a distinct power law which arises from the dipolar interaction within the ferromagnetic clusters across the antiferromagnetic to ferromagnetic and the back transformation. The relaxation measurements are used to identify the crossover from nucleation to growth (Manekar and Roy, J. Phys.: Condens. Matter **20**, 325208 (2008)). In this chapter a brief discussion is carried out on the Avrami model of nucleation and growth process during crystallization of solid from melt.²⁵ The evolution of the fraction of the crystalline phase from melt as a function of time is briefly reviewed, which is popularly known as the Kolmogorov-Johnson-Mehl-Avrami (KJMA) relation. A heuristic argument is also given for transforming the KJMA relation as a function of time to a general relation which is a function of temperature. While extending the KJMA relation to temperature and magnetic field driven transitions, the central problem is the identification of the phase fraction of the transformed phase from bulk measurements. Bulk magnetization or susceptibility cannot be taken as a measure of phase fraction because the measured bulk magnetization is a vector sum of all the local moments pointing in random directions (Manekar et al., Europhys. Lett. **80**, 17004 (2007)). We have proposed to quantify the phase fraction by relating it to the area of the minor hysteresis loops. This idea is based on the conjecture that different locations of the sample undergo transition at different values of the external driving parameter and each of these locations has its own hysteresis. This is essentially the *landscape* picture of transition temperatures as proposed for manganites.²⁴ The areas of the minor hysteresis loops as a function of temperature and magnetic field are shown to follow the KJMA relation by replacing *time* with *temperature* and *magnetic field* for the respective transitions. The KJMA model is thus extended for temperature and magnetic field. The nucleation and growth dynamics across a first order magnetic transition are shown to be analogous to those of crystallization during melt (Manekar and Roy, J. Phys.: Condens. Matter **20**, 325208 (2008)).

Chapter 5 further explores into the outcome of the conjectures proposed in **Chapter 4** about the identification of phase fraction from the nature of the hysteresis loop across a first order transition. The sample under investigation is another Ni doped Fe-Rh alloy with the composition of $\text{Fe}_{0.955}\text{Ni}_{0.045}\text{Rh}$, and the physical property (or functionality) that is measured is the linear strain across the temperature driven first order transition. A large strain of about 0.4% is observed across the magnetostructural transition (Manekar et al., J. Phys.: Condens. Matter **24**, 216004 (2012)). The minor hysteresis loops are found to retain the memory of the last reversal of the temperature change, over the entire temperature range and irrespective of the temperature history followed to reach the point of initiation. This memory is termed as the end point memory. The smaller temperature excursion is wiped out by a larger excursion if the larger excursion contains one of the extrema of the smaller excursion. To explain these properties of the minor hysteresis loops, we have proposed that the Preisach model of hysteresis (which was originally proposed for hysteresis in ferromagnets) is a natural way to relate the picture of *landscape* of transition temperatures, which arises in a disorder influenced first order phase transition (Manekar et al., J. Phys.: Condens. Matter **24**, 216004 (2012)). The basic assumption of the Preisach model is that the complete hysteresis curve (also termed as the envelope curve) can be expressed as a summation of elementary hysteresis operators (or bistable switches) which switch between 0 to +1 at a value ' α ' during the temperature increasing cycle and back from +1 to 0 at a value ' β ' during the temperature decreasing cycle.²⁷ This is the same assumption which we had proposed in **chapter 4** that individual pockets of the samples have their own independent hysteresis loops across the transition. The Preisach model for our case is able to explain the end point memory and wiping out property of the minor hysteresis loops. However, the model does not apply entirely for larger temperature excursions and cannot account for the lack of congruency between the envelope curve and the minor hysteresis loops. This

discrepancy is most probably due to a crossover from nucleation to growth across the transition (Manekar et al., J. Phys.: Condens. Matter **24**, 216004 (2012)). Our observations pose certain questions about the *local* nature of end point memory and congruency which need further experiments at various length scales on samples prepared with carefully controlled disorder. We believe that these future experiments could provide further information which is useful for tuning the functional properties of smart materials whose applications are based on first order phase transitions. The modeling of minor hysteresis loops allows us to predict the outcome of a temperature cycle inside the hysteretic region on the basis of only a few measurements initiated on the envelope heating curve. This observation could be quite important for applications under multiple cycles of the external driving parameter.

Chapter 6 reports the history effects in functional properties across the first order transition when the transition is driven by two external variables like temperature and magnetic field. In the earlier chapters the discussion is mainly on the characteristic features of a disorder influenced first order phase transition for only those cases when the transition occurs as a function of one variable alone, i.e. time, temperature or magnetic field. In this chapter we show that interesting thermomagnetic history effects arise due to the broadening of the transition in the presence of disorder. Specifically we show that the virgin magnetization curve lies outside the envelope curve, and is lost for that particular cycle, when the isothermal field cycle is initiated within certain temperature range of the field-temperature phase space. These history effects are generic to any first order phase transition driven by both magnetic field and temperature and are not limited to only Fe-Rh (Manekar and Roy, Eur. Phys. J. B **64**, 19 (2008)). We also show that these history effects in the Fe-Rh alloy were misinterpreted to conclude that the giant magnetocaloric effect in this system vanishes after the first field cycle. We estimate the magnetocaloric effect in the parent Fe-Rh alloy for various histories of temperature and magnetic field and show

that a reproducible entropy change can be achieved if the starting point of the field-temperature cycle is chosen properly. Thus we have solved a long standing problem in this area (Manekar and Roy, J. Phys. D: Appl. Phys. **41**, 192004 (2008)). The understanding of these thermomagnetic history effects is used to estimate the magnetocaloric effect in yet another Ni doped alloy, namely $\text{Fe}_{0.975}\text{Ni}_{0.025}\text{Rh}$. We report a very large effective refrigerant capacity of nearly 492.8 J kg^{-1} for a field excursion of 5 T at room temperature with the hot end at 307 K. This large effective refrigerant capacity is probably the highest achieved yet for any material at room temperature. The refrigerant capacity could be increased over the parent alloy by the addition of small amount of disorder in form on Ni, because the disorder tends to broaden the first order phase transition (Manekar and Roy, J. Phys. D: Appl. Phys. **44**, 242001 (2011)). The disorder thus plays an important role in tuning the functionality of the materials undergoing first order phase transitions. Thermomagnetic history effects are also reported in the giant magnetostriction across the first order transition in $\text{Fe}_{0.955}\text{Ni}_{0.045}\text{Rh}$, which can be explained using the same understanding developed for explaining the history effects in magnetization (Manekar et al., J. Phys.: Condens. Matter **24**, 216004 (2012)). Our results on the thermomagnetic history effects in functional properties reported in this chapter further highlight the necessity to understand the influence of disorder, which was discussed in the earlier chapters, so as to achieve a repeatable performance of materials whose functionalities are based on first order phase transitions.

Chapter 7 discusses about the glassy dynamics reflected in magnetization measurements across the ferromagnetic to antiferromagnetic transition during cooling in $\text{Fe}_{0.955}\text{Ni}_{0.045}\text{Rh}$. In the earlier chapters, the discussion is about how disorder influences the functional properties of materials undergoing a first order phase transition. By increasing the disorder even further by adding more amount of Ni, we see the presence of glassy dynamics in magnetization measurements. The arrest of the kinet-

ics of the ferromagnetic to antiferromagnetic transition during cooling was inferred by observing thermomagnetic history effects in the temperature dependent magnetization. Magnetic relaxation measurements showed a combination of two different kinds of metastabilities, one arising from the first order phase transition and the second one is the stretched exponential behaviour which is typical of glassy dynamics.²⁸ The fractions of the arrested and non-arrested metastable phases were inferred from the weights of the individual relaxation processes. It was observed that a dramatic increase in the fraction of the arrested ferromagnetic phase almost coincides with the crossover from the nucleation to growth of the antiferromagnetic phase. We conjecture that this coincidence is an outcome of the disorder influenced nature of the first order ferromagnetic to antiferromagnetic phase transition. The heterogeneous nucleation in such disorder influenced first order phase transition is expected to create interfaces between the coexisting phases. The onset of kinetic arrest or glassy dynamics in this alloy is possibly linked to the decrease in mobility of these interfaces, creating a situation where the growth of the product phase influences the kinetic arrest of the transition itself. The presence of disorder thus not only tunes the functional properties as we have seen before, but also can lead to an entirely new interesting phenomenon of arresting the kinetics of the transition (Manekar et al., J. Phys.: Condens. Matter **23**, 086001 (2011)).

Chapter 8 summarizes the main findings of the work presented in the thesis and tries to project some of the ideas for further experiments. The central theme of the thesis is related to the influence of disorder on first order phase transitions and how the functional properties can be tuned by understanding the history effects arising from this influence. This understanding evolved through the local imaging of the first order transition process and bulk measurements related to the observation of phase coexistence and metastability to study the nucleation and growth dynamics. These concepts were implemented to solve a long-standing problem of the vanishing

magnetocaloric effect in Fe-Rh alloy system and discovering a very large effective refrigeration capacity in one of the related alloys. New interesting phenomenon like the arrest of the kinetics of a first order phase transition were also discovered and related to the influence of disorder. The future work would be to characterize the exact nature of this disorder and attempt to make samples with controlled disorder, so as to further explore the nucleation and growth processes across first order phase transitions. Another direction could be to understand the nature of microscopic interactions between the constituent elements of solids undergoing first order magneto-structural transitions so that newer materials can be designed with desired functionalities.

References

- [1] J. S. Kouvel and C. C. Hartelius, J. Appl. Phys. **33** suppl., 1343 (1962). [iv](#)
- [2] G. Shirane, R. Nathans, and C. W. Chen, Phys. Rev. **134**, A1547 (1964). [iv](#)
- [3] V. L. Moruzzi and P. M. Marcus, Phys. Rev. B. **46**, 2864 (1992). [iv](#)
- [4] M. E. Gruner, E. Hoffmann, and P. Entel, Phys. Rev. B. **67**, 064415 (2003). [iv](#)
- [5] A. I. Zakharov, A. M. Kadomtseva, R. Z. Levitin, and E. G. Ponyatovskii, Sov. Phys. JETP **19**, 1348 (1964). [iv](#)
- [6] J. S. Kouvel, J. Appl. Phys. **37**, 1257 (1966). [iv](#)
- [7] C. J. Schinkel, R. Hartog, and F. Hochstenbach, J. Phys. F: Metal Phys. **4**, 1412 (1974). [iv](#)
- [8] N. V. Baranov and E. A. Barabanova, J. Alloys Compd. **219**, 139 (1995). [v](#)

- [9] M. Lederman, G. A. Gibson, and S. Schultz, J. Appl. Phys. **73**, 6961 (1993). [v](#)
- [10] G. Ju, Phys. Rev. Lett. **93**, 197403 (2004). [v](#)
- [11] S. A. Nikitin, G. Myalikgulyev, A. M. Tishin, M. P. Annaorazov, K. A. Asatryan, and A. L. Tyurin, Phys. Lett. A. **148**, 363 (1990). [v](#)
- [12] M. P. Annaorazov, S. A. Nikitin, A. L. Tyurin, K. A. Asatryan, and A. K. Dovletov, J. Appl. Phys. **79**, 1689 (1996). [v](#)
- [13] S. A. Nikitin, G. Myalikgulyev, M. P. Annaorazov, A. L. Tyurin, R. W. Myndyev, and S. A. Akopyan, Phys. Lett. A. **171**, 234 (1992). [v](#)
- [14] M. R. Ibarra and P. A. Algarabel, Phys. Rev. B **50**, 4196 (1994). [v](#)
- [15] P. A. Algarabel, M. R. Ibarra, C. Marquina, A. D. Moral, J. Galibert, M. Iqbal, and S. Askenazy, Appl. Phys. Lett. **66**, 3061 (1995). [v](#)
- [16] J. Thiele, S. Maat, and E. E. Fullerton, Appl. Phys. Lett. **82**, 2859 (2003). [v](#)
- [17] V. K. Pecharsky and K. A. Gschneidner, Jr., J. Magn. Magn. Mater. **200**, 44 (1999). [v](#)
- [18] V. K. Pecharsky and K. A. Gschneidner, Jr., Phys. Rev. Lett. **78**, 4494 (1997). [v](#)
- [19] R. M. White and T. H. Geballe, *Long range order in solids* (Academic Press, New York, 1979). [vi](#)
- [20] P. M. Chaikin and T. C. Lubensky, *Principles of condensed matter physics*. (Cambridge University Press, Cambridge, 1995), [vi](#)
- [21] M. K. Chattopadhyay, S. B. Roy, A. K. Nigam, K. J. S. Sokhey, and P. Chaddah, Phys. Rev. B. **68**, 174404 (2003). [vi](#)
- [22] V. K. Sharma, [Ph.D. thesis](#), Homi Bhaha National Institute, Raja Rammana Centre for Advanced Technology, Indore (2012). [vii](#)
- [23] Yimei Zhu ed., *Modern techniques for characterizing magnetic materials*. (Kluwer Academic Publishers, Boston, 2005), see chapter 11. [vii](#)
- [24] K. H. Ahn, T. Lookman, and A. R. Bishop, Nature **428**, 401 (2004). [viii](#), [ix](#)
- [25] M. Avrami, J. Chem. Phys **7**, 1103 (1939). [viii](#), [ix](#)

- [26] M. Manekar, S. B. Roy, and P. Chaddah, J. Phys.: Condens. Matter **12**, L409 (2000). **viii**
- [27] I. Mayergoyz, *Mathematical models of hysteresis and their applications* (Elsevier Science, New York, 2003), 2nd ed. **x**
- [28] P. G. Debenedetti and F. H. Stillinger, Nature **410**, 259 (2001). **xiii**

List of Publications

In Refereed Journals:

- 1) Imaging of time evolution of the first-order magneto-structural transition in Fe-Rh alloy using magnetic force microscopy
M. Manekar, C. Mukherjee and S. B. Roy
Europhys. Lett. **80**, 17004 (2007).
- 2) Thermomagnetic history effects across the first order magneto-structural transition in the giant magnetocaloric Fe-Rh alloy
M. Manekar and S. B. Roy
Eur. Phys. J. B **64**, 19 (2008).
- 3) Reproducible room temperature giant magnetocaloric effect in Fe-Rh
M. Manekar and S. B. Roy
J. Phys. D: Appl. Phys. **41**, 192004 (2008).
- 4) Nucleation and growth dynamics across the antiferromagnetic to ferromagnetic transition in $(\text{Fe}_{0.975}\text{Ni}_{0.025})_{50}\text{Rh}_{50}$: analogy with crystallization
M. Manekar and S. B. Roy
J. Phys.: Condens. Matter **20**, 325208 (2008).
- 5) Glassy dynamics in magnetization across the first order ferromagnetic to anti-ferromagnetic transition in $\text{Fe}_{0.955}\text{Ni}_{0.045}\text{Rh}$
M. Manekar, M. K. Chattopadhyay and S. B. Roy
J. Phys.: Condens. Matter **23**, 086001 (2011).

- 6) Very large refrigerant capacity at room temperature with reproducible magnetocaloric effect in $\text{Fe}_{0.975}\text{Ni}_{0.025}\text{Rh}$
M. Manekar and S. B. Roy
J. Phys. D: Appl. Phys. **44**, 242001 (2011).
- 7) Thermo-magnetic history effects in the giant magnetostriction across the first order transition and minor hysteresis loops modeling in $\text{Fe}_{0.955}\text{Ni}_{0.045}\text{Rh}$ alloy
M. Manekar V. K. Sharma and S. B. Roy
J. Phys.: Condens. Matter **24**, 216004 (2012).

In Conference Proceedings:

- 1) Phase coexistence and its implications on the functional properties of the room-temperature giant magnetocaloric alloy Fe-Rh
M. Manekar
Proceedings of the 53^d DAE Solid state physics symposium, (BARC, Mumbai)
p. 25 (2008) (**Invited talk**).

List of Figures

1.1	Behaviour of the Gibbs free energy at a first order transition.	2
1.2	Behaviour of Gibbs free energy at a first order transition in presence of disorder.	3
1.3	Behaviour of entropy at a first order transition in presence of disorder.	4
1.4	Order parameter as a function of temperature for first order and second order phase transition.	7
1.5	Free energy as a function of order parameter at different temperatures when odd order terms of the order parameter are allowed.	8
1.6	Free energy as a function of order parameter at different temperatures when even order terms of the order parameter are allowed.	10
1.7	Influence of disorder on the hysteresis across a first order transition. .	12
1.8	The lattice and magnetic structures of Fe-Rh.	14
2.1	Photograph of the arc-melting furnace used for sample preparation. .	19
2.2	Schematic of x-ray diffraction from a set of atomic planes.	20
2.3	X-ray diffraction pattern for the parent Fe-Rh alloy used in this work.	21
2.4	Schematic of excitation of a characteristic X-ray photon by a high energy electron or photon.	22
2.5	Interaction of the electron probe and specimen atoms below a specimen surface.	22
2.6	Microstructure and energy dispersive spectrum of the parent Fe-Rh alloy.	23
2.7	Schematic of the SQUID magnetometer detection system.	24
2.8	Schematic of a Vibrating Sample Magnetometer.	25
2.9	Schematic of the strain gauge used in the present study.	26
2.10	Schematic of the home made ac susceptometer.	28
2.11	Schematic of a magnetic force microscopy apparatus.	29
2.12	Shift in the resonant frequency and phase of the oscillating cantilever of a magnetic force microscope.	30
2.13	The force experienced by the tip of a magnetic force microscope as a function of the distance from the sample.	30

2.14	Schematic of a magnetic force microscopy scan to acquire the information of the topography.	31
2.15	Schematic of a magnetic force microscopy scan to acquire the magnetic information.	32
3.1	Magnetization as a function of temperature of the $\text{Fe}_{48}\text{Rh}_{52}$ alloy, both while heating and cooling in a magnetic field $\mu_0 H = 10$ mT.	35
3.2	2D image of a magnetic force microscopy scan along with the raw data of the topography and magnetic information of the $\text{Fe}_{48}\text{Rh}_{52}$ sample before subjecting it to any temperature or field cycles.	36
3.3	Time evolution of topography and the corresponding magnetic information after the $\text{Fe}_{48}\text{Rh}_{52}$ sample was cooled to liquid nitrogen temperature and brought back to room temperature.	39
3.4	Distribution of counts obtained for phase shifts plotted in the images of figure 3.3.	40
4.1	Ac susceptibility as a function of temperature showing hysteresis and phase coexistence across the first order transition in $\text{Fe}_{0.975}\text{Ni}_{0.025}\text{Rh}$	48
4.2	Time dependent magnetization during the temperature driven transition in $\text{Fe}_{0.975}\text{Ni}_{0.025}\text{Rh}$ at representative temperatures during the heating and cooling cycles.	49
4.3	Temperature dependence of the exponent γ in equation 4.1 during the temperature driven transition in $\text{Fe}_{0.975}\text{Ni}_{0.025}\text{Rh}$	50
4.4	Schematic of the nucleation and growth process in the Avrami model.	52
4.5	Phase fraction as a function of time at constant temperatures during solidification of pure copper from melt.	54
4.6	Phase fraction of the ferromagnetic phase inferred from the ac susceptibility measurements on $\text{Fe}_{0.975}\text{Ni}_{0.025}\text{Rh}$ shown in figure 4.1 and the fit with equation 4.12.	57
4.7	Isothermal magnetization as a function of magnetic field with minor hysteresis loops across the metamagnetic transition in $\text{Fe}_{0.975}\text{Ni}_{0.025}\text{Rh}$	58
4.8	Time dependent magnetization during the field induced transition in $\text{Fe}_{0.975}\text{Ni}_{0.025}\text{Rh}$ at representative fields on the field-increasing cycle and the field-decreasing cycle.	60
4.9	Magnetic-field dependence of the exponent γ in equation 4.1 during the field driven transition in $\text{Fe}_{0.975}\text{Ni}_{0.025}\text{Rh}$	60

4.10	Phase fraction of the ferromagnetic phase inferred from the dc magnetization measurements on $\text{Fe}_{0.975}\text{Ni}_{0.025}\text{Rh}$ shown in figure 4.7 and the fit with equation 4.13.	62
5.1	Linear strain as a function of temperature during the heating and cooling cycles in $\text{Fe}_{0.955}\text{Ni}_{0.045}\text{Rh}$	66
5.2	Minor hysteresis loops initiated on the heating and cooling cycle across the temperature driven first order transition in $\text{Fe}_{0.955}\text{Ni}_{0.045}\text{Rh}$	68
5.3	Minor hysteresis loop during the temperature driven transition in $\text{Fe}_{0.955}\text{Ni}_{0.045}\text{Rh}$, which shows the end point memory and the wiping out property and the comparison with the $B - H$ hysteresis loop in a usual ferromagnet.	69
5.4	The definition of an elementary hysteresis operator according to the Preisach model for explaining the hysteresis in figure 5.1.	71
5.5	A pictorial representation of the Preisach model given in equation 5.1.	72
5.6	One example of the first order reversal curve in the hysteretic region across the first order transition in $\text{Fe}_{0.955}\text{Ni}_{0.045}\text{Rh}$ and the corresponding geometrical construction in the Preisach plane.	73
5.7	Experimental minor hysteresis loops and the equivalent geometrical construction for the temperature cycling across the first order transition in $\text{Fe}_{0.955}\text{Ni}_{0.045}\text{Rh}$ along with the calculated output using equations 5.7 and 5.9.	75
5.8	One more experimental minor hysteresis loops and the equivalent geometrical construction for the temperature cycling across the first order transition in $\text{Fe}_{0.955}\text{Ni}_{0.045}\text{Rh}$ along with the calculated output using equations 5.7 and 5.9.	77
5.9	Schematic of minor hysteresis loops to explain the meaning of ‘congruency’.	78
5.10	Results of calculation using equations 5.7 and 5.9 along with the experimental data of $\text{Fe}_{0.955}\text{Ni}_{0.045}\text{Rh}$ which show the breakdown of Preisach model for larger temperature excursions.	79
6.1	Ac susceptibility of $\text{Fe}_{48}\text{Rh}_{52}$ as a function of temperature in an ac magnetic field of 3.4×10^{-4} T rms.	84
6.2	Magnetization of $\text{Fe}_{48}\text{Rh}_{52}$ as a function of temperature in a magnetic field of 1 T.	86
6.3	Magnetization of $\text{Fe}_{48}\text{Rh}_{52}$ as a function of field at 270 K.	87
6.4	Magnetization of $\text{Fe}_{48}\text{Rh}_{52}$ as a function of field at 290 K.	88

6.5	Magnetization of $\text{Fe}_{48}\text{Rh}_{52}$ as a function of field at 305 K.	89
6.6	Magnetic relaxation measurements on $\text{Fe}_{48}\text{Rh}_{52}$ at 305 K on the virgin curve and the envelope curve.	90
6.7	Difference of magnetization of $\text{Fe}_{48}\text{Rh}_{52}$ on the envelope curve and the virgin curve as a function of temperature.	91
6.8	$H-T$ phase diagram of $\text{Fe}_{48}\text{Rh}_{52}$ constructed from magnetization measurements.	92
6.9	Schematic of magnetic refrigeration based on the magnetocaloric effect and a comparison with the conventional vapour compression cycle. . .	97
6.10	Magnetocaloric effect in $\text{Fe}_{48}\text{Rh}_{52}$ as a function of temperature for a field excursion of 5 T following three different protocols.	100
6.11	Magnetization of $\text{Fe}_{0.975}\text{Ni}_{0.025}\text{Rh}$ as a function of temperature in a magnetic field of 10 mT.	102
6.12	Magnetization of $\text{Fe}_{0.975}\text{Ni}_{0.025}\text{Rh}$ as a function of field at 250 K and 270 K.	104
6.13	Derivative of magnetization of $\text{Fe}_{0.975}\text{Ni}_{0.025}\text{Rh}$ with respect to temperature and the plot of $\partial M/\partial T$ at 260 K as a function of field.	105
6.14	The magnetocaloric effect in $\text{Fe}_{0.975}\text{Ni}_{0.025}\text{Rh}$ as a function of temperature for a field excursion of $\mu_0 H = 5T$, estimated from isothermal $M-H$ and constant field $M-T$ curves.	106
6.15	Schematic of the conventional magnetostriction.	110
6.16	Linear strain in $\text{Fe}_{0.955}\text{Ni}_{0.045}\text{Rh}$ as a function of temperature in different values of applied magnetic field.	110
6.17	Magnetostriction in $\text{Fe}_{0.955}\text{Ni}_{0.045}\text{Rh}$ at 170 K along with the minor hysteresis loops generated on the field-increasing and decreasing cycle.	111
6.18	Magnetostriction in $\text{Fe}_{0.955}\text{Ni}_{0.045}\text{Rh}$ at 200 K and 240 K.	112
6.19	Field-temperature phase diagram of $\text{Fe}_{0.955}\text{Ni}_{0.045}\text{Rh}$ constructed from linear strain measurements.	113
7.1	Magnetization of $\text{Fe}_{0.955}\text{Ni}_{0.045}\text{Rh}$ as a function of temperature in an applied field of 10 mT under three different protocols.	118
7.2	Magnetization of $\text{Fe}_{0.955}\text{Ni}_{0.045}\text{Rh}$ as a function of temperature in an applied field of 5 T under three different protocols.	119
7.3	Normalized magnetization of $\text{Fe}_{0.955}\text{Ni}_{0.045}\text{Rh}$ as a function of time, along with the fit to equation 7.1 at 130 K and 110 K on the field-cooled-cooling cycle in an applied field of 5 T.	120

7.4	Normalized magnetization of $\text{Fe}_{0.955}\text{Ni}_{0.045}\text{Rh}$ as a function of time, along with the fit to equation 7.2 at 80 K and 70 K on the field-cooled-cooling cycle in an applied field of 5 T.	121
7.5	Normalized magnetization of $\text{Fe}_{0.955}\text{Ni}_{0.045}\text{Rh}$ as a function of time at 50 K and 30 K on the field-cooled-cooling cycle in an applied field of 5 T.	122
7.6	The metastable phase fraction in $\text{Fe}_{0.955}\text{Ni}_{0.045}\text{Rh}$ as a function of temperature across the ferromagnetic to antiferromagnetic transition. . .	124
7.7	The temperature dependence of the absolute value of the exponent γ of the power law in equation 7.1.	125
7.8	The temperature dependence of the time constant τ in the stretched exponential term of equation 7.2 along with a fit to the equation 7.3. . .	126

List of Tables

1.1	List of order parameters for various systems undergoing phase transitions.	6
6.1	Refrigerant capacities of Fe-Rh based alloys.	107

Chapter 1

Introduction

The work presented in this thesis is based on the study of physical properties of Fe-Rh and related pseudobinary alloys, which lead to interesting functionalities governed by a temperature and magnetic field induced first order magneto-structural phase transition in these alloys. In the following sections of this chapter, we briefly introduce the necessary theoretical concepts and the existing information on the alloy system prior to the commencement of this work.

1.1 Phenomenology of first order phase transitions

1.1.1 Ehrenfest scheme of classification

According to the Ehrenfest scheme of classification of phase transitions, a transition is said to be of n^{th} order if the n^{th} order derivative of the Gibbs free energy:

$$G = U - TS + PV \tag{1.1}$$

is the first discontinuous derivative.¹ Here U is the internal energy, T is the temperature, S is the entropy, P is the pressure and V is the volume. The differentiation is carried out with respect to the intensive thermodynamic variables like T or P . Thus a first order transition would mean a discontinuity in entropy as a function of

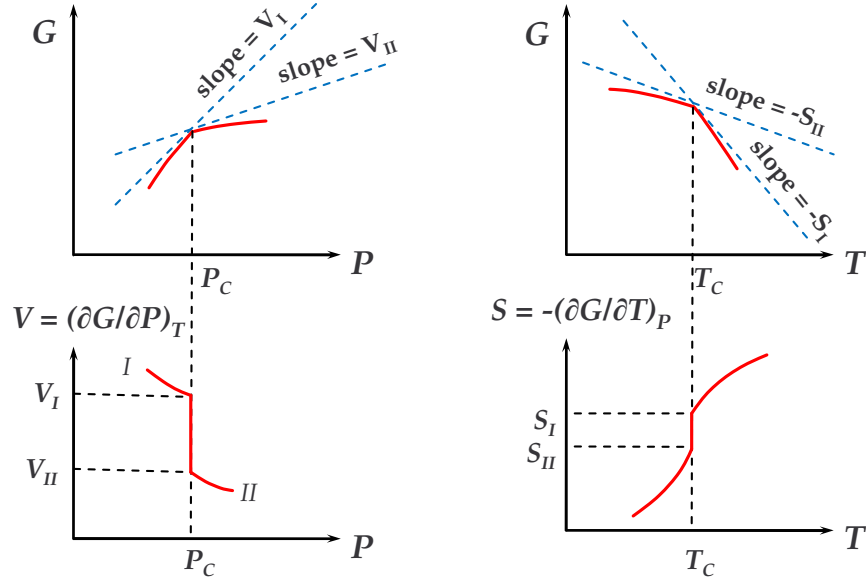


Figure 1.1: Typical behaviour of the Gibbs free energy at a first order transition. V_I and V_{II} are the volumes in the low pressure and high pressure phases respectively. Similarly S_I and S_{II} are the entropies in the high temperature and low temperature phases respectively. The transition temperature (T_c) and transition pressure (P_c) are defined as that temperature and pressure where the Gibbs free energy of both the phases is equal. Recreated from ref. [1].

temperature or a discontinuity in volume as a function of pressure. Equation 1.1 is applicable for PVT systems only but can be generalized to include the effect of other variables like magnetic field (H) or electric field (E).^{1,2} Figure 1.1 shows the Gibbs free energy as a function of temperature and pressure and their respective derivatives at a first order transition point. The slope of the Gibbs free energy at the transition point is discontinuous. When the slope of G is discontinuous at T_c , it is possible to drag the high- T phase below T_c (known as supercooling) and also to carry the low- T phase above T_c (superheating).² This leads to hysteresis across the transition and is quite commonly observed during melting transitions (like ice to water for example).²

The discontinuities shown in figure 1.1 can be experimentally measured by measuring the latent heat (discontinuity in entropy) or discontinuity in volume. However, such sharp discontinuities have been observed only in ultra-pure systems like elemental Dy and are generally difficult to measure in alloy systems.³ The local composition

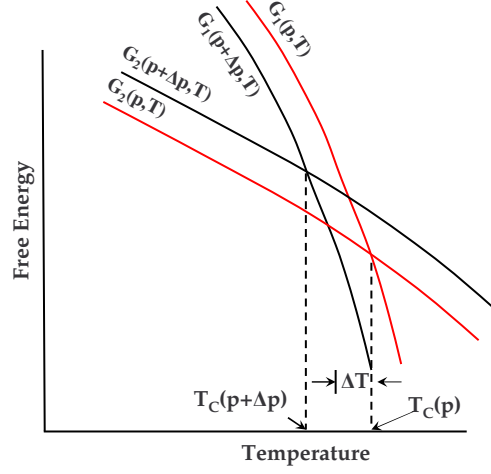


Figure 1.2: Behaviour of Gibbs free energy at a first order transition in presence of disorder. See text for details. Recreated from ref. [4].

in any alloy system or doped compound varies around some average composition due to the disorder that is frozen-in as the solid crystallizes from the melt. The frozen disorder can arise in form of dislocations, vacancies, atomic configuration and grain boundaries. The role of this disorder is to block the growth of correlations, resulting in effective inhomogeneity in the sample and smearing of the discontinuity across the transition.⁴

This smearing of the discontinuity can be understood in terms of the situation shown in figure 1.2. Here G_1 is the free energy of the high-temperature phase (phase 1) and G_2 is the free energy of the low-temperature phase (phase 2). We mostly follow here the arguments given by Imry and Wortis.⁴ The impurity concentration (or the probability of the occupancy of a lattice site by an impurity species) is taken as ‘ p ’. This impurity concentration can vary randomly at different locations of the sample. In each of these localized pockets, the transition is assumed to be a pure system-like sharp transition. If we compare the free energies of two local pockets in the sample where the impurity concentrations are ‘ p ’ and ‘ $(p + \Delta p)$ ’ respectively, we find that the high-temperature phase is more stable relative to the low-temperature phase when the impurity concentration is higher (see figure 1.2). The transition temperature T_c

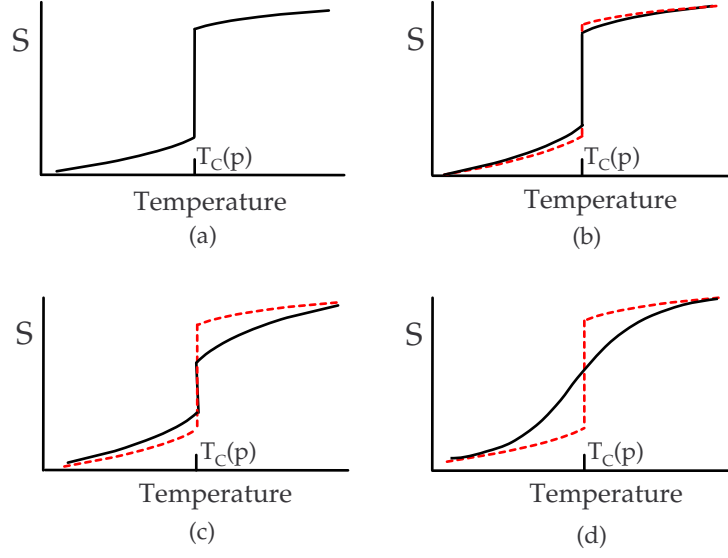


Figure 1.3: Behaviour of entropy at a first order transition in presence of disorder. (a) Pure system-like sharp discontinuity, (b) the magnitude of discontinuity reduces slightly with the addition of small quantity of disorder, (c) substantial reduction in the magnitude of discontinuity due to large amount of disorder and (d) a very large amount of disorder eventually smears off the discontinuity making the transition appear like a second order transition. Recreated from ref. [4].

is therefore lowered by the addition of impurities. Thus we may assume that each coherence volume (volume over which correlation exists, beyond which it is blocked by impurities) undergoes a transition at its own $T_c(p + \Delta p)$. However, the transformation of one pocket in the sample creates an interface between the two phases which requires an additional energy. Thus the actual transformation in a localized volume occurs when the cost of energy during creating the interface is compensated by the lowering of free energy during the transformation. The sample is thus in a mixed phase (phase coexistent state) between the temperatures $(T_c(p) - \Delta T_c)$ and $(T_c(p) + \Delta T_c)$, thereby smearing off the transition over a temperature range of ΔT_c . The sample still shows an ideal discontinuity on a local scale but when the measurement is performed on the entire bulk, the discontinuity appears to get rounded off.

Figure 1.3 shows the typical smearing of the discontinuity as the impurity concentration is progressively increased. In such cases where the disorder has reduced the magnitude of discontinuity or has smeared out the transition, hysteresis in observable

properties (*not necessarily thermodynamically extensive ones*, like resistivity for example) and phase coexistence across the transition remain useful tools to distinguish between a first order and a second order transition.² Hysteresis is not observed across a second order transition as there is no discontinuity in the slope of the Gibbs free energy at the transition point.

The limitation of the Ehrenfest scheme arises in case of certain transitions, like the normal to superfluid transition in ^4He where the heat capacity increases logarithmically near the transition point like the greek letter ‘ λ ’. Such logarithmic behaviour means that all the derivatives of the free energy *diverge* and the Ehrenfest scheme breaks down.² The other limitation, specifically in the case of first order transitions is related to the extent of supercooling and superheating. A discontinuous slope of the Gibbs free energy at the transition point only indicates a possibility of supercooling and superheating, but does not explain their limits. From the behaviour of free energy shown in figures 1.1 and 1.2, it appears that supercooling and/or superheating can proceed indefinitely beyond the transition point.

1.1.2 Landau theory of phase transitions

A description of phase transitions is required that deals with divergences of the physical properties instead of discontinuities of the derivatives of free energy. The same description should also provide a limit of superheating and supercooling in case of first order transitions. This general description is based on the fact that during *most* of the phase transitions, there is an appearance of a nonzero quantity in the ordered state.^{2,5} Such a nonzero quantity in the ordered phase, which distinguishes it from the disordered phase, is called the *order parameter*. By identifying a proper order parameter related to the system, all phase transitions can be explained in terms of order-disorder transitions (here, *disorder* is not related to the *quenched disorder* in form of defects and dislocations discussed above). The phase transitions are now

Table 1.1: List of order parameters for various systems undergoing phase transitions. Reproduced from ref. [6].

System	Order Parameters	Conjugate field
Ferromagnet	Magnetization Density	Uniform magnetic field
Antiferromagnet	Staggered-magnetization density	Staggered magnetic field
Superconductivity	Electron pairing function	Pair source
Phase separation in alloys	Density of components	Chemical Potential
Order-disorder in alloys	Sublattice density of components	Chemical Potential
Displacive transitions	Soft-mode density	Stress field
Ferroelectric transitions	Soft-mode density or Spontaneous Polarization	Uniform electric field
Antiferroelectric transition	Soft-mode density or Staggered Polarization	Staggered electric field
Nematic liquid crystal	Traceless director tensor	Electric field

identified within only two categories, either first order transition or the second order transition depending upon whether the order parameter changes discontinuously or continuously across the transition (see figure 1.4). Table 1.1 lists the order parameters identified for various systems which undergo phase transition.

In the Landau theory of phase transitions, the free energy is expanded in terms of power series of the order parameter. Such an expansion is valid only for small values of order parameter, i.e. only near to the transition point. The free energy G in terms

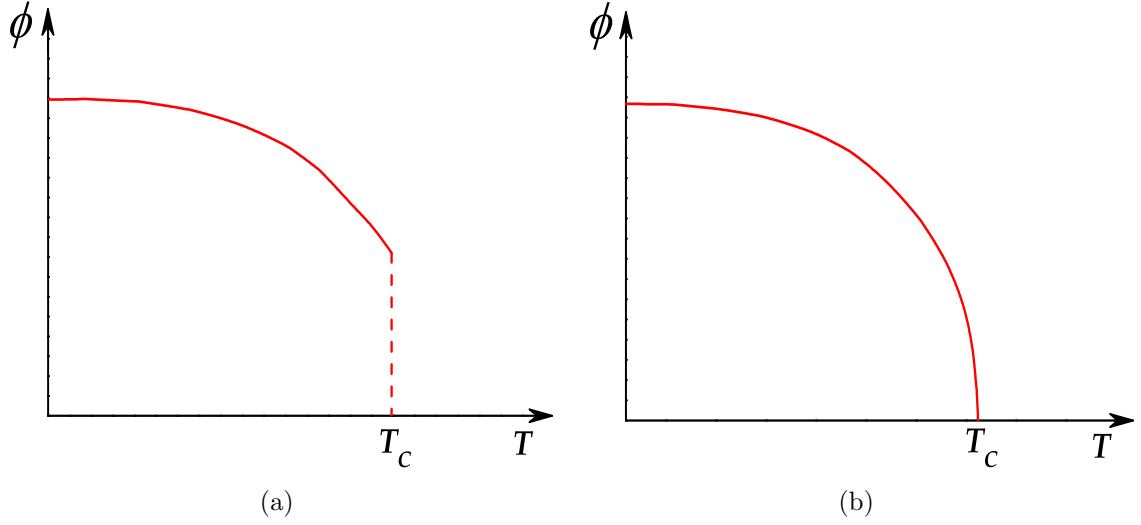


Figure 1.4: Order parameter as a function of temperature for (a) first order phase transition and (b) second order phase transition. Recreated from ref. [7].

of the order parameter ϕ for a temperature driven transition is then given by^{1,7}

$$G(T) = G_0(T) + A(T)\phi^2 + u_3\phi^3 + u_4\phi^4 + \dots, \quad (1.2)$$

where G_0 includes all the contributions to the free energy which do not arise from the order parameter. There is no term which is of first order in ϕ as that would imply a nonzero value of the order parameter above the transition temperature. The coefficient A is chosen such that the free energy in the low-temperature phase is lower than that of the high-temperature phase for a nonzero value of order parameter. This can be achieved by defining $A = a(T - T^*)$ (we shall see the significance of the temperature T^* in the following discussion). The presence of the third order term is decided by the symmetry of the order parameter. If the order parameter is a scalar, the third order term can be present. Whereas, if the order parameter is a vector (spontaneous magnetization, for example), then a third order term would imply that the free energy in the ordered state would depend on the orientation of the order parameter, which is physically not possible. For a global stability to occur, the coefficient of the fourth order term is always positive.

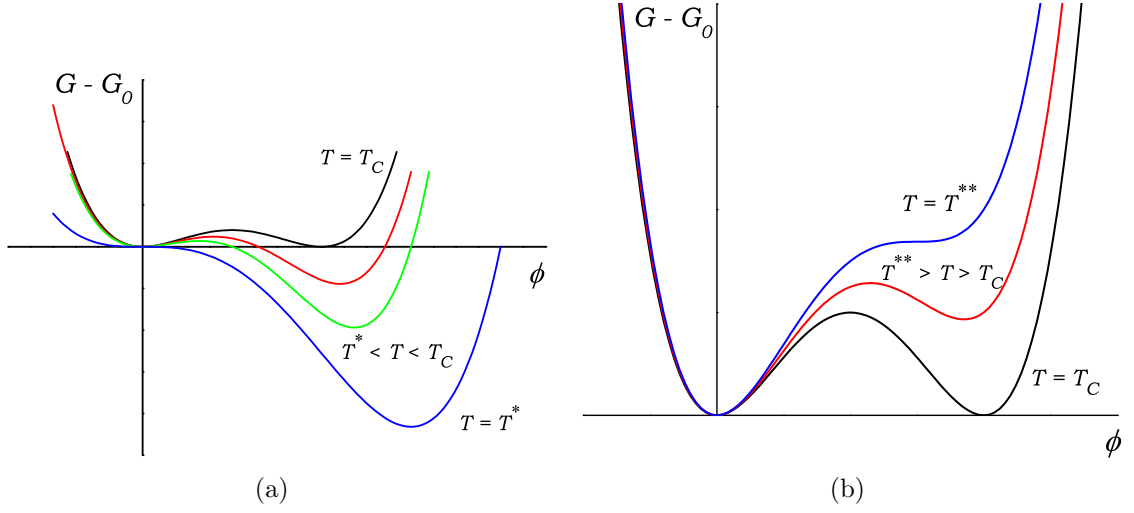


Figure 1.5: Plots of free energy as a function of order parameter as described in equation 1.2. (a) Free energy during cooling and (b) Free energy during heating. Recreated from ref. [7].

We focus our discussion only on first order transitions as the results presented in this work are based on the first order transition in the Fe-Rh alloy system. A first order transition can occur if the coefficient of the third order term in equation 1.2 is negative.⁷ In case of second order transitions, the third order term is absent.^{1,7}

Figure 1.5 shows the plots of free energy as a function of order parameter from equation 1.2 for different temperatures. At a temperature $T = T_C$, there are two minima of equal value in the free energy curve, one at the zero value of order parameter and one at a nonzero value, which means that the order parameter can change discontinuously at $T = T_C$, as shown in figure 1.4 (a). Thus the system can exist in any one of the two phases, *ordered* or *disordered* at this temperature. This temperature is defined as the thermodynamic transition temperature as the free energies in both the phases are equal. However, for the actual transition to occur during cooling (figure 1.5 (a)), the energy barrier between the ordered and disordered state has to be surmounted. This allows the disordered (or high temperature) phase to be *supercooled*, i.e. to retain it as a metastable phase till the temperature T^* . At $T = T^*$, there is no minimum at the zero value of order parameter and the system transforms from a disordered state to the ordered state by an infinitesimal energy fluctuation. It is no

longer possible to supercool any further. Thus T^* is termed as the *limit of metastability* during cooling or the *limit of supercooling* for the high temperature phase, below which the system will always be in the stable low temperature phase.⁷

During the heating cycle, the system can be *superheated* till the temperature $T = T^{**}$. At T^{**} , there is only one minimum at the zero value of order parameter and the system transforms to the disordered state. T^{**} is thus the limit of metastability (or superheating) for the low temperature phase. However in a real system, energy fluctuations are always present due to finite temperature, which can help in crossing the barrier and the actual transition during cooling may take place somewhere between $T = T_C$ and $T = T^*$. Whereas during heating, the transformation may actually take place between $T = T_C$ and $T = T^{**}$. This explains the hysteresis across a first order transition.

First order transition can also occur when the odd order term in equation 1.2 is prohibited by symmetry like in case of field-induced antiferromagnetic to ferromagnetic (metamagnetic) transitions. Equation 1.2 is then modified to take into account only the even order terms and the free energy is expressed as⁷

$$G(T) = G_0(T) + A(T)\phi^2 + u_4\phi^4 + u_6\phi^6. \quad (1.3)$$

Here a first order transition can arise when u_4 is negative. Figure 1.6 shows the plot of free energy as a function of order parameter as in equation 1.3. A secondary minimum of order parameter appears at negative values, which implies that both negative and positive values of order parameter are equally likely across the phase transition. Here also metastable states can be seen during cooling and heating with the respective limits being T^* and T^{**} .

The expression for the free energy in equations 1.2 and 1.3 is valid for only pure systems where the behaviour at any single point of the sample is the same for the entire sample volume. However, in case of real samples, disorder is always present

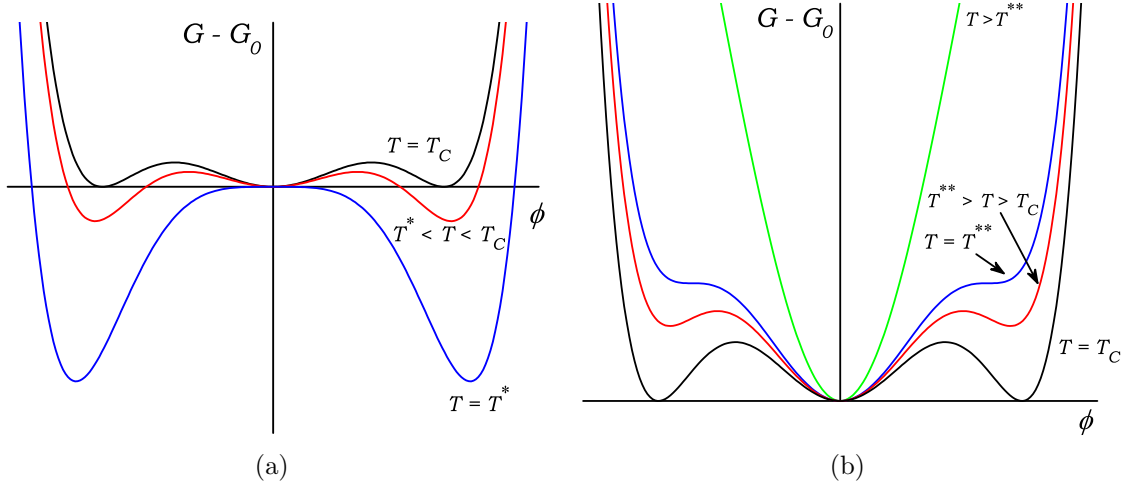


Figure 1.6: Plots of free energy as a function of order parameter as described in equation 1.3. (a) Free energy during cooling and (b) Free energy during heating. Recreated from ref. [7].

as discussed in the earlier section. In such cases, the disorder site can act as the nucleation centre for a finite value of order parameter to appear. Thus the spatial dependence of the order parameter also needs to be taken into consideration. The expression for free energy in such cases is given by⁸

$$G = \int G(\mathbf{r})dV, \quad (1.4)$$

with

$$G(\mathbf{r}) = G_0 + A\phi^2(\mathbf{r}) + u_4\phi^4(\mathbf{r}) + u_6\phi^6(\mathbf{r}) + D(\nabla\phi)^2 + \Delta A(\mathbf{r})\phi^2(\mathbf{r}). \quad (1.5)$$

Here $\Delta A(\mathbf{r})$ is the defect induced change in the coefficient A of equation 1.2, and $(\nabla\phi)^2$ gives the spatial dependence of the order parameter. However, such a modification does not discuss the *mechanism* by which there can be a spatial distribution of the order parameter. For example, a defect in a ferroelectric material may act as an electric dipole which changes the local configuration of the electric field and thus cause the transition at a different value of temperature compared to the case of a pure system. Whereas, the mechanism of the spatial variation of the order parameter in a

ferromagnetic metal with the presence of defects could be quite different. The term $A(\mathbf{r})$ consists of the transition temperature as discussed earlier. Thus the defect site can *locally* change the transition temperature compared to the bulk thermodynamic critical temperature. Thus at different pockets of the sample, there can be a situation where the order parameter appears at different values of temperature thereby smearing the transition when observed over the entire bulk.⁸ Close to the transition temperature, the defects cannot be treated as independent because the correlation between the ordered pockets starts building up.⁸ One of the ways in which the correlation from one ordered pocket of the sample can be *transmitted* to another pocket is through the strain experienced by the sample matrix during a structural transition.⁹ We discuss this issue in details later in connection with the experimental results obtained during the local imaging of the first order magneto-structural transition in Fe-Rh alloy.

1.2 Hysteresis across a disorder influenced first order transition

We now see how the hysteresis across a first order transition is influenced by disorder. Figure 1.7(a) shows the evolution of phase fraction as a function of temperature for two cases, 1) system without any disorder and 2) system in presence of small amount of disorder, where the discontinuity across the transition is only reduced in magnitude but not completely rounded off. Figure 1.7(b) shows that situation where substantial disorder is present in the sample which completely rounds off the discontinuity. We now see the detailed features of the phase transition and the associated hysteresis in all these cases. We follow the arguments given by Chattopadhyay et al.¹⁰ to observe the nature of hysteresis in case of disorder influenced first order transitions. The phase fraction is calculated with respect to the high temperature phase. So at low- T ,

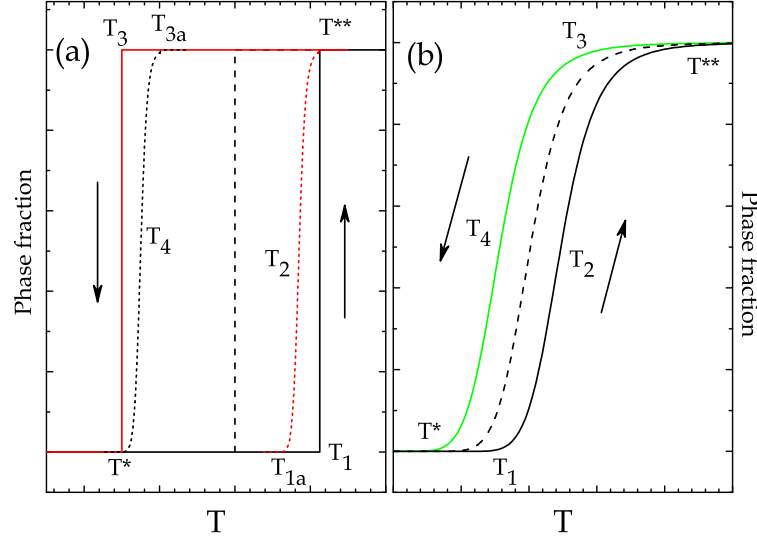


Figure 1.7: Influence of disorder on the hysteresis across a first order transition. The phase fraction is plotted as a function of temperature. See text for details. Recreated from ref. [10].

the phase fraction is zero and at high- T the phase fraction is unity.

- (1) **Hysteresis in pure system:** The discontinuity at the thermodynamic transition temperature is plotted as a dashed line in figure 1.7(a). The evolution of phase fraction for this case is plotted as a solid line. The low- T phase can be superheated up to a temperature T_1 where it suddenly transforms to high- T phase. This temperature marks the limit of metastability of the low- T phase and is denoted as T^{**} following the standard notation discussed earlier.⁷ While cooling, the high- T phase can be supercooled down to T_3 and transforms entirely to low- T phase at T^* , which is the limit of supercooling of the high- T phase. In this situation, phase coexistence cannot be observed as the entire sample transforms from one phase to the other at a single temperature.
- (2) **Hysteresis in presence of small amount of disorder:** The phase fraction for this case is plotted as a dotted line in figure 1.7(a). The onset of the transition while heating is at T_{1a} , which is above T_c and the transition completes at T^{**} . T_2 is the temperature at which the curvature of the phase fraction with respect to temperature changes from positive to negative. During cooling, the

phase fraction follows the path $T_{3a} - T_4 - T^*$. T_4 is that temperature where the curvature of the graph changes sign. Here $T_{3a} < T_{1a}$ i.e the onset of the low- T phase while cooling occurs at a lower temperature than the onset of the high- T phase while heating. This relation between the onset temperatures is similar to the case of the transition in a pure system. However, signatures of phase coexistence can be observed in this case.

- (3) **Hysteresis in presence of large amount of disorder:** In case of a large amount of disorder (see figure 1.7(b)), the transition is completely rounded off. The onset of the transition while heating takes place at T_1 and the phase fraction follows a path along $T_1 - T_2 - T^{**}$. While cooling, the phase fraction follows a path along $T_3 - T_4 - T^*$, where T_3 is the onset temperature. The sample transforms from the low- T phase to the high- T phase through a phase coexistent state where the product phase nucleates heterogeneously in the parent matrix. Another thing to be noted here is the relation between the onset temperatures of both the phases. Here $T_3 > T_1$, which means that the onset of the low- T phase actually takes place at a higher temperature than the onset temperature of the high- T phase. This situation is quite opposite to the two situations discussed earlier. We thus see that disorder can not only smear off the discontinuity but also can influence the onset temperatures of the two phases.

Bulk measurements to observe the characteristic signatures of disorder influenced first order transition have been performed on a variety of systems like first order transition in vortex matter, and first order magnetic transition in intermetallics (see Roy and Chaddah¹¹ for a comprehensive review). We use some of that understanding for explaining the results presented in this work. With this phenomenological background on first order phase transitions, we now briefly revisit some of the existing information on the Fe-Rh alloy system which formed the background and motivation behind the work presented here.

1.3 The Fe-Rh alloy system

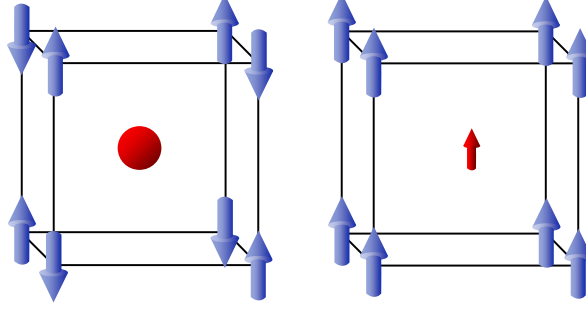


Figure 1.8: The lattice and magnetic structures of Fe-Rh in the antiferromagnetic and ferromagnetic phase. The Fe atoms reside at the corners. The magnetic structure shown at the left is for the antiferromagnetic phase. The Rh atom carries a magnetic moment in the ferromagnetic phase. Recreated from ref. [12].

The nearly equi-atomic Fe-Rh alloy is known to show a first order transition during heating from an antiferromagnetic to ferromagnetic state slightly above room temperature and a second order transition from the ferromagnetic to paramagnetic state at about 675 K.¹³ The alloy system initially generated interest because magnetization measurements showed an anomalously large magnetic moment in the ferromagnetic phase.¹³ The temperature dependent magnetization in the ferromagnetic phase could be fitted with the Brillouin function with the total angular momentum $J = 1$. The average atomic moment was found out to be $1.85 \mu_B$ from the saturation magnetization. The composition of the alloy was $\text{Fe}_{48}\text{Rh}_{52}$. This gave an average moment per iron atom as $3.85 \mu_B$, which is unusually large considering the moment of iron atom in pure bulk iron, which is $2.2 \mu_B$. This indicated that the Rh atom must be carrying a magnetic moment in the ferromagnetic phase, which was later verified by neutron scattering experiments¹⁴ and ab-initio calculations.^{12,15}

The Fe-Rh alloy has a CsCl type crystal structure (see figure 1.8) in the low-temperature antiferromagnetic phase. The same structure is retained in the high-temperature ferromagnetic phase with a 1% discontinuous increase of volume.¹⁶ The discontinuous volume change can also be induced by the application of magnetic

field.¹⁶ The transition in the nature of magnetic ordering which depends on the lattice constant hinted towards a mechanism where the inversion of the sign of exchange interaction is related to the lattice parameter.¹⁷ However, it was shown that the model of exchange inversion leads to serious numerical discrepancies in accounting for the temperature dependence of critical fields (the field required for the antiferromagnetic to ferromagnetic transition)¹⁸ and the excess entropy in the ferromagnetic state.¹⁹ The excess entropy apart from the expected lattice entropy was thought to arise from the increase in magnetic entropy in the ferromagnetic state.¹⁹ The magnetic and electrical transport properties of the nearly equiatomic alloys was shown to be extremely sensitive to concentration.²⁰ Addition of small amount of Ni and Pd shifts the antiferromagnetic to ferromagnetic transition to lower temperatures and magnetic fields.²¹ The magnetic transition which is coupled to a structural change prompted pump-probe experiments using femtosecond laser pulse to determine if the lattice distortion drives the magnetic transition or vice-versa.^{22,23} It was observed in these measurements that the instability in the magnetic lattice occurs earlier to the structural transition.

While most of the attention was focused on the microscopic origin of the transition and the exact nature of the magnetic structure in both the phases, the technological applications of the alloy were also explored. A technologically important functionality like the giant magnetocaloric effect was reported near the room temperature.^{24,25} A large adiabatic temperature change of more than 12 K for a field excursion of nearly 2 T was observed.²⁴ The other functionalities that were observed near room temperature were the giant elastocaloric effect,²⁶ giant magnetostriction,²⁷ and giant magnetoresistance.²⁸ Artificial structures made from FeRh/FePt have been proposed for thermally assisted magnetic recording media.²⁹ We now think that such wide range of functionalities of this alloy system arise due to the underlying first order magneto-structural transition close to room temperature.

However, it was believed that though the Fe-Rh alloy shows a wide range of important functional properties, the functionalities like the giant magneto-caloric effect actually vanish after the first field cycle.^{25,30,31} In this work we solve this long-standing problem and show that the possible role of phase coexistence across the first order phase transition in tuning the functional properties of this material has largely gone unnoticed. We also show that the thermomagnetic history effects that arise across a disorder influenced first order transition are generic to any other first order transition induced by both temperature and magnetic field and are not limited to only the Fe-Rh system. Our work presented in the following chapters highlights that it is necessary to understand the nucleation and growth mechanism across a first order transition, apart from having a large value of the functional property (e.g. magnetocaloric effect or magnetostriction), if such materials are to be used for reproducible technological applications under multiple temperature or magnetic field cycles.

In the following chapters, the results obtained during the course of this work are presented in a manner which carries the thread of disorder influenced first order transition and connects the various experimental results observed in different measurements. Chapter 2 discusses about the experimental methods used to obtain the results presented here. The local imaging of phase coexistence and metastability across the antiferromagnetic to ferromagnetic transition in the parent Fe-Rh alloy is presented in chapter 3. Chapter 4 discusses about the nucleation and growth dynamics across the first order transition in one of the Ni doped Fe-Rh alloys. The evolution of phase fraction across a temperature and magnetic-field induced transition is shown to be analogous to the dynamics seen during crystallization of a solid from melt. The inference of the fraction of the transformed phase is based upon the assumption that different microscopic locations of the sample have their own independent hysteresis across the transition. Chapter 5 further explores this assumption to

understand the general features of minor hysteresis loops within the hysteretic region across the transition. The minor hysteresis loops are modeled by using the Preisach model of hysteresis by establishing its equivalence with the landscape picture of transition temperatures across a disorder influenced first order transitions. Chapter 6 discusses the thermomagnetic history effects in isothermal measurements across the first order transition in the parent Fe-Rh and the Ni doped Fe-Rh alloys and provides a solution to the long-standing problem of the lack of repeatability of the magnetocaloric effect in this alloy system. The thermomagnetic history effects are shown to be generic to any first order transition driven by temperature and magnetic field. Chapter 7 discusses yet another kind of thermomagnetic history effects across the temperature driven transition. Dynamical features usually associated with structural glasses are observed across the ferromagnetic to antiferromagnetic transition during cooling. Chapter 8 summarizes the work presented in this thesis and discusses about the future plans based on the present work.

Chapter 2

Experimental methods

This chapter deals with the experimental methods used for obtaining the results presented in this work. We first discuss the sample preparation and characterization methods and then discuss the measurement techniques which are used to study the physical properties of the samples under investigation.

2.1 Sample preparation and characterization

2.1.1 Arc-melting

The samples of Fe-Rh and Ni doped Fe-Rh alloys were prepared in a commercial argon arc melting furnace (Centorr Vacuum Industries, Model 5TA Reed tri-arc furnace), whose actual photograph is shown in figure 2.1. This furnace consists of upper and lower water-cooled sections separated by a quartz observation tube. Electrical power and water are fed to each of these sections by water-cooled power cables. The three copper stinger rods carry the tungsten electrodes, which are used for striking the arc. The copper hearth is inserted in this arrangement through a tapered opening in the bottom section. Provision is made for attaching a vacuum pump for evacuation prior to backfilling with argon. Ports are provided for argon gas inlet and outlet.

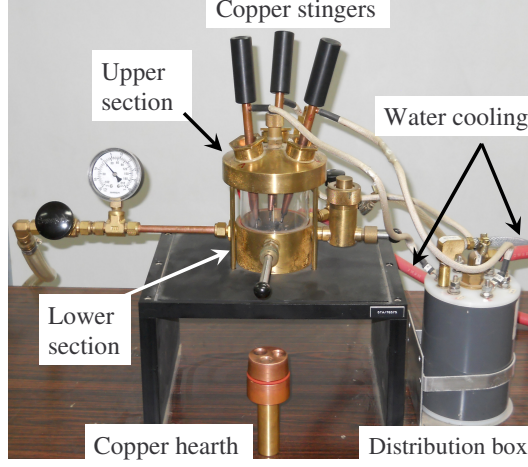


Figure 2.1: Photograph of the arc-melting furnace used for sample preparation.

Pure elements which are supposed to be melted are placed in the cup of the hearth after weighing them in desired proportions. The furnace is then purged by a mechanical pump, followed by backfilling with argon. Once the system is purged and the desired power setting on the power supply is set, the electrodes are brought to a position near the edge of a titanium getter and an arc is struck. This piece of titanium is melted prior to melting the specimen to remove any possible impurity in the argon atmosphere from the furnace cavity. The same procedure is repeated without breaking the argon atmosphere for melting the elements to get the sample. The specimen is turned over and remelted several times to ensure homogeneity.

After obtaining the sample button, the alloy was sealed under argon atmosphere in quartz ampules and subjected to the following heat-treatment schedule: 48 hours at 1100°C, cooled to 800°C at the rate of 2°C per minute, maintained for 24 hours at 800°C and then cooled to room temperature at the rate of 2°C per minute. This annealing schedule is similar to the one followed in case of FeRh_{1-x}Pt_x alloys.³² We have followed the same annealing schedule for all the alloys used in this work. The button is then cut into pieces with the help of a diamond wheel and characterized for crystal structure and composition.

2.1.2 X-ray diffraction

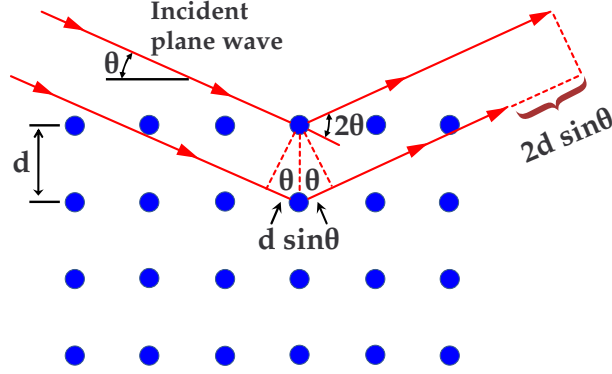


Figure 2.2: Schematic of x-ray diffraction from a set of atomic planes.

The crystal structure of a solid can be determined by the diffraction of x-rays as their wavelength is of the order of the periodic distance between atoms occupying the lattice sites.³³ The schematic of such diffraction is shown in figure 2.2. The Bragg law of diffraction states that the condition for constructive interference to occur for the reflected beam is given by:³³

$$2d \sin\theta = n\lambda, \quad (2.1)$$

where d is the interplanar spacing, θ is the angle of incidence, n is the order of diffraction and λ is the wavelength. Instead of considering the n^{th} order diffraction from the set of planes with distance d , the law can be modified to consider only the first order diffraction from a set of planes with d/n interplanar distance. The law then becomes:

$$2d_{hkl} \sin\theta = \lambda, \quad (2.2)$$

where h, k, l are the miller indices.

One x-ray diffraction pattern of the parent Fe-Rh alloy using the powder method is shown in figure 2.3. The diffraction pattern was recorded using a commercial x-ray

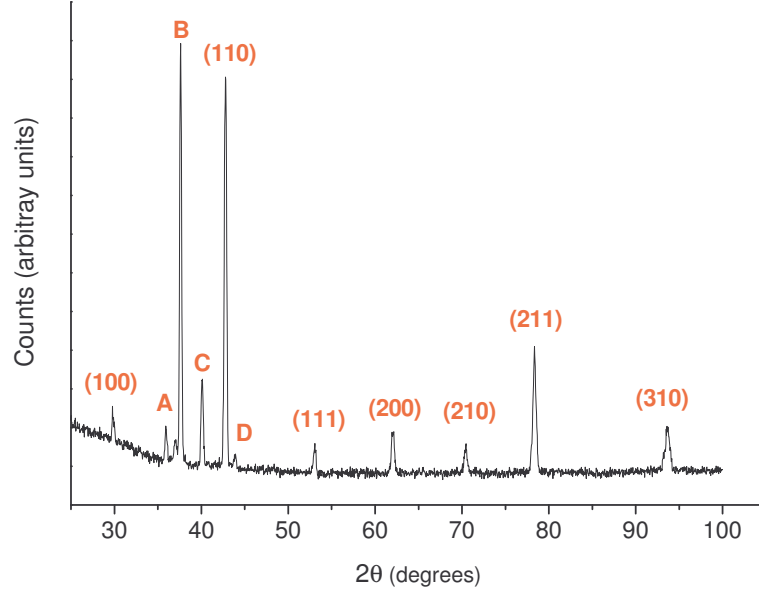


Figure 2.3: X-ray diffraction pattern for the parent Fe-Rh alloy used in this work.

diffractometer with Cu K_{α} radiation (PANalytical X’Pert PRO Materials Research Diffractometer (MRD)). The peaks ‘A’, ‘B’, ‘C’ and ‘D’ arise from the sample holder block, which were verified by taking a *blank* run without any sample. The remaining peaks could be indexed for a CsCl type structure with a lattice parameter of 2.986 Å, which matches quite well with the earlier reports.³⁴

2.1.3 Energy dispersive spectroscopy

The composition and homogeneity of the samples were determined by using a commercial scanning electron microscope equipped with a energy dispersive spectrometer (Philips XL-30PC). In energy dispersive spectroscopy, the sample is exposed to high energy electrons, which interact with the atoms inside the solid to give characteristic x-ray photons, which are the signatures of the elements present in the material.³⁵ The schematic of such process which can be initiated by either an electron or photon is shown in figure 2.4.

When high energy electrons strike a specimen, they produce either elastic or inelastic scattering. Elastic scattering produces the backscattered electrons, which are

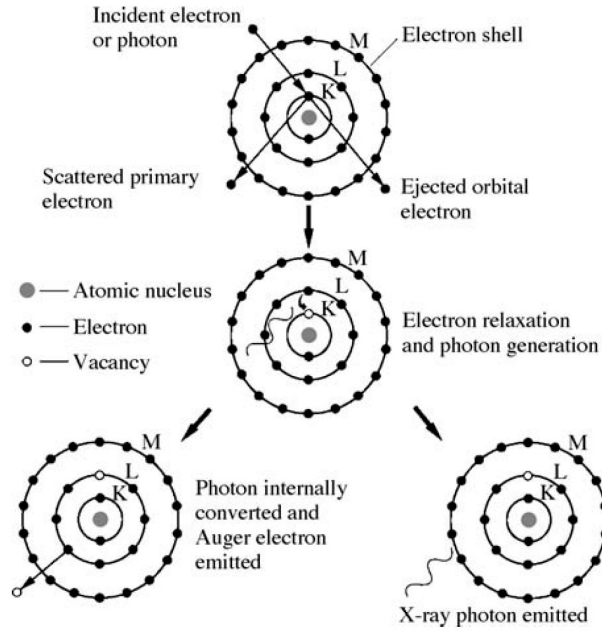


Figure 2.4: Schematic of excitation of a characteristic X-ray photon by a high energy electron or photon. Reproduced from ref. [35].

incident electrons scattered by the atoms in the specimen. Inelastic scattering produces secondary electrons, which are electrons ejected from the atoms in the specimen.³⁵ The schematic of this interaction of the electron beam with the material specimen is shown in figure 2.5. Both these type of electrons can be used for imaging while simultaneously acquiring the spectrum of the emitted x-rays.

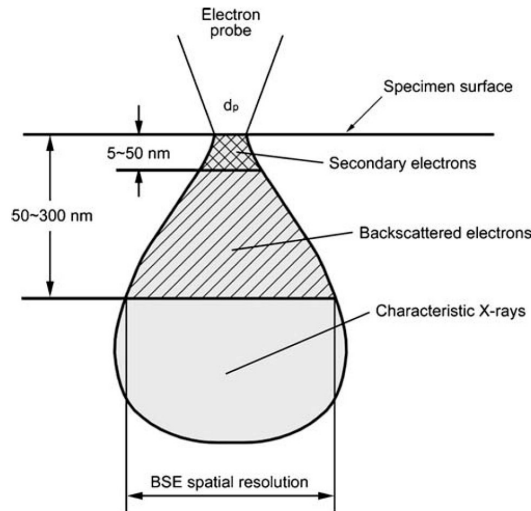


Figure 2.5: Interaction of the electron probe and specimen atoms below a specimen surface. BSE refers to the backscattered electrons. Reproduced from ref. [35].

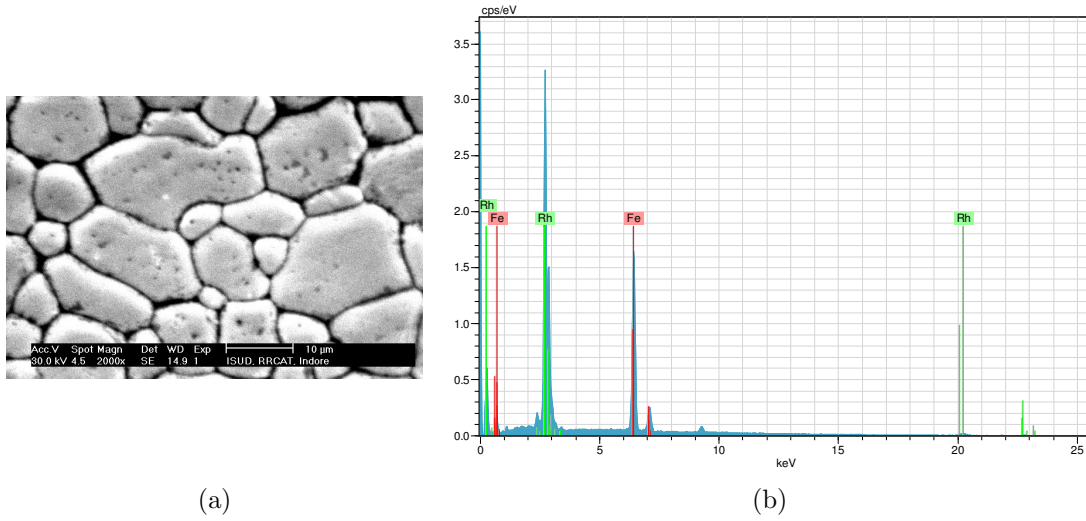


Figure 2.6: (a) Microstructure of the Fe-Rh alloy using the secondary electrons for imaging and (b) The spectrum obtained for the parent Fe-Rh alloy using Energy Dispersive Spectroscopy.

One typical microstructure using the secondary electrons and the energy dispersive spectrum for the parent Fe-Rh alloy are shown in figure 2.6. The energy dispersive spectrum is taken at various locations of the sample and the composition is determined through a software routine, included with the spectrometer, which takes into account the relative intensities of the characteristic x-rays emitted by the sample. The homogeneity of the alloy is confirmed by determining the composition at various locations.

2.2 Measurement of physical properties

2.2.1 SQUID magnetometer

A commercial Superconducting Quantum Interference Device (SQUID) magnetometer (MPMS-5, Quantum Design USA) was used to measure dc magnetization as a function of temperature and magnetic field.

The MPMS-5 is based on a radio frequency SQUID which has a single josephson junction. A single junction SQUID is based on the ac josephson effect.³⁷ The

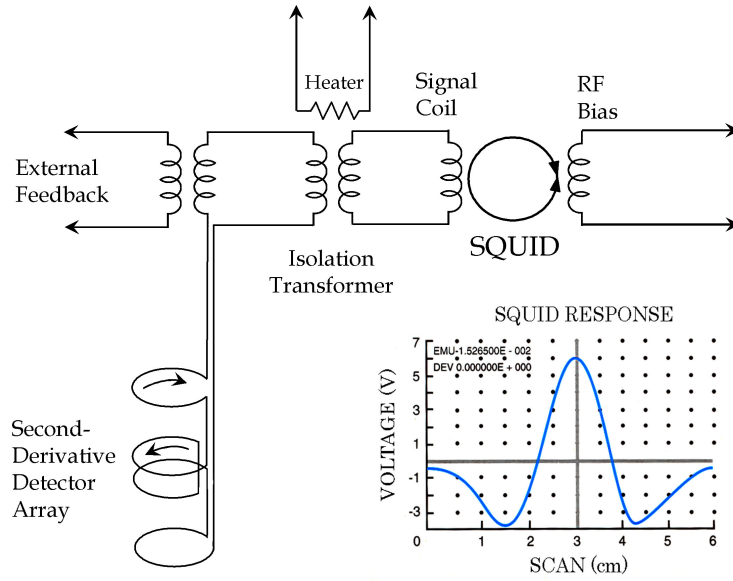


Figure 2.7: Schematic of a SQUID magnetometer detection system. Reproduced from ref. [36].

schematic of the MPMS-5 detection system is shown in figure 2.7. The detection system consists of a superconducting second derivative gradiometer coil assembly through which the sample is translated. The induced emf due to the motion of the sample, which carries a magnetic moment is then inductively coupled to the SQUID sensor through a shielded superconducting isolation transformer. The SQUID sensor also forms a part of a radio frequency biased resonant tank circuit. Before any measurement, the heater is used to drive both sides of the transformer to normal to get rid of any persistent currents in the circuit. Depending on the flux linked with the SQUID, the inductance of the tank circuit changes, which leads to the change in its resonant frequency. This change in the resonant frequency appears as a change in the voltage amplitude of the tank circuit and is periodic in units of the flux quantum Φ_0 .^{37,38} The flux linked with the SQUID sensor is related to the magnetic moment of the sample, which thus makes it possible for using the SQUID sensor for measuring magnetization. The resulting SQUID profile is shown in the bottom right corner of figure 2.7. The magnetic moment is inferred by fitting this profile with that of an ideal magnetic dipole.^{36,39}

2.2.2 Vibrating Sample Magnetometer

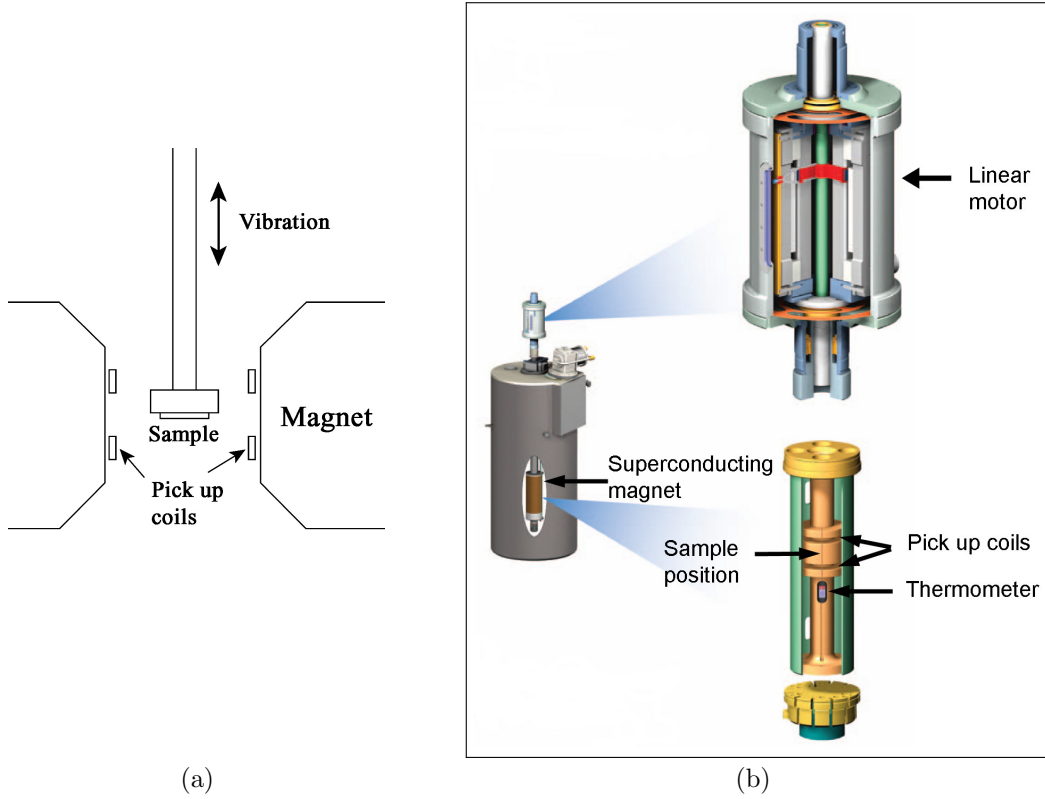


Figure 2.8: Schematic of a Vibrating Sample Magnetometer. Reproduced from refs. [40] and [41].

The vibrating sample magnetometer (VSM) is based on the Faraday's law of electromagnetic induction, where the induced emf in a pick-up coil is proportional to the rate of magnetic flux change through the coil. To measure the magnetization of the sample, the sample is vibrated at low frequency by a linear motor situated at the top of the cryostat. The flux change which results due to this vibration, induces an emf in the pick-up coil. The linear motor is driven by a sinusoidal waveform which acts as a reference to the lock-in amplifier. The induced emf in the pick-up coil is detected by the same lock-in amplifier to measure the signal at the same frequency as the drive frequency. The schematic of the magnet and pick-up coil arrangement in a typical VSM is shown in figure 2.8a.⁴⁰ The schematic of the VSM used in the present study is shown in figure 2.8b.⁴¹

2.2.3 Linear strain

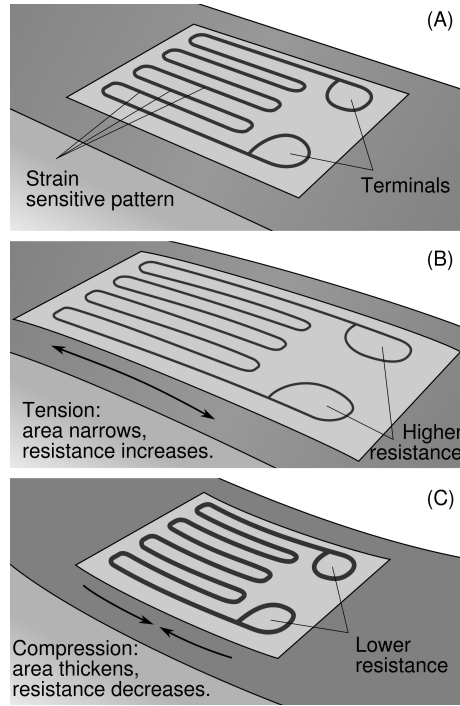


Figure 2.9: Schematic of the strain gauge used in the present study. Reproduced from http://en.wikipedia.org/wiki/Strain_gauge

Linear strain as a function of temperature and magnetic field was measured in home-made instruments. The strain was measured using the standard strain gauge technique. A commercial strain gauge was used in this study to measure the change in linear dimensions of the sample (model CFLA-1-350-11, Tokyo Sokki Kenkyujo Co., Ltd.). The strain gauge consists of a metallic geometrical pattern embedded in a polymer film as shown in figure 2.9A. When the gauge is stretched along the length, the metallic wire becomes longer and thinner which results in the increase of its electrical resistance (see figure 2.9B). When the gauge is compressed, the length decreases and the diameter of the wire increases which results in decrease of resistance (see figure 2.9C). Thus the change in electrical resistance can be measured to know the strain experienced by the strain gauge. The resistance of the strain gauge also changes due to the temperature dependence of resistivity and thermal expansion/contraction of

the metallic wire used in the gauge. These contributions, viz.: external stress on the gauge arising from the change in dimensions of the sample, resistance change due to thermal expansion/contraction of the strain gauge and the temperature dependence of resistivity of the strain gauge material, need to be separated to obtain the true value of volume change experienced by the sample under consideration. Detailed discussion about this method can be found in ref. [42]. Linear strain as a function of temperature without magnetic field was measured using a homemade liquid nitrogen based apparatus. Magnetostriction was measured using another homemade apparatus built on a commercial superconducting magnet system.⁴²

2.2.4 ac susceptibility

Figure 2.10 shows the schematic of a homemade ac susceptibility apparatus which uses liquid nitrogen as the cryogen. The same apparatus has been used in our earlier studies on different samples.^{43,44} The ac susceptibility set-up consists of a coil system having a primary solenoid and two oppositely wound secondaries, each consisting of nearly 1500 turns. The coil is immersed in liquid nitrogen to ensure that the temperature of the coil remains constant throughout the entire experiment to avoid drifts in the value of the applied field. The sample is mounted on a thin copper strip and inserted in a double-walled quartz insert. The outer (or exchange) space is kept under rough vacuum, while the inner (or sample) space is kept in inert gas (He) environment at a slightly higher pressure than the atmospheric pressure. A temperature controller (Lake Shore DRC-91CA) is used for monitoring and controlling the temperature. The sinusoidal output of a lock-in amplifier (Stanford Research SR830) is supplied to a voltage-to-current converter which drives the current through the coil to generate the necessary ac magnetic field. The signal from the pick-up coil which is proportional to the susceptibility⁴⁵ is measured by the same lock-in amplifier. To obtain the susceptibility in absolute units, the geometrical factor (or

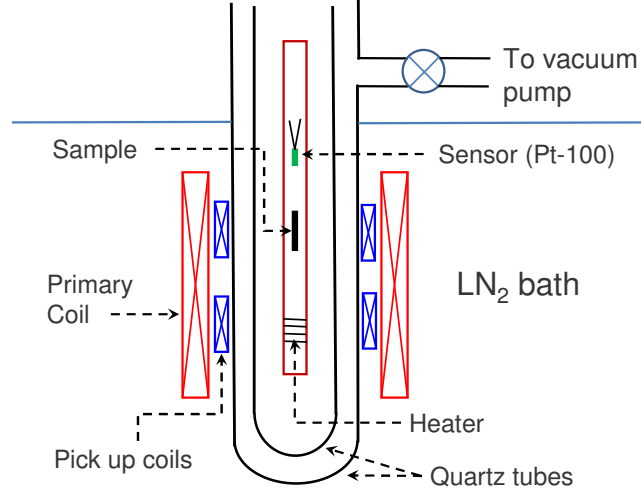


Figure 2.10: Schematic of the home made ac susceptometer.

the calibration factor) between the sample and coil is necessary. Since our samples are not of well defined shape, the susceptibility is expressed in arbitrary units.

2.2.5 Magnetic force microscopy

A typical setup for atomic force microscopy or magnetic force microscopy (\mathcal{MFM}) is shown in figure 2.11. The commercial set-up used in the present study (NT-MDT, SOLVER-PRO) uses a laser light source which is focused onto a flexible, reflective cantilever. The cantilever deflection is detected by using the reflected light which is converted into electrical signal by the four quadrant position sensitive detector.

For magnetic force microscopy, the tip is magnetic which is sensitive to the magnetic field gradients arising from the sample instead of the sample magnetization alone.⁴⁶ Usually, the cantilevers are compliant in only one direction (the z-axis) and are quite stiff in the other two. Thus the force experienced by the tip is given by:

$$F^t = \hat{\mathbf{z}} \cdot [\nabla(\mathbf{m}^t \cdot \mathbf{H}^s)], \quad (2.3)$$

where \mathbf{m}^t is the magnetic moment of the tip and \mathbf{H}^s is the field from the sample.

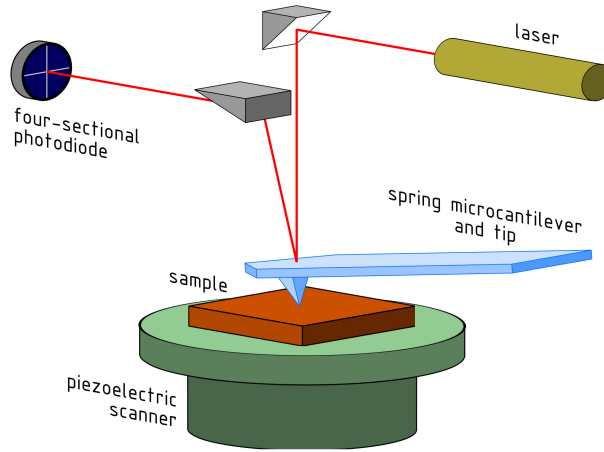


Figure 2.11: A typical atomic force microscopy setup. The same setup can be used for magnetic force microscopy by using a magnetic tip. Reproduced from http://en.wikipedia.org/wiki/Atomic_force_microscopy

The force gradient is given by:

$$F'^t = \hat{\mathbf{z}} \cdot (\nabla \mathbf{F}^t). \quad (2.4)$$

The equation 2.3 simplifies to

$$F^t = \frac{\partial}{\partial z} (\mathbf{m}^t \cdot \mathbf{H}^s), \quad (2.5)$$

and equation 2.4 simplifies to

$$F'^t = \frac{\partial^2}{\partial z^2} (\mathbf{m}^t \cdot \mathbf{H}^s). \quad (2.6)$$

The task now is to measure the magnetic force or force gradient with the help of the cantilever attached with a magnetic tip. The measurements reported in this work are performed using the ac technique where the cantilever is oscillated at or near its resonance frequency. The \mathcal{MFM} tip in our set-up has a Co/Cr coating on Si cantilever tip where the Cr layer prevents the oxidation of the Co layer. Typical radius of curvature of the tip is 40nm and the tip resonant frequency is about 180 kHz. The typical magnetic field the tip generates is around 0.04 T.

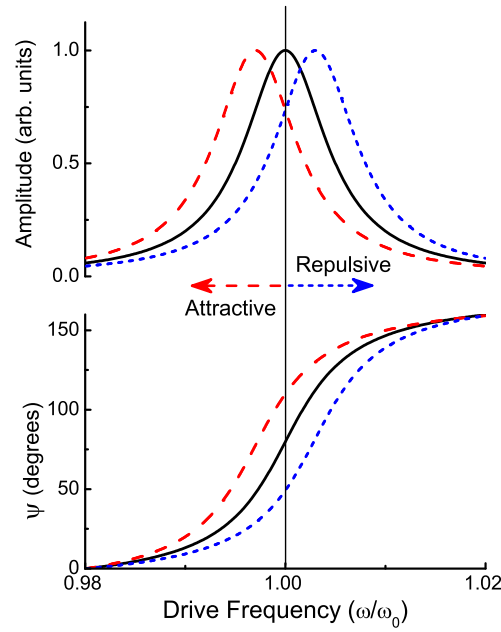


Figure 2.12: Shift in the resonant frequency and phase of the oscillating cantilever of a magnetic force microscope. Recreated from ref. [46].

The magnetic interaction acts through a force gradient on the tip to produce a shift in the resonant frequency (see figure 2.12). This shift in the resonance frequency is detected in terms of shift in the phase of cantilever oscillation.^{46,47} The presence of a ferromagnetic or antiferromagnetic cluster can be inferred by measuring the phase shift. A non-zero phase shift indicates the presence of a ferromagnetic cluster. The map of the phase shift over the scan area constructs the MFM image.

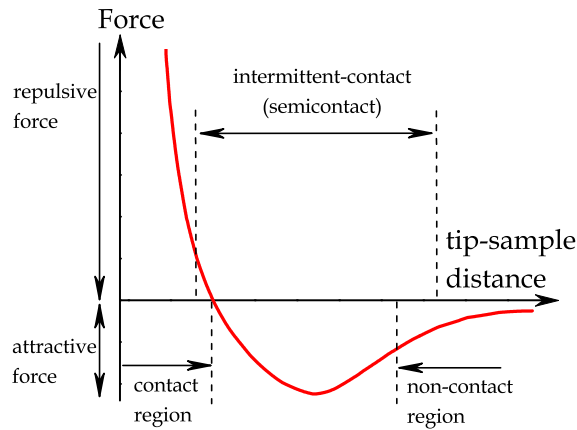


Figure 2.13: The force experienced by the tip of a magnetic force microscope as a function of the distance from the sample. Different regions of the force-distance curve which decide the scan modes are marked.

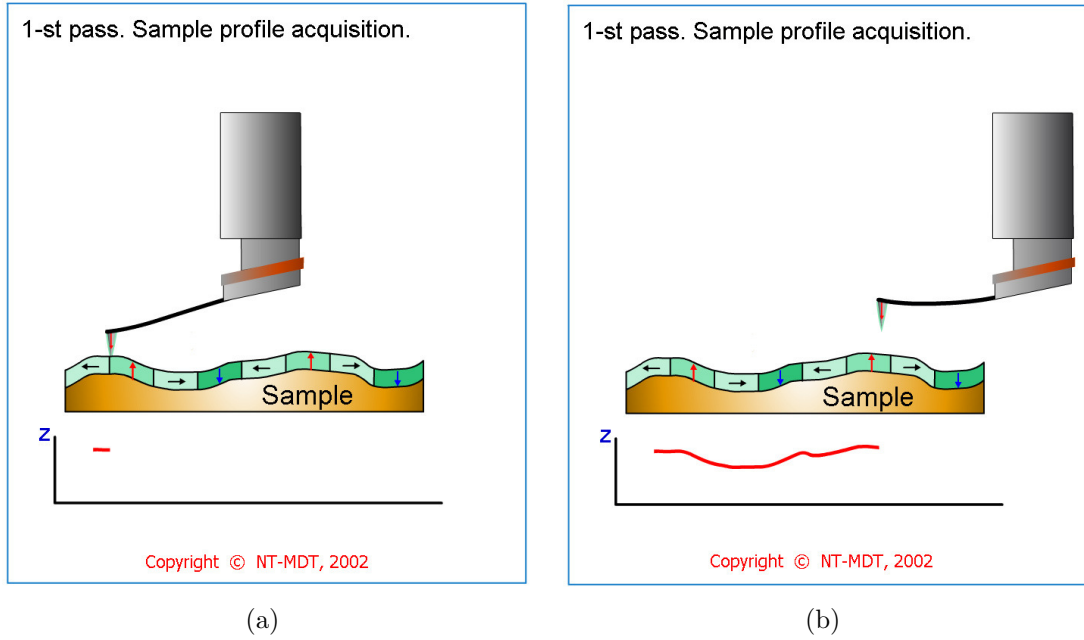


Figure 2.14: Schematic of a magnetic force microscopy scan to acquire the information of the topography of the sample. Reproduced from <http://www.ntmdt.com>

The magnetic information is separated from the topographic information by performing the measurement in two different passes (or scans) over the same region of the sample.

Figure 2.13 shows the force experienced by the tip of the magnetic force microscope as a function of distance from the sample. For acquiring the topographic information, the scan is performed in the semi-contact or the intermittent contact mode (see figure 2.14.) This information of topography is then used as a reference surface for the second pass with the tip lifted by about 30 nm (see figure 2.15).

The feedback to maintain a constant amplitude of oscillation is switched off and the tip is scanned over the reference surface. Thus the second pass measures forces originating mostly from magnetic interaction which fall off much more slowly compared to the van der Waals forces.⁴⁶ The map of the phase change over the sample surface gives the information of the magnetic signal originating from the sample. It is important to cross check if the magnetic force is actually separated from the van der

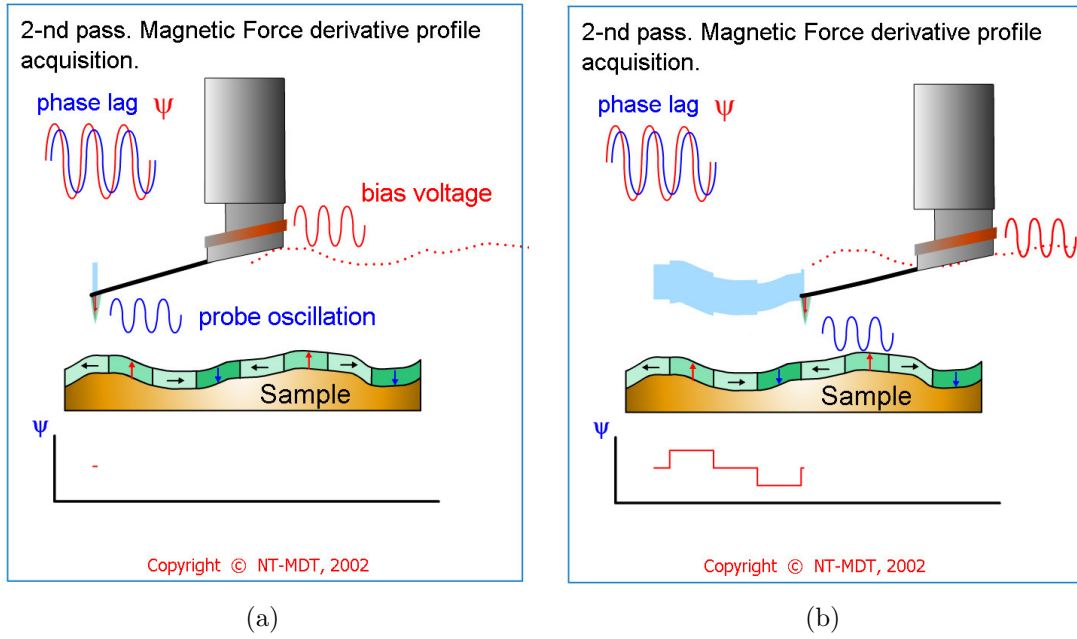


Figure 2.15: Schematic of a magnetic force microscopy scan to acquire the magnetic information. Reproduced from <http://www.ntmdt.com>

Waals forces during the measurement. For this purpose, standard sample like magnetized hard-disk of a computer is used where the topography and magnetic information are not related to each other. We thus see that \mathcal{MFM} provides a unique tool to study the information of the topography and the magnetic signal simultaneously at a length scale of a few tens of nano-metres. This feature becomes useful when we image the magneto-structural transition in the parent Fe-Rh alloy as we see in the next chapter.

Chapter 3

Local imaging of phase coexistence and metastability in Fe₄₈Rh₅₂ alloy

3.1 Introduction

In the first chapter, we described the phenomenology of first order phase transitions and how phase coexistence and metastability across such transitions could be explained. Phase coexistence across a first order magneto structural transition (FOMST) has been a subject of great interest in the context of manganites showing colossal magnetoresistance (CMR)^{48,49} as it is believed to be the cause behind the observed CMR.⁵⁰ Such phase coexistence is now observed in various other classes of magnetic materials like CeFe₂ based pseudobinaries,⁵¹ materials like Gd₅Ge₄ showing giant magnetocaloric effect⁵² and Huesler alloys like Ni-Mn-In,⁵³ suggesting the generality of this phenomenon. Electronic mechanism and chemical disorder alone are unable to explain such multiscale phase coexistence observed even up to the micrometer scale.^{50,54} It has been suggested that a strong coupling between electronic and elastic degrees of freedom is essential for the phase-coexistence to occur in the micrometer scale.^{9,55} Though various methods have been employed to image phase

coexistence, like magnetic force microscopy,⁵⁴ electron microscopy,^{50,56} and scanning tunneling microscopy,⁵⁷ the evidence that strain plays a role in deciding the kinetics of the transition has been at best indirect.^{47,52} It was observed in $\text{La}_{5/8-y}\text{Pr}_y\text{Ca}_{3/8}\text{MnO}_3$ (LPCMO) ($y \sim 0.4$), that the initial nucleation of the ferromagnetic phase occurs at the twin boundaries of the underlying lattice, which suggests that accommodation strain plays a major role in nucleation dynamics across a FOMST.⁴⁷ This material belongs to the family of CMR manganites. In this chapter, we provide an explicit experimental evidence of the intricate relationship between structural and magnetic transition in the intermetallic alloy of Fe-Rh in the sub-micron scale. Our results provide support to the proposed theoretical framework^{9,55} and further emphasize that phase coexistence and metastability are generic features associated with any system undergoing a FOMST and are not limited to only CMR manganites.

In this chapter, we present the results of magnetic force microscopy to image the phase coexistence across the antiferromagnetic to ferromagnetic transition which is coupled with a structural distortion in Fe-Rh. As discussed in chapter 2, magnetic force microscopy offers a unique tool to study the topography and magnetic domains simultaneously. This ability can be used to directly image a magnetostructural transition by monitoring the changes in topography (structural or elastic degree of freedom) along with the changes in magnetic structure. Our results provide direct evidence of strong coupling between the elastic and electronic degrees of freedom seen across this first order magneto-structural transition. Theoretical frameworks⁹ based on long range strain disorder coupling proposed originally for explaining phase coexistence in manganese oxide compounds with colossal magnetoresistance also appear to be applicable for other systems, like intermetallics, undergoing magneto-structural transitions.

3.2 Results and discussion

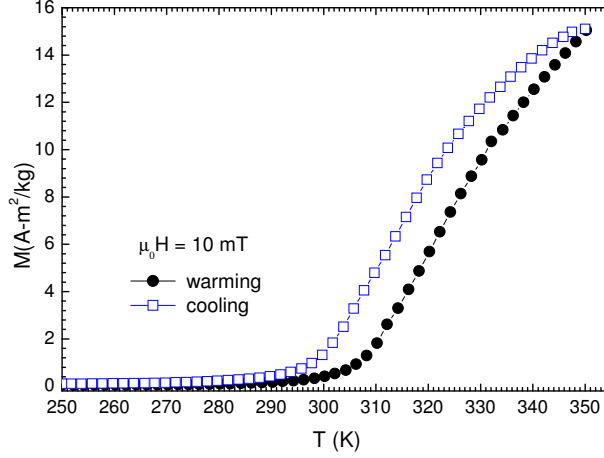


Figure 3.1: Magnetization as a function of temperature of the $\text{Fe}_{48}\text{Rh}_{52}$ alloy, both while heating and cooling in a magnetic field $\mu_0 H = 10$ mT.

Figure 3.1 shows magnetization as a function of temperature of the $\text{Fe}_{48}\text{Rh}_{52}$ alloy in a field of $\mu_0 H = 10$ mT. The onset of the antiferromagnetic to ferromagnetic transition during warming occurs at around 300 K. The transition is not complete even at 350 K which is the maximum temperature possible in our SQUID magnetometer. On cooling, the transition shows a thermal hysteresis of about 10 K. The transition occurs over a large temperature interval, which indicates that the transition proceeds through a heterogeneous nucleation of the product phase in the parent phase. This gives rise to phase coexistent state in the intermediate temperature range. The product phase while warming is the ferromagnetic phase, while that during cooling is the antiferromagnetic phase.

3.2.1 Imaging of phase coexistence

Figure 3.2 shows the 2D image of (a) surface topography and (b) magnetic information at one representative location (scan area: $1\mu\text{m} \times 1\mu\text{m}$) of the sample measured at room temperature ($\sim 298\text{K}$) using the \mathcal{MFM} . This measurement was done on the sample which was not exposed to any temperature cycling after obtaining it from the

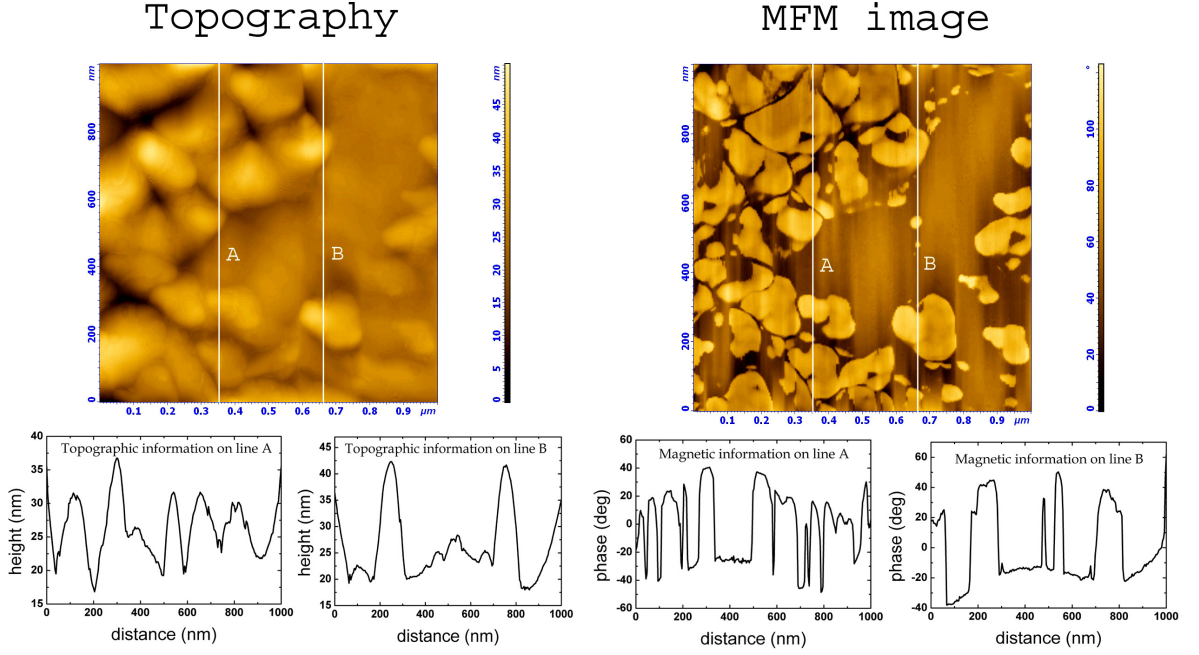


Figure 3.2: 2D image along with raw data of the topography and magnetic information of the annealed $\text{Fe}_{48}\text{Rh}_{52}$ sample before subjecting it to any temperature or field cycles. The raw data is plotted along two representative lines ‘A’ and ‘B’. For creating the image of magnetic information, the reference is shifted to make all values of phase change greater than zero.

annealing furnace. The sample thus has the thermal history of a slow cooling from 1100°C to the temperature of measurement before the \mathcal{MFM} scans. The magnetic field induced by the \mathcal{MFM} tip is considered to be constant during the measurement. With this temperature history, at $\sim 298\text{ K}$ and in the presence of this field of $\approx 0.04\text{ T}$, the sample is expected to have some amount of ferromagnetic fraction in the largely antiferromagnetic state (the sample is still in the hysteretic region of figure 3.1). This coexistence of antiferromagnetic and ferromagnetic clusters is clearly visible on the scale of $1\text{ }\mu\text{m} \times 1\text{ }\mu\text{m}$. The typical sizes of the ferromagnetic clusters range from a few tens of nm to almost 300 nm. Below each images, raw data of the topography and magnetic information are shown along two representative lines marked as ‘A’ and ‘B’.

Apparently some gross features in the topography and the \mathcal{MFM} image (see figure 3.2) seem to be related. However, the raw data clearly show that variations of the topography and magnetic information along the lines ‘A’ and ‘B’ shown in

figure 3.2 are quite different. This difference is expected because the sample was polished at room temperature, which essentially wipes out any correlation (if any) between the magnetic clusters and the surface topographic undulations. Raw \mathcal{MFM} data shows that phase shift changes from almost -40° to $+40^\circ$, whereas the surface topography changes randomly with a peak to peak roughness of about 20 nm. The magnetic part of the signal, which is measured in the second pass of \mathcal{MFM} scan can arise additionally due to ferromagnetic clusters buried inside the surface. The magnetic signal would thus not be related to the surface topography. It should be noted here that the magnetic signal at various locations is not always of the same sign. We have also taken scans at various other locations of the sample. In order to ensure that our \mathcal{MFM} setup can filter out the topographic information from the magnetic part, \mathcal{MFM} imaging of a magnetized hard-disk of a computer was done before the experiments. This is absolutely essential as we later see in figure 3.3 that the changes in topography are related to changes in magnetic structure when the sample undergoes a phase transition.

3.2.2 Time evolution of the magneto-structural transition

After the \mathcal{MFM} measurements, the sample was immersed directly in liquid nitrogen (LN_2). At the boiling point of LN_2 ($\sim 77\text{K}$), the entire sample is in the antiferromagnetic state as can be seen from figure 3.1. The sample was then brought back to room temperature and again the \mathcal{MFM} imaging was done under a field of $\approx 0.04\text{T}$ (\mathcal{MFM} tip field). With this temperature and field history, the sample is now expected to remain mostly in the antiferromagnetic state very close to the onset of the ferromagnetic state as seen through bulk magnetization measurements. This is quite evident from the \mathcal{MFM} image (M0) of figure 3.3 where the ferromagnetic state is yet to develop. The phase shift is only a fraction of a degree. The scan area was increased to $6\mu\text{m} \times 6\mu\text{m}$ to maximize the chance of detecting the ferromagnetic clus-

ters. The length scale of $6\mu\text{m}$ is quite small compared to the average grain size of almost $30\mu\text{m}$. However, since the sample is only polished and not chemically etched, it is not possible to determine in a unique manner if the scan area consists of a grain boundary or not.

To study the time evolution (dynamics) of the antiferromagnetic to ferromagnetic transition, we now focus our attention on the place marked as ‘A’ on the 3D topography and the \mathcal{MFM} image of figure 3.3. At time $t = 0$ (i.e. the first measurement performed after bringing back the sample to room temperature), the place marked ‘A’ on the topography (T0) has a height of about 40 nm and is the largest defect site on the surface. This defect site acts as a nucleation centre for the first nucleus of the ferromagnetic phase. The images (T1) and (M1) in figure 3.3 were obtained after 1 hour. As can be clearly seen the magnetic signal (ferromagnetic state) at location ‘A’ has increased to slightly more than 4^0 . There are a few more locations at the left corner of the image (M1) where additional nucleation centres are visible. The antiferromagnetic to ferromagnetic transition is also coupled to a structural distortion in which the volume of the unit cell in the ferromagnetic phase is slightly larger.¹⁶ Correspondingly, the height of the location ‘A’ has also increased to slightly more than 50 nm (see figure 3.3 (T1)).

The topography (T2) and \mathcal{MFM} (M2) of figure 3.3 were again recorded after another 1 hour ($t = 2$ hrs). New *blisters* appear on the topography and the \mathcal{MFM} image. These regions are marked as 1, 2 and 3. There are also a few more locations at the top corner of figure 3.3(M2) where the nucleation of the ferromagnetic phase takes place. However, their density is much less and their individual magnitude is also slightly smaller. At $t = 2$ hrs, the height of the location ‘A’ has also increased to almost 70 nm with a corresponding increase in the magnetic signal at the same location. This observation shows that not only the growth of individual nucleus but also the formation of newer nuclei is governed by intricate coupling between the

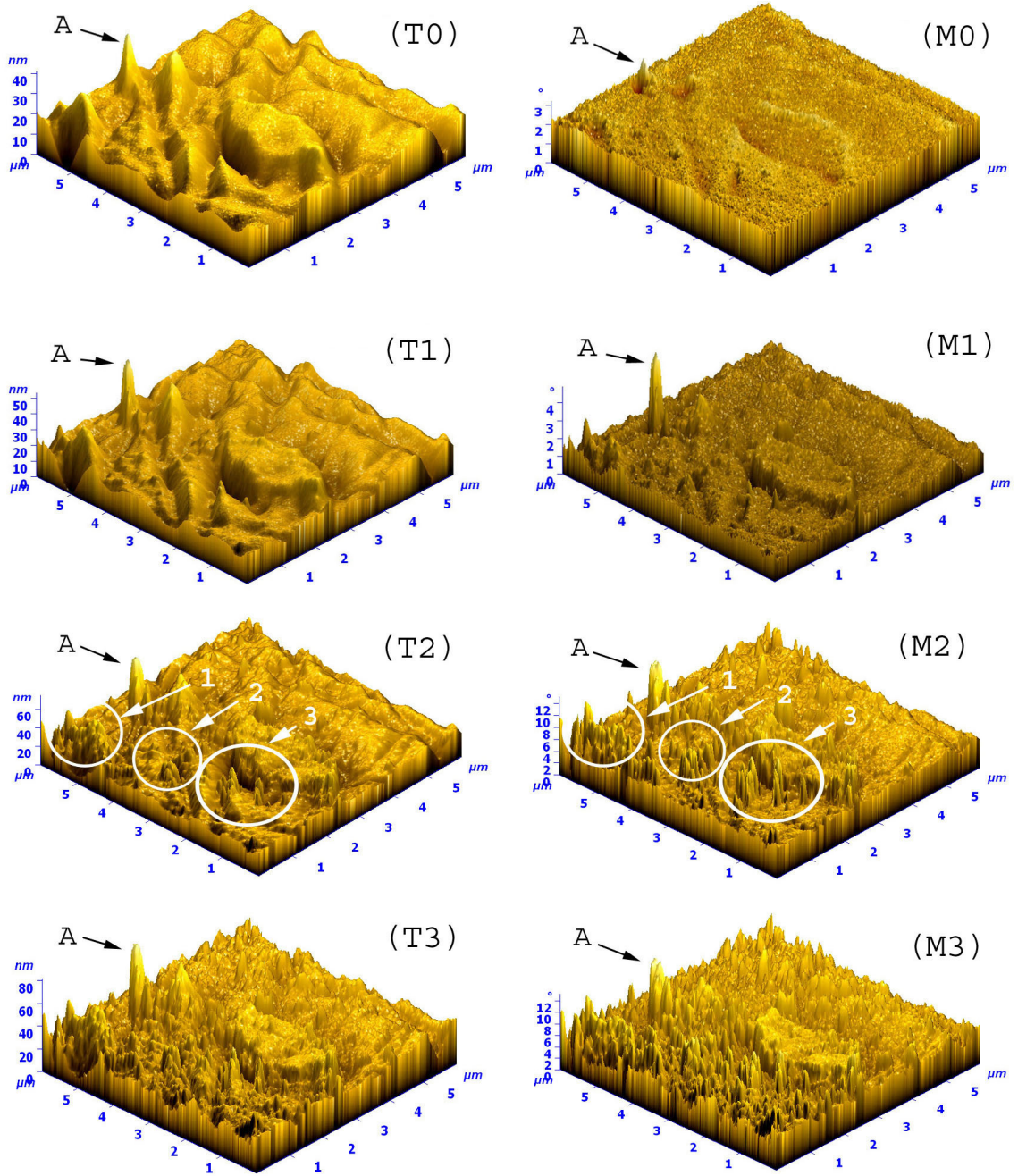


Figure 3.3: Time evolution of topography (T0, T1, T2 and T3) and the corresponding magnetic information (M0, M1, M2 and M3) after the $\text{Fe}_{48}\text{Rh}_{52}$ sample was cooled to liquid nitrogen temperature and brought back to room temperature. Note the change in scale of the \mathcal{MFM} images between M1 and M2, indicating the rise in magnetic signal. For creating the image of magnetic information, the reference is shifted to make all values of phase change greater than zero.

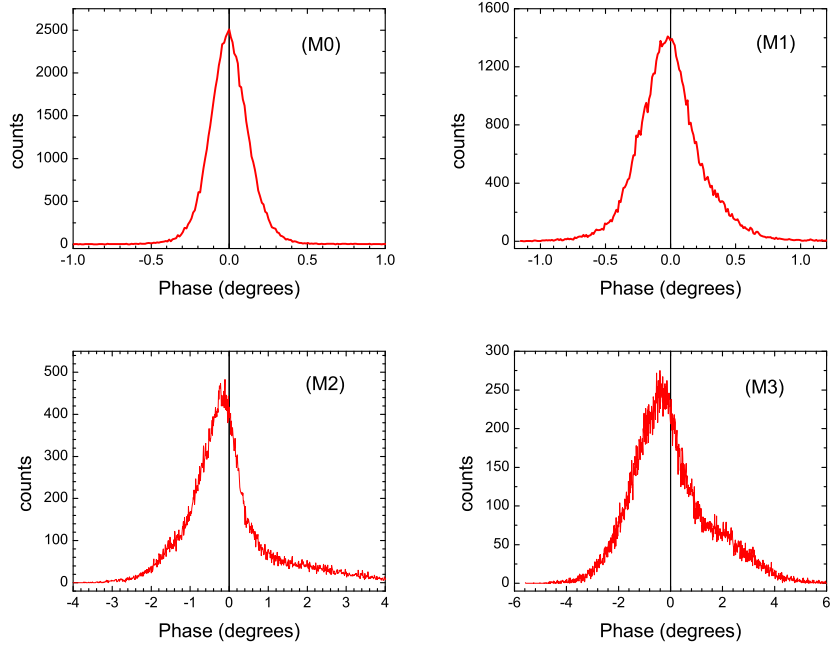


Figure 3.4: Distribution of counts obtained for phase shifts plotted in the images of figure 3.3 (M0), (M1), (M2) and (M3).

surface topography and the magnetic structure, which is discussed later. Eventually after 3 hours, almost entire sample surface gets crowded with these nuclei of the product ferromagnetic phase ((T3) and (M3)). No further changes were observed after waiting for longer times, which indicates the saturation of the relaxation process. It should be noted that for representing the $\mathcal{MF}\mathcal{M}$ data, the reference of the phase change is adjusted so as to make all the values positive. In reality, both the positive and negative values of phase change corresponding to the formation of newer nuclei are observed. Figure 3.4 makes this more clear.

Figure 3.4 shows the distribution of phase shift for all the $\mathcal{MF}\mathcal{M}$ images (M0 to M3). Each image has 256×256 points which thus gives the total number of counts. Phase shift distribution of image (M0) shows equal number of counts for positive and negative values making the distribution symmetric around zero. This is expected as the sample is supposed to be in the antiferromagnetic state when the image (M0) is obtained. As the evolution towards the ferromagnetic state takes place, the peak of distribution shifts slightly towards negative values. A net negative phase shift

indicates a repulsive interaction between the \mathcal{MFM} tip and the sample surface (see figure 2.12). The other aspect to be noted is that the width of the distribution has increased from a fraction of a degree in (M0) to a few degrees in (M3) (this can also be seen in the Z scale of the images of figure 3.3 as well). An increase in the width of distribution with a slight shift in the peak indicates that though newer nuclei of larger magnitudes are created, the net change in magnetization is quite less. Also, the smaller values of phase shift in figure 3.3 compared to those obtained in figure 3.2 indicate that the bulk is still in the antiferromagnetic state and the nucleation seen in figure 3.3 is probably only limited to the surface. The appearance of magnetic clusters with both positive and negative phase shift in the \mathcal{MFM} measurements clearly rules out the possibility that the features seen in \mathcal{MFM} measurements arise due to the sample-tip interaction. Otherwise, all the phase changes would have been of the same sign indicating either a completely attractive or repulsive interaction. Therefore, it can be inferred that the events imaged in figure 3.3 are intrinsic features of the sample and not any experimental artifact. The \mathcal{MFM} tip only acts as a sensor and not a trigger to the nucleation events.

The results presented in figure 3.3 show that a framework, which takes into account only static and isolated quenched-in disorder⁴ to explain phase coexistence across the transition could be quite insufficient. In case of quenched disorder, the density fluctuations in a coherence volume containing the defects create nucleation centres which give rise to phase coexistence over a length scale of a few nano-metres. The growth of individual nuclei is blocked due to the interface created between the nucleus and the parent matrix.⁴ If additional thermal fluctuations are also present which can overcome the interfacial energy barrier, each nucleus will grow to the extent where thermal fluctuations are balanced by the energy barrier. This can probably explain the growth of the location marked as ‘A’ in figure 3.3. However, this does not explain the formation of newer nuclei (figure 3.3 (T2) and (M2)) unless a mechanism

is present where the static impurities are correlated through a long range field. Disorder is intrinsic to any alloy system due to chemical inhomogeneity and lattice defects occurring over few atomic length scales. In case where a system undergoes structural transition, cooperative lattice distortions and the associated modification in the strain fields provide a natural way to couple the isolated pockets of disorder already present.⁵⁵ This scenario is seen in case of solid-solid transition in martensites which are mainly strain based systems.^{58,59} We now focus our attention back to figure 3.3 (T2). Newer nuclei in (T2) are formed at those places where the surface undulations were quite rapid in figure 3.3 (T0) and (T1). This indicates that variations in strain field could be responsible for correlating the nucleation centres present in the sample. A structural distortion taking place in one of the pockets of the sample produces a strain in the surrounding matrix through cooperative lattice distortion. This lattice distortion then couples to an adjacent impurity site and helps the other nucleus to overcome the interfacial energy barrier. This cooperative phenomenon leads to formation of textures of coexisting phases as can be seen in figure 3.3 (T2). The elastic and the magnetic degrees of freedom are coupled in Fe-Rh system¹⁶ and thus the lattice distortion (change in topography) is accompanied with a corresponding coexistence of the two competing magnetic phases (see figure 3.3 (M2)). This observation seems to follow the theoretical model proposed by Ahn et al.⁹ where the structural aspect is necessary to explain phase coexistence at micrometer scales. Modification in strain field will take place even if the magnetic transition occurs first and then leads to a structural distortion as seen in pump-probe experiments.^{22,23} It is possible that the scan area shown in figure 3.3 contains a grain boundary which influences the nucleation events in the regions 1, 2 and 3 of figure 3.3 (T2) and (M2). Even in that case the above discussion remains valid as a grain boundary is a discontinuity in the topography across which the variation in strain field will be very large.

The initial nucleation events which give rise to phase coexistence between the two

lattice and magnetic structures modify the original elastic and magnetic energy landscape decided by the temperature and field history of the sample. This modification can further produce numerous local minima in the energy landscape.⁹ The nucleation dynamics is then governed by this dynamical change of the landscape itself. This modification can lead to further nucleation of the product phase as seen in figure 3.3 (T3) and (M3) or can lead to a cooperative freezing of the transition in some cases.^{47,60} In either case the subsequent events are strongly dependent on the previous history of the free energy landscape. The sequence of events, in some sense, appear to be self-organized. It has been theoretically shown that micrometer scale phase coexistence is self organized and is caused due to an underlying elastic energy landscape.⁹ The structural aspect of the transition is necessary for the multi-scale phase coexistence to occur across a first order magneto-structural transition. Our results on the time evolution of the magneto-structural transition in Fe-Rh suggest that the predictions which were originally proposed for manganites with colossal magnetoresistance could also be extended to other systems which undergo a magneto-structural transition.

3.3 Summary

To summarize, we have directly imaged the time evolution of the initial stages of a first order magneto-structural transition occurring in Fe-Rh alloy. We observe coexistence of the antiferromagnetic and ferromagnetic phase over a sub-micrometer length scale. Nucleation and growth of the ferromagnetic phase out of the superheated antiferromagnetic matrix are observed. The correlation between the magnetic and the structural aspects of transition is distinctly visible. The dynamics of the transition process appears to be governed by coupling between electronic and elastic degrees of freedom, which leads to occurrence of phase-coexistence in micrometer scale. All these experimental observations further emphasize that the phase-coexistence and

metastability are general properties of a first order phase transition, and should be observed in various classes of materials undergoing magneto-structural transition irrespective of the origin of magnetic interaction. In the next few chapters, we shall use the understanding developed in this chapter to further probe the effects of phase coexistence and metastability on the functional properties of the Fe-Rh alloy system.

Publications based on this chapter

- 1) Imaging of time evolution of the first-order magneto-structural transition in Fe-Rh alloy using magnetic force microscopy
M. Manekar, C. Mukherjee and S. B. Roy
Europhys. Lett. [80, 17004](#) (2007).

Chapter 4

Nucleation and growth dynamics across first order phase transition in $\text{Fe}_{0.975}\text{Ni}_{0.025}\text{Rh}$

4.1 Introduction

In chapter 3, we saw the results of local imaging of the phase coexistence across the antiferromagnetic to ferromagnetic transition in the parent Fe-Rh alloy and how the phase transformation proceeded as a function of time. In this chapter, we present the results of bulk ac susceptibility and dc magnetization measurements on polycrystalline $\text{Fe}_{0.975}\text{Ni}_{0.025}\text{Rh}$. The sample undergoes a first order antiferromagnetic to ferromagnetic phase transition both as a function of temperature and magnetic field.²¹ It is known that addition of small amounts of Ni in the parent Fe-Rh alloy shifts the antiferromagnetic to ferromagnetic transition to lower temperatures and magnetic fields as compared to the parent alloy.²¹ This makes it possible to cover the entire transition regime within the upper temperature limit of our measuring instruments. Here, we try to find the common features between a general first order

transition driven by temperature and magnetic field and the time dependent crystallization of solids from sufficiently undercooled melts. Crystallization process or the nucleation and growth dynamics, in general, during transformations in solids has been a subject of great interest.^{61,62} The solidification and melting transitions are known to be of a first order nature and attempts have been carried out to establish the common features in such transitions with first order transitions in other systems. In this direction, it has been shown that the vortex lattice in a type-II superconductor melts like ice melting to water.⁶³ A lot of studies using local imaging at various length scales with different techniques have been carried out on diverse systems to study the transformation kinetics across first order transitions.^{47,50–54,56,57} While it is relatively straightforward to estimate the phase fractions of the coexisting phases using local imaging,⁶⁴ it is quite difficult to get a physical parameter from bulk measurements which can be related to the phase fraction. In situations where the local imaging or measurement of latent heat is difficult due to small values, hysteresis across the transition is used to determine the first order nature of the transition.² The presence of minor hysteresis loops (MHL) is usually taken as a signature of phase coexistence of both the phases across a first order transition.⁴³ However the correlation between the area of MHL and the phase fraction has only been intuitive.⁶⁵ In this chapter we attempt to correlate the area of MHLs with the phase fraction by studying the first order magnetic transition from the antiferromagnetic state to the ferromagnetic state in polycrystalline $\text{Fe}_{0.975}\text{Ni}_{0.025}\text{Rh}$ using bulk ac susceptibility and dc magnetization measurements. The well studied antiferromagnetic to ferromagnetic transition in Fe-Rh provides an interesting case study to understand the nucleation and growth dynamics across a first order magnetic transition. We first establish the generic features seen across a first order transition like phase coexistence and metastability for this antiferromagnetic to ferromagnetic transition. The phase coexistence is inferred by using the technique of MHLs and the presence of metastable states is confirmed

through time dependent magnetization measurements across this first order transition. The results of these relaxation measurements are used to draw analogy between the dynamics of this first order transition with the generalized model of crystallization of solids. The inferred phase fraction from the areas of MHLs appears to follow the well known Avrami law for phase transformation in solids.⁶⁶

4.2 Phase coexistence and metastability

Figure 4.1 shows the ac susceptibility as a function of temperature both during heating and cooling of the sample. A sharp rise in susceptibility slightly above 260 K during heating indicates the onset of the antiferromagnetic to ferromagnetic transition. During cooling, the onset of the ferromagnetic to antiferromagnetic transition takes place at a temperature slightly below 320 K and the temperature dependent susceptibility shows a hysteresis across the transition. Hysteresis across the antiferromagnetic to ferromagnetic transition in Ni doped Fe-Rh alloys has been earlier observed in electrical transport measurements.²¹ Those results along with the present ac susceptibility results confirm the first order nature of the transition. As mentioned in our earlier reports on ac susceptibility measurements on other systems using the same apparatus,^{43,44} we have swept the temperature unidirectionally instead of stabilizing at each measurement point. This was done to avoid any thermal oscillation around the temperature set-point which is typical of any PID controller. Reversing the direction of temperature change before reaching the reversible region results in a minor loop. A minor loop which exhibits finite hysteresis is an indication of the coexistence of the two competing phases involved in the transition.^{43,67} Thus a MHL initiated on the heating cycle indicates the coexistence of the growing product ferromagnetic phase within the parent antiferromagnetic matrix. Similarly the MHLs initiated on the cooling cycle indicate the coexistence of the product antiferromag-

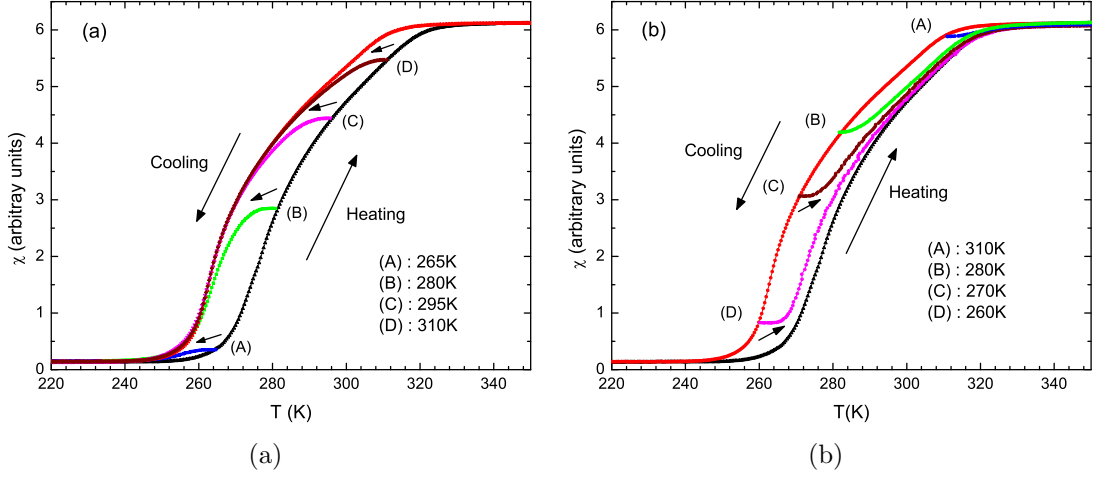


Figure 4.1: Ac susceptibility as a function of temperature across the first order transition in $\text{Fe}_{0.975}\text{Ni}_{0.025}\text{Rh}$. (a) Minor hysteresis loops initiated on the heating cycle and (b) Minor hysteresis loops initiated on the cooling cycle. The temperatures of initiation of the minor loops in both the cases are marked as A, B, C and D.

netic phase within the parent ferromagnetic matrix. Figure 4.1(a) and figure 4.1(b) show a few representative MHLs initiated both on the heating and the cooling cycle respectively. It can be seen that the area of MHLs increases while the sample transforms from one phase to another. We shall relate the area of the MHLs with the growth of the product phase in the following discussion.

Having established the presence of hysteresis and phase coexistence across the transition, we focus on another signature of a first order transition which is the existence of metastable states. The signature of metastable states can be experimentally observed by measuring the time dependence of a physical quantity intrinsic to the sample which is relevant to the phase transition. In this case, we measure the time dependence of magnetization at various temperatures in a fixed field of 10 mT using the VSM.

Figure 4.2(a) shows normalized magnetization as a function of time at 295 K on the heating cycle. The sample was heated unidirectionally up to 295 K from a temperature well below those values where the magnetization is reversible. The magnetization was then measured as a function of time immediately after the temperature was stabilized.

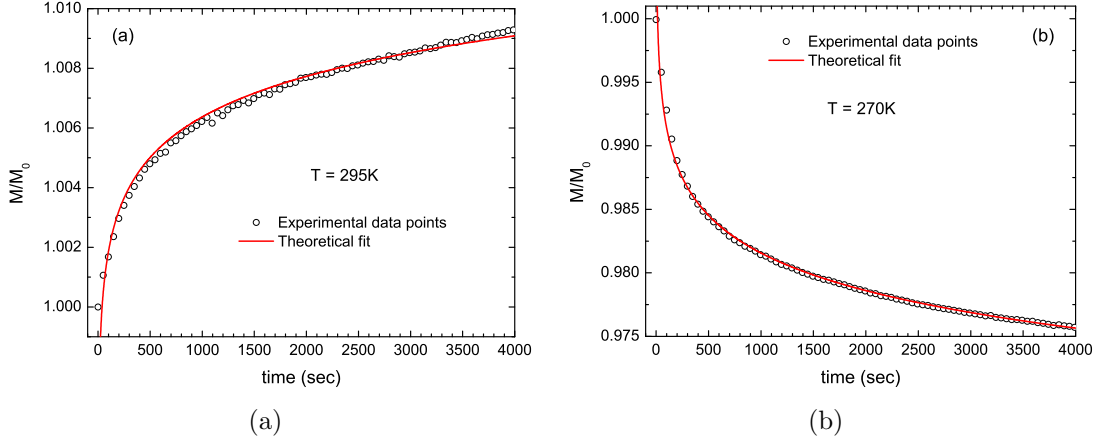


Figure 4.2: Time dependent magnetization of $\text{Fe}_{0.975}\text{Ni}_{0.025}\text{Rh}$ during the temperature driven transition at representative temperatures on (a) the temperature increasing cycle and (b) the temperature decreasing cycle. Solid line shows the calculated curve from equation 4.1.

The normalization of magnetization is carried out with respect to the magnetization value at the first measurement point after reaching this temperature (i.e. at $t = 0$). The magnetization relaxes towards a higher value, which clearly indicates the presence of metastable (superheated) antiferromagnetic phase relaxing towards the stable ferromagnetic phase. The time dependent magnetization does not follow the usual exponential law but can be very well fitted with the following equation:

$$M/M_0 = -1 + 2t^\gamma, \quad (4.1)$$

where M_0 is the value of magnetization at $t = 0$. The value of γ indicates the extent of relaxation, i.e. a higher value of γ means a greater degree of relaxation for the same time interval. This equation has been shown to apply for the relaxation of ferromagnetic dots which interact through long-range dipolar interaction.⁶⁸ A similar situation could arise for the case of an antiferromagnetic to ferromagnetic transition when the nucleation is heterogeneous. The clusters of the ferromagnetic phase nucleate in the antiferromagnetic matrix and these ferromagnetic clusters can interact through a long-range dipolar interaction. In chapter 3 we have discussed the results of local imaging of the antiferromagnetic to ferromagnetic transition on a sub-micron

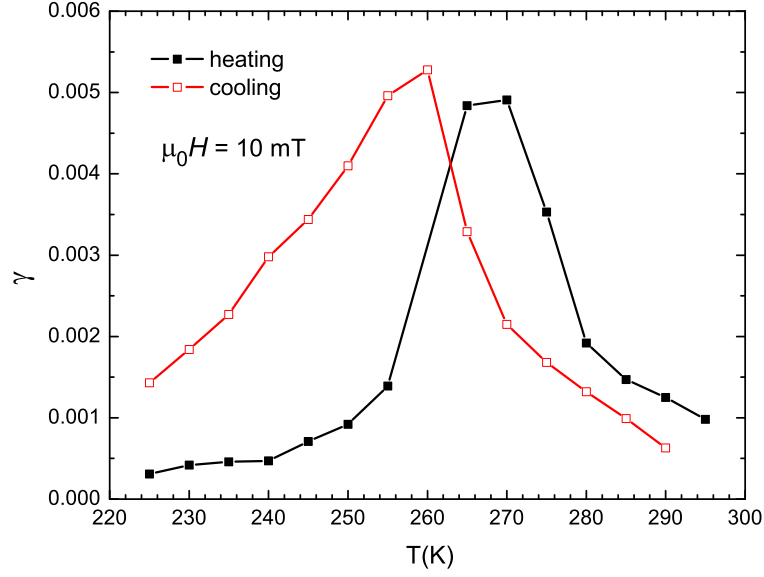


Figure 4.3: Temperature dependence of the exponent γ in equation 4.1 during the temperature driven transition in $\text{Fe}_{0.975}\text{Ni}_{0.025}\text{Rh}$. The absolute value of γ is plotted for the cooling cycle for the sake of comparison on the same scale.

scale in Fe-Rh alloy using magnetic force microscopy. There we have indeed shown the nucleation of the ferromagnetic phase in the antiferromagnetic matrix. We believe that the nucleated ferromagnetic clusters in this sample interact through long-range forces.

Similar measurements of the time dependence of magnetization were performed on the cooling cycle as well. Figure 4.2(b) shows the normalized magnetization as a function of time at 270K on the cooling cycle. Once again the relaxation can be described with the power law expressed in equation 4.1 with the value of γ being negative. To get the temperature dependence of γ , relaxation measurements were performed at various temperatures both during the heating and cooling cycle. For measuring the relaxation during the heating(cooling) cycle, the temperature was increased(decreased) unidirectionally until the target value starting from that temperature where the magnetization is reversible.

Figure 4.3 shows the variation of the exponent γ in equation 4.1 as a function of temperature. While the value of γ is directly taken for the heating cycle, the

magnitude of γ is plotted for the cooling cycle. During the heating cycle, the value of the exponent shows an initial increase with rise in temperature and then drops with further rise in temperature. This probably indicates that the initial part of the transition while heating is dominated by the creation of newer ferromagnetic nuclei (giving rise to more relaxation) and at later stages these nuclei merge to grow into the product ferromagnetic phase. The peak in the temperature dependence of γ thus indicates the cross-over from nucleation to growth of the product phase. The same discussion applies for the temperature dependence of γ while cooling. The initial part of the cooling cycle appears to be dominated by the creation of newer antiferromagnetic nuclei (resulting in more rapid fall of magnetization) and later these antiferromagnetic nuclei coalesce to form the low-temperature antiferromagnetic phase.

4.3 Avrami model of nucleation and growth

The results of figure 4.3 indicate a nucleation and growth mechanism quite similar to that of crystallization of solids described in the Avrami model.⁶⁶ The central assumption of the Avrami model are as follows

- The new phase is nucleated by *germ nuclei* which already exist in the parent matrix.
- The density of these germ nuclei diminishes through activation of some of these into growth nuclei and the coalescence of these nuclei in to the product phase.
- The growth rate is independent of the transformed phase and only depends on the *untransformed* phase
- The nucleation events are considered to be random and the nuclei are allowed to freely overlap with each other during the growth process.

The schematic of this process is shown in figure 4.4.

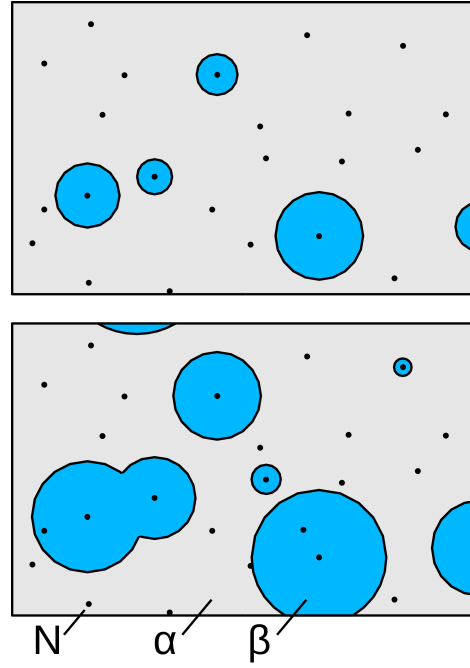


Figure 4.4: Schematic of the nucleation and growth process in the Avrami model. N is the number of nuclei, α is the parent phase and β is the product phase.

4.3.1 Isothermal case

The transformation of the parent α phase in to product β phase proceeds by the nucleation of new particles at a rate \dot{N} per unit volume which grow at a rate \dot{G} into spherical particles and only stop growing when they meet each other. During a time interval, $0 < \tau < t$, nucleation and growth can only take place in *untransformed* material. During the time interval τ to $\tau + d\tau$ the number of nuclei, N , that appear in a sample of volume V will be given by:⁶⁶

$$N = V \dot{N} d\tau. \quad (4.2)$$

With the assumption of an isotropic growth with a constant growth rate \dot{G} , which is not hindered by the previous growth, each nucleus will grow into a sphere of radius $\dot{G}(t - \tau)$. Thus the volume of the product phase will be:

$$dV_\beta^e = \frac{4\pi}{3} \dot{G}^3 (t - \tau)^3 V \dot{N} d\tau. \quad (4.3)$$

The superscript ‘ e ’ in the above equation is to indicate that the transformed volume is actually an extended (or overestimated) volume of the β phase as the spheres of the product phase are allowed to overlap freely (see figure 4.4). The integration of equation 4.3 between $\tau = 0$ to $\tau = t$ will yield the total extended volume:

$$V_{\beta}^e = \frac{\pi}{3} V \dot{N} \dot{G}^3 t^4. \quad (4.4)$$

Only a fraction of this extended volume is real and the overlapping region is virtual. Since it is assumed that the nucleation is random (i.e. independent of the other nucleation or growth events and having no preference), the fraction of the extended volume that is real is proportional to the untransformed phase α . Thus,

$$dV_{\beta} = dV_{\beta}^e \left(\frac{V - V_{\beta}}{V} \right). \quad (4.5)$$

Upon integrating the above equation we get

$$\ln(1 - f) = -\frac{V_{\beta}^e}{V}, \quad (4.6)$$

where f is the transformed phase fraction, or volume fraction of the product phase β . The same equation can be rearranged in the more familiar form:

$$f = 1 - \exp(-Kt^{\eta}), \quad (4.7)$$

where K is $\pi \dot{N} \dot{G}^3 / 3$ and η is 4 as can be seen from equation 4.4. This relation is popularly known as the Kolmogorov-Johnson-Mehl-Avrami (KJMA) relation. Here K is related to the activation energy and η is known as the Avrami exponent which depends on the geometrical factors.⁶⁶ The model was originally proposed for time dependent isothermal cases where the melt (liquid phase) has been sufficiently un-

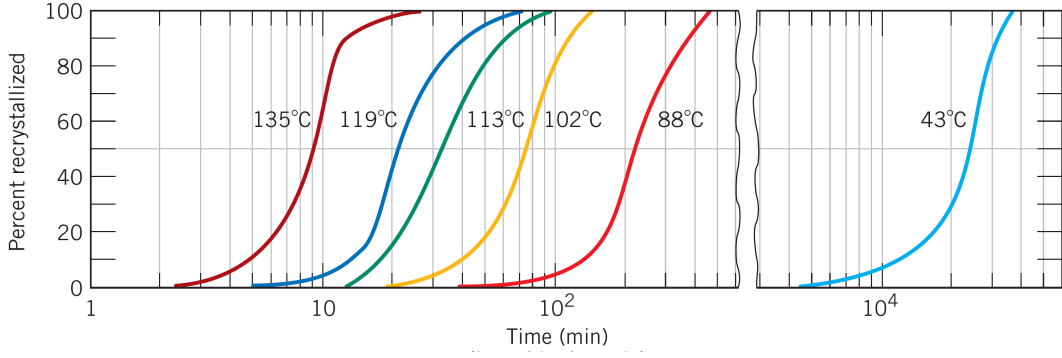


Figure 4.5: Percent recrystallization (phase fraction) as a function of time at constant temperatures during solidification of pure copper from melt. Reproduced from ref. [69].

dercooled to enable crystallization of the solid phase. Equation 4.7 gives the famous S -shaped curve when the phase fraction of the crystallized phase is plotted as a function of time.^{69,70} One such example for the case of crystallization of pure copper is shown in figure 4.5.

4.3.2 Temperature driven transition

If we extend this analogy for temperature driven first order magnetic transitions with the same assumption of nucleation and growth process, we should be able to (intuitively) see a similar relation of the temperature dependence of the phase fraction of the product phase. From the results of local imaging presented for field-induced transitions in case of Gd_5Ge_4 ⁵² and CeFe_2 based alloy system,⁵¹ the nucleation and growth process appears to closely follow the assumptions of the Avrami model. We believe that similar nucleation and growth process takes place across the first order transition in case of our alloy system under consideration.

For temperature driven transitions, a general constitutive framework can be formulated if the phase fraction f of the transformed phase is governed by a differential equation of the type:⁷¹

$$\frac{df}{dt} = F\left(f, T, \frac{dT}{dt}, \dots, \frac{d^n T}{dt^n}\right). \quad (4.8)$$

Here F is some function of phase fraction, temperature and the rate of change of temperature. In the first approximation, if the transformation rate depends only on the first order rate of change of temperature, this equation can be specialized to

$$\frac{df}{dt} = H(f, T) \frac{dT}{dt}, \quad (4.9)$$

where H is a function of only f and T . The variables can be separated if we look in to the third assumption of the Avrami model, which states that the rate of transformation depends only on the *untransformed* phase fraction. Equation 4.9 can be rewritten as:⁷¹

$$\frac{df}{dt} = (1 - f)\zeta(T) \frac{dT}{dt}. \quad (4.10)$$

The temperature dependence of the phase fraction can be calculated by integrating the above equation. This yields:

$$f = 1 - \exp\left(-\int \zeta(T) dT\right). \quad (4.11)$$

Under certain special circumstances the above equation will be reduced to

$$f = 1 - \exp(-k(T - T_0)^\eta), \quad (4.12)$$

where T_0 is the onset temperature of the transformation. This equation is very similar to equation 4.7 with time replaced by temperature. A more rigorous derivation of the non-isothermal KJMA equation requires the input from thermodynamical measurements like the differential scanning calorimetry to know the activation energy which decides the growth rate and the function $\zeta(T)$.^{72,73} However, the final result matches quite well with simple relation given in equation 4.12. The evolution of the phase fraction with temperature also follows the *S*-shaped curve as in equation 4.7.⁷⁴ The

validity of this change of variables for our case needs to be verified now by identifying the phase fraction across the first order transition in bulk measurements.

4.4 Identification of phase fraction

The central issue now is to identify a proper parameter from bulk magnetization measurements which can be related with the phase fraction of the respective phases. The value of magnetization or susceptibility at a particular temperature cannot be directly taken as a measure of phase fraction because the nucleation of the ferromagnetic phase is random, which leads to the magnetization of ferromagnetic clusters to align in random directions. The measured bulk magnetization is the vector sum of all these magnetic moments and thus will give an entirely different value of phase fraction. In the earlier chapter which discussed the results of imaging of magneto-structural transition using \mathcal{MFM} , we have explicitly shown that the alignment of all the newly formed ferromagnetic clusters during the transition is not along the same direction. Also the time dependent magnetization data presented in figure 4.2 follow an entirely different equation compared to the Avrami model in equation 4.7. This strongly indicates that bulk magnetization cannot be taken as a measure of phase fraction directly.

We propose that the area of MHLs can be a convenient parameter which is related to the phase fraction. Our heuristic argument is as follows. The envelope curve is the hysteresis curve which encloses both the reversible low-temperature and high-temperature phases. During the heating cycle of the envelope curve, the entire sample transforms from the antiferromagnetic to ferromagnetic phase. Similarly, the cooling curve represents the entire sample transforming from the ferromagnetic to antiferromagnetic phase. If a minor loop is initiated at any intermediate temperature value, it exhibits a smaller hysteresis compared to the hysteresis obtained on the complete

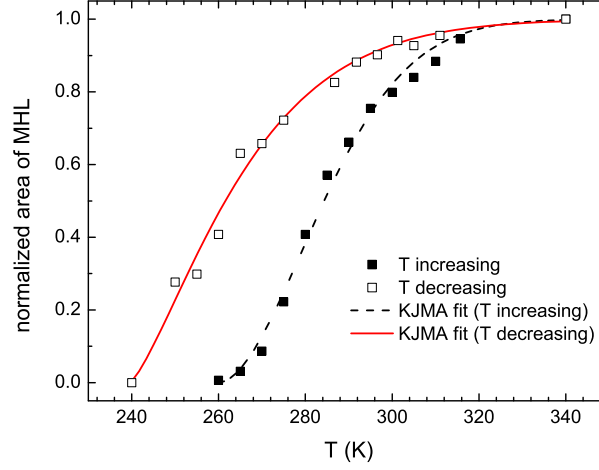


Figure 4.6: Temperature dependence of the areas of MHLs inferred from the ac susceptibility measurements shown in figure 4.1. The areas of MHLs are related to the phase fraction of the ferromagnetic phase. See text for details for the estimation of phase fraction during both the heating and cooling cycles. The dashed line shows the theoretical curve for the heating cycle following equation 4.12. Similarly, the solid line indicates the theoretical curve using the same equation for the cooling cycle.

envelope curve. A minor loop shows hysteresis when both the phases involved in the transition coexist. The MHL ‘A’ of figure 4.1(a) encloses a smaller area compared to MHL ‘B’ as the amount of the ferromagnetic phase at lower temperatures is lower during the heating cycle. Thus growing ferromagnetic fraction is also accompanied with the growing area of MHL. If we (hypothetically) divide the entire sample into smaller volumes, each hysteresis loop (envelope curve or MHL) can be thought of as a superimposition of smaller hysteresis loops for each of these volumes. Thus the area of a hysteresis loop initiated at any temperature, which is an addition of smaller hysteresis loops, would represent the volume of the transformed phase at that temperature. If we take the area of envelope curve as unity, the area of each MHL divided by the area of the envelope curve can then be taken as the phase fraction of the product phase at the temperature of initiation of MHL. A similar situation has been dealt with in the case of hysteresis loops of ferromagnets where the minor loop area is related to the volume fraction.⁷⁵ However, in absence of any theoretical framework for deducing the phase fraction from bulk measurements, our assumption here is more simplified and we take the normalized area of MHL directly as the phase

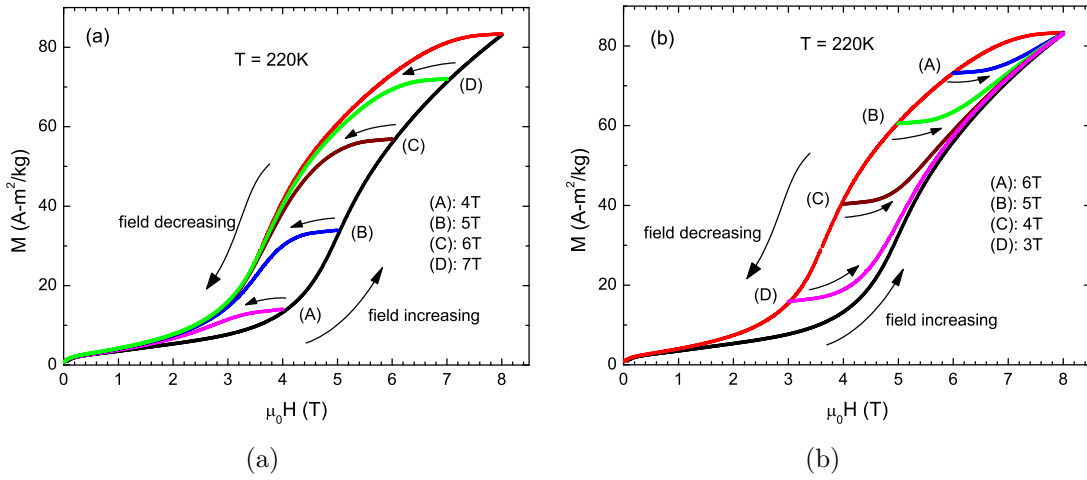


Figure 4.7: Isothermal magnetization of $\text{Fe}_{0.975}\text{Ni}_{0.025}\text{Rh}$ as a function of magnetic field. Minor hysteresis loops (a) on the field increasing cycle and (b) on the field decreasing cycle. The field values of initiation of minor loops are marked as ‘A’, ‘B’, ‘C’ and ‘D’.

fraction.

The increasing area of MHL during cooling represents the increasing phase fraction of the antiferromagnetic phase. However, for simplicity, we shall always discuss in terms of the increase and decrease of the fraction of the ferromagnetic phase. So unity minus the normalized area of MHL during the cooling cycle represents the decrease of the ferromagnetic fraction and thus can be plotted on the same scale as that of the growing ferromagnetic fraction.

Figure 4.6 shows the phase fraction of the ferromagnetic phase as a function of temperature both while heating and cooling the sample. The temperature dependent phase fraction very closely resembles the famous ‘S’-shaped transformation-time curve which is predicted by the Avrami model.⁶⁶ The shape of the curve enables us to fit the phase fraction with an equation very similar to the KJMA equation by replacing time with temperature (equation 4.12). The values of T_0 and η on the heating cycle are 260 K and 1.837 respectively. Similarly on the cooling cycle, the values of T_0 and η are 239.6 K and 1.324 respectively. As can be clearly seen, the experimental data can be very well described with this law. This close similarity indicates that the growth kinetics across a first order transition follow some kind of a universal behaviour

irrespective of the detailed nature of the phases involved. Similar to our observation, it has been shown that the extended Avrami model can also be applied for describing the volume fraction of the reversed domains in ferroelectrics subjected to oscillating electric fields.⁷⁶ The nucleation and growth kinetics across the temperature driven first order antiferromagnetic to ferromagnetic transition in $\text{Fe}_{50}(\text{Rh}_{1-x}\text{Pt}_x)_{50}$ thin films were analyzed using the KJMA model.⁷⁷ However, the authors have directly taken the value of bulk magnetization as a measure of phase fraction, which is incorrect as we have discussed before.

Similar arguments can be carried out for the field induced (metamagnetic) transition. Figure 4.7 shows the isothermal magnetization at 220 K. This temperature value was chosen so that the entire sample is definitely a single phase antiferromagnet. A sharp rise in magnetization at about 4T on the field increasing curve marks the onset of the antiferromagnetic to ferromagnetic transition. The transition is not complete till 8 T which is quite close to the upper limit of magnetic field in our VSM. On decreasing the field, we see a hysteresis across the transition similar to the temperature dependent ac susceptibility measurement. This indicates that the metamagnetic transition is also of the first order nature. The presence of phase coexistence across the metamagnetic transition can be seen by generating MHLs on the field-increasing and field-decreasing cycles. Figure 4.7(a) shows a few representative MHLs initiated on the field-increasing cycle. Similarly, figure 4.7(b) shows MHLs initiated on the field-decreasing cycle.

Similar to the relaxation measurements in constant field which are shown in figure 4.2, isothermal time dependent magnetization measurements clearly show the presence of metastable states across the metamagnetic transition (see figure 4.8). Figure 4.8(a) shows time dependent magnetization during the field-increasing cycle, whereas figure 4.8(b) shows relaxation during the field-decreasing cycle. Like the constant-field relaxation shown in figure 4.2, the isothermal relaxation at various fields also

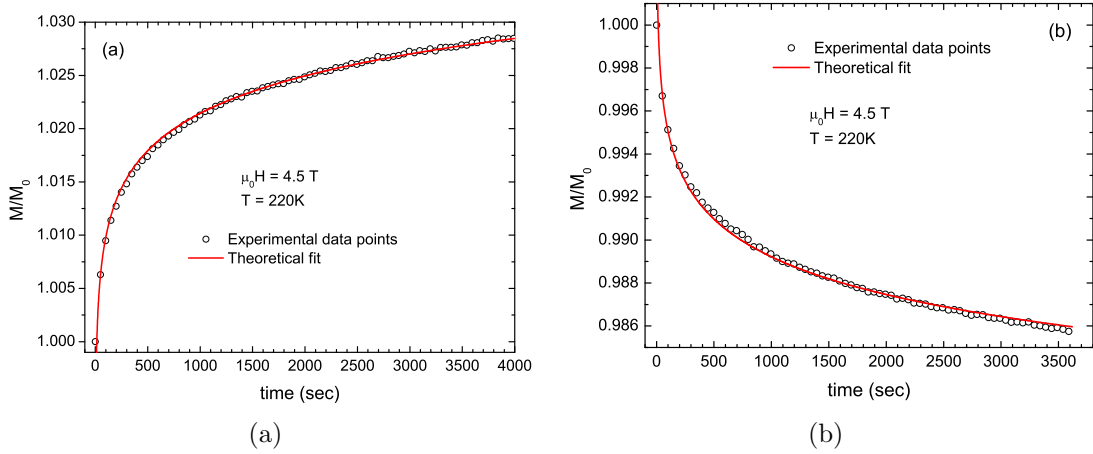


Figure 4.8: Time dependent magnetization of $\text{Fe}_{0.975}\text{Ni}_{0.025}\text{Rh}$ during the field induced transition at representative fields on (a) the field increasing cycle and (b) the field decreasing cycle. The solid line indicates the calculated curve using equation 4.1.

obeys the same law expressed in equation 4.1.

The value of exponent at various fields during both the field increasing and decreasing cycle is shown in figure 4.9. The same behaviour of the exponent is again seen here across the field induced transition. This shows that the transition kinetics appear to be the same for both the temperature and field induced transitions.

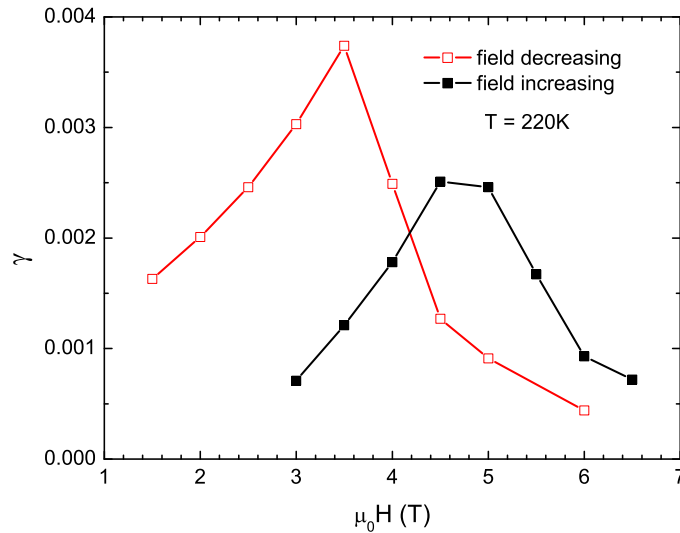


Figure 4.9: Field dependence of the exponent γ in equation 4.1 during the field-induced transition. The absolute value of γ is plotted for the field-decreasing cycle for the sake of comparison on the same scale.

Figure 4.10 shows the areas of MHLs during the metamagnetic transition along with the theoretical fit given by the equation:

$$f = 1 - \exp(-k(H - H_0)^\eta), \quad (4.13)$$

where H_0 is the onset magnetic field of the transition.

This is just equation 4.12 rewritten by replacing temperature with magnetic field. The phase fraction again closely follows the Avrami law as can be seen from figure 4.10. Here the values of H_0 and η are 3 T and 2.284 respectively on the field-increasing cycle. The values of H_0 and η are 1.28 T and 2.198 respectively on the field-decreasing cycle. The difference in the values of η for the temperature-driven transition (see equation 4.12) and the field-driven transition probably arises because the dependence of the activation energy on the magnetic field and temperature are not explicitly included in the above equations. Further work is needed to establish a generalized function similar to the case of electric field driven reversal of domains in ferroelectrics.⁷⁶ The areas of MHLs are represented in arbitrary units as we do not have the complete envelope curve whose area can be taken for normalization.

We thus see that the temperature and field driven transitions both follow similar kinetics and have a very close resemblance to that of phase transformation during solidification process. We hope our experimental results will provide a path for future work for identifying the phase fraction from bulk measurements and also to explain the transformation kinetics in a generalized manner. More experimental and theoretical work is required on various systems undergoing a first order phase transition before a generalized framework is established.

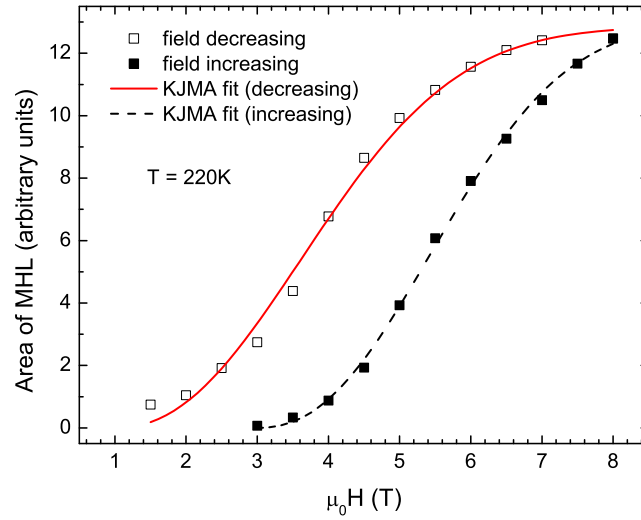


Figure 4.10: Field dependence of areas of MHLs inferred from the isothermal magnetization measurements shown in figure 4.7, which is related to the phase fraction of the ferromagnetic phase. See text for details for the estimation of phase fraction during both the field-increasing and field-decreasing cycles. The dashed line shows the theoretical curve for the field-increasing cycle following equation 4.13. Similarly, the solid line indicates the theoretical curve using the same equation for the field-decreasing cycle.

4.5 Summary

In this chapter we have seen the results of the bulk ac susceptibility and dc magnetization across the antiferromagnetic to ferromagnetic transition in $(\text{Fe}_{0.975}\text{Ni}_{0.025})_{50}\text{Rh}_{50}$. The time dependent magnetization both during the temperature and field driven transitions follows a power law which is thought to arise from the long-range dipolar interaction between the ferromagnetic clusters. The exponent of the power law equation shows a non-monotonic behaviour in both the temperature and field induced transitions. This non-monotonic behaviour points towards a nucleation and growth behaviour very similar to the Avrami model of crystallization of solids. The areas of the minor hysteresis loops across the transition can be related to the phase fraction of the product phase involved in a first order transition. The evolution of these areas follow the law explained by the Avrami model which is extended by replacing time with temperature and magnetic field. Further theoretical work is now required which can relate the parameters from bulk magnetization measurements to the phase fraction

across a first order magnetic transition. In the next chapter we see if the assumption behind identification of phase fraction, that different locations of the sample which undergo transition have their own hysteresis, holds true or not. Specifically we study the response of the sample undergoing multiple temperature cycling inside the hysteretic region across the first order transition and model its thermal response within the assumption of independent hysteresis loops.

Publications based on this chapter

- 1) Nucleation and growth dynamics across the antiferromagnetic to ferromagnetic transition in $(\text{Fe}_{0.975}\text{Ni}_{0.025})_{50}\text{Rh}_{50}$: analogy with crystallization

M. Manekar and S. B. Roy

J. Phys.: Condens. Matter **20**, 325208 (2008).

Chapter 5

Modeling of minor hysteresis loops in $\text{Fe}_{0.955}\text{Ni}_{0.045}\text{Rh}$

5.1 Introduction

In chapter 4, we discussed the nucleation and growth dynamics across the antiferromagnetic to ferromagnetic transition and showed the analogy with the crystallization process. The identification of the phase fraction of the transformed phase from bulk measurements was based on the assumption that different locations of the sample have their own independent hystereses. In this chapter we further explore the assumption of independent hysteresis loops by studying the results of temperature dependent strain measurements across the first order antiferromagnetic to ferromagnetic phase transition in $\text{Fe}_{0.955}\text{Ni}_{0.045}\text{Rh}$. We observe a distinct thermal hysteresis in the measured strain across the phase transition. The minor hysteresis loops inside the hysteretic regime across the temperature driven transition are modeled using the Preisach model of hysteresis.⁷⁸ The Preisach model is based upon the assumption of adding independent hysteresis loops with a suitable weight factor to explain the entire hysteresis curve. The applicability of the Preisach model to explain the general

features of minor hysteresis loops presented here is discussed for a disorder influenced first order transition. Specifically we observe that the minor hysteresis loops show the property of retaining the memory of the starting or end point of the temperature cycle followed within the hysteretic region. A larger temperature excursion within the hysteretic region wipes out the memory of a smaller temperature cycle which contains one of the end points of the larger cycle. The end point memory and the wiping out property of the minor hysteresis loops can be described quite well within the Preisach model, irrespective of the temperature history followed to reach a particular starting point. Our results show that the understanding of physical processes taking place across a first order transition is important if the functional response of the material is to be predicted under multiple cycling of the external driving parameter.

5.2 Hysteresis and phase coexistence

Figure 5.1 shows the linear strain in $\text{Fe}_{0.955}\text{Ni}_{0.045}\text{Rh}$ alloy as a function of temperature in the temperature range from 150 K to 300 K. The strain $\varepsilon(T)$ is calculated with respect to the length at 293 K and is defined as $\Delta L(T)/L(293\text{K})$, where $\Delta L(T) = L(T) - L(293\text{K})$, with $L(T)$ being the length at any temperature T . A sudden increase in strain during the heating cycle just near 200 K marks the onset of the antiferromagnetic to ferromagnetic first order magneto-structural transition. On decreasing the temperature, the onset of the ferromagnetic to antiferromagnetic transition takes place at slightly above 235 K and the transition completes just below 175 K. The characteristic temperatures related to the transition are $(\text{FM})_s \approx 200\text{ K}$, $(\text{FM})_f \approx 275\text{ K}$, $(\text{AFM})_s \approx 235\text{ K}$ and $(\text{AFM})_f \approx 175\text{ K}$, where the subscripts ‘s’ and ‘f’ denote the start and finish temperatures respectively. $(\text{FM})_f$ is actually the limit of superheating (T^{**}) and $(\text{AFM})_f$ is the limit of supercooling (T^*) for the bulk sample.⁷ A linear strain of almost 0.4% is observed between the two reversible ends of the

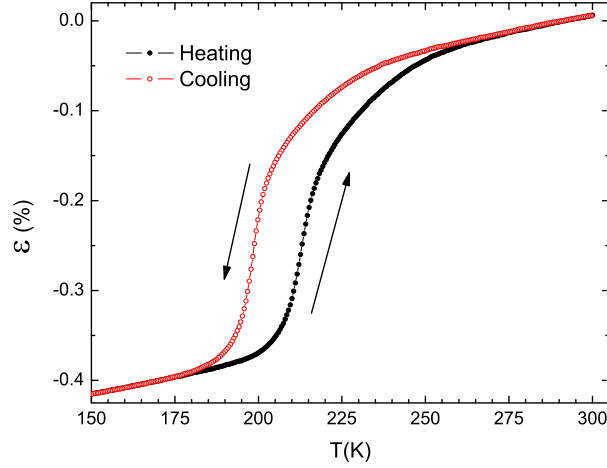


Figure 5.1: Linear strain as a function of temperature in the $\text{Fe}_{0.955}\text{Ni}_{0.045}\text{Rh}$ alloy during the heating and cooling cycles. See text for the definition of strain.

transition in our polycrystalline sample, which is consistent with the reported volume change of nearly 1% across the transition measured by x-ray diffraction.¹⁶

The important aspect to be noticed about the hysteresis curve is related to the onset temperatures of the transition while heating and cooling. The onset temperature during the cooling cycle ($(\text{AFM})_s \approx 235 \text{ K}$) is larger than that during the heating cycle ($(\text{FM})_s \approx 200 \text{ K}$), which indicates that the transition is influenced by disorder, as we have discussed in chapter 1.¹⁰ Furthermore, strain produced in the sample matrix during a structural transition can couple these isolated defects and lead to the formation of a *landscape* of free-energy minima.⁹ We have discussed the results of local imaging of such correlation of the elastic and electronic (magnetic) degrees of freedom across the FOMST in the parent Fe-Rh alloy in chapter 3. This free-energy landscape can thus manifest as a broad transition when observed in bulk samples with global measurements, but on a local scale (smaller pockets) the sample undergoes a relatively sharp transition at different temperatures or different values of the external driving force related to the transition. This behaviour has been seen in doped CeFe_2 based alloy⁵¹, Ni-Mn-In alloy⁵³ and Gd_5Ge_4 .⁵² The landscape model was shown to be applicable in case of our parent sample Fe-Rh through direct imaging of the phase coexistence (see chapter 3) and thus could be the cause behind the broad transition

in the present sample under consideration. A similar landscape of transition fields in the case of melting transition in vortex matter in a high- T_C superconductor has been explicitly imaged.⁶⁴ A smeared out transition with the presence of supercooling and superheating can result in a hysteresis curve as seen in figure 5.2 which has the relation between the onset temperatures as mentioned above.¹⁰

As discussed in chapter 4, such broad first order transitions usually proceed through the nucleation and growth of the product phase out of the parent matrix. The hysteretic temperature region thus consists of a phase-coexistence regime where the parent and product phase coexist together. We use the technique of minor hysteresis loops (MHL)⁴³ to establish the presence of phase coexistence across the hysteretic region. We term the $\varepsilon(T)$ curve which encloses the hysteretic region as the envelope curve (see figure 5.1). This envelope curve consists of the heating curve generated from below T^* till T^{**} and the cooling curve started from above the T^{**} till below T^* . A minor loop is formed when the direction of temperature change during the experiment is reversed before reaching the thermally reversible region. The MHLs as well as the envelope curves are generated by varying the temperature in a strictly unidirectional manner. Typically, the temperature is ramped at a rate of 0.6K/min.

We show some of the representative MHLs in figure 5.2 which are initiated both on the heating and cooling cycle. The minor loops showing hysteresis is an indication of the coexistence of the competing phases at the temperature of initiation of the loop.⁴³ The concept of the landscape of free energy minima discussed in the earlier chapters will be useful when we attempt to model these MHLs generated during multiple cycling of temperature.

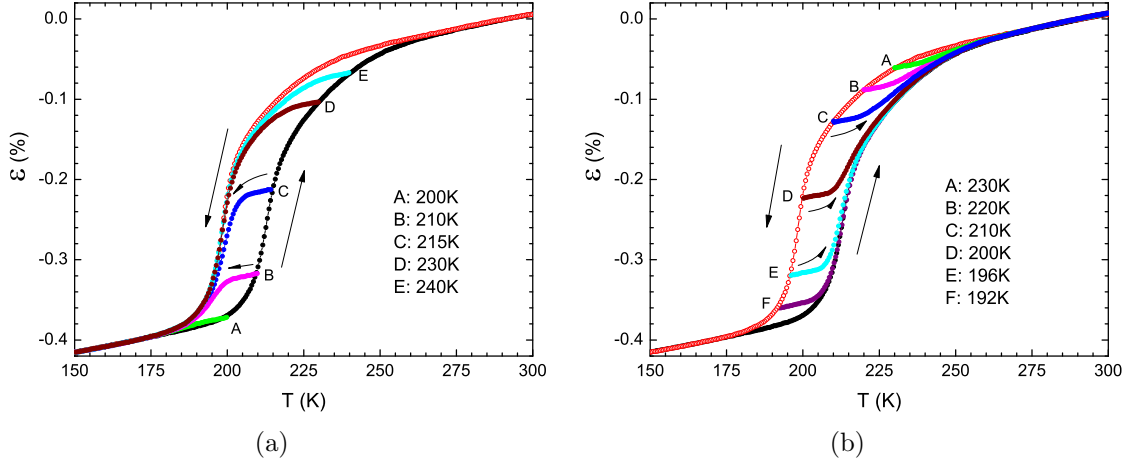


Figure 5.2: Minor hysteresis loops in $\text{Fe}_{0.955}\text{Ni}_{0.045}\text{Rh}$ initiated on (a) heating cycle and (b) the cooling cycle. The temperatures of initiation of the minor loops are denoted as alphabets.

5.3 General features of minor hysteresis loops

The presence of hysteresis and phase coexistence (resulting in MHLs) across the transition means that the value of the measured physical property not only depends on the value of the driving force (temperature, in this case) but also on the history of reaching to a particular value of the control parameter. The output is then a multivalued function of the input. This fact is of significant importance if the physical property (presently, strain) is to be used for technological applications where the device undergoes numerous cycling of the driving force. Specifically, if the material is cycled to and fro inside the hysteretic regime, it becomes necessary to be able to predict the entire path of evolution of the output if a successful device is to be constructed. Such a situation may arise if the entire available range of the strain across the transition (0.4% in our case) is not required for the desired application.

To understand the response of the material exposed to multiple temperature cycling, we first note down some of the universal features of the MHLs. Figure 5.3(a) shows the result of multiple cycling of temperature inside the hysteretic regime across the first order transition in our sample. This particular MHL is initiated on the envelope cooling curve. The temperature is decreased unidirectionally on the envelope

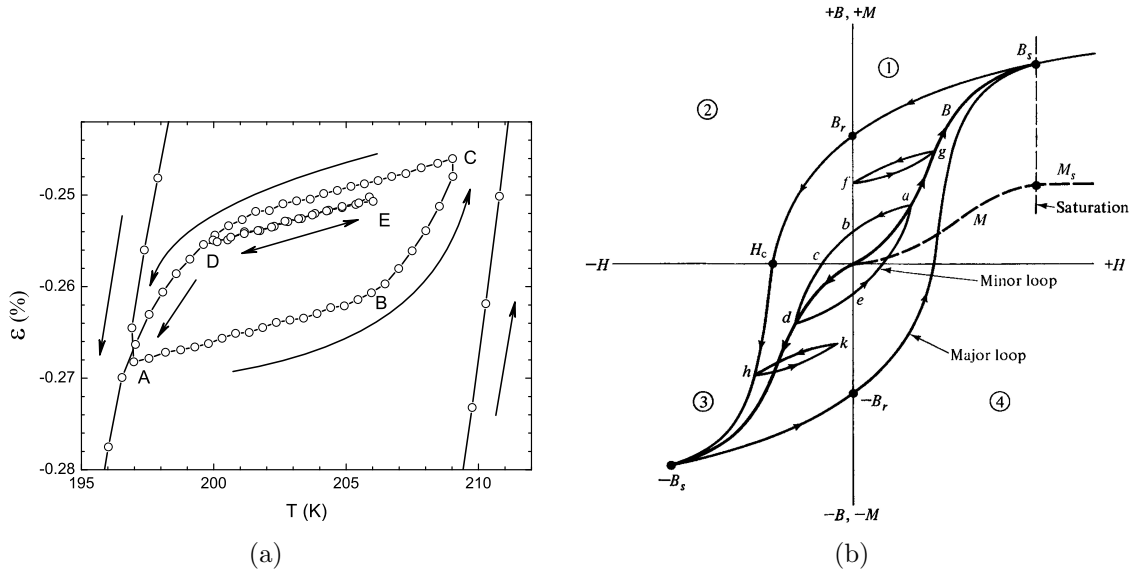


Figure 5.3: (a) Minor hysteresis loop during the temperature driven transition in $\text{Fe}_{0.955}\text{Ni}_{0.045}\text{Rh}$, which shows the property of retaining the end point memory and also the wiping out of the memory of a smaller temperature excursion inside a minor hysteresis loop. Note that the hysteresis is confined to the first quadrant only. (b) The $B-H$ (or $M-H$) hysteresis loop in a usual ferromagnet which spans over all four quadrants. The minor loops and the retaining of the end point memory is clearly seen in this case. Reproduced from ref. [40].

cooling curve till the temperature ‘A’ and then cycled along the path ‘A-B-C-D-A’. During this cycling, the temperature is increased from ‘A’ to ‘C’ without reaching the envelope heating curve (the extreme right curve in figure 5.3(a)) and then decreased back to the initial temperature value ‘A’, from where the first reversal of the direction of temperature change took place. It is interesting to note that the strain after the cycling along the MHL returns back to its original value. Such *memory* of returning back to the initial value is known as either the return-point-memory or the end-point-memory (EPM).^{79,80} Figure 5.3(b) shows the $B-H$ (or $M-H$) hysteresis in a usual ferromagnet with the minor loops showing the end point memory.

Apart from the EPM there is one more feature which is common to all the MHLs irrespective of the temperature value or the history of initiation. Suppose instead of following the path ‘C-D-A’, there is one more smaller to and fro cycling of the temperature between ‘D’ and ‘E’. The path followed now starting from the envelope cooling curve is ‘A-B-C-D-E-D-A’. Here we observe that the memory of the cycle

between ‘D’ and ‘E’ is *wiped out*. In general, during any MHL, the *memory* of the smaller excursion of the input variable is wiped out if an excursion with larger values of extrema is carried out over a path which includes one of the end points of the smaller excursion. The wiping out property and the retaining of the EPM is found to be valid over entire temperature range and are irrespective of the temperature history of reaching to a particular value. We shall later see in more details the result of a similar temperature cycling where the path ‘D-E’ is actually hysteretic.

The *landscape* of transition temperatures is able to explain the broad first order transition (figure 5.1), the relation between the onset temperatures during heating and cooling on the envelope curve (figure 5.1) and the phase coexistence across the transition (figure 5.2). We now try to understand the general features of the MHLs (figure 5.3) in terms of the landscape picture.

5.4 The Preisach model of hysteresis

We propose here that a natural way in which the landscape picture and the properties of the MHLs (figure 5.3) can be related is through the Preisach model of hysteresis.⁷⁸ Though the original model was proposed for explaining the hysteresis in a ferromagnet,⁷⁸ the assumptions of the model can be directly used for explaining other types of hysteresis also, like the stress-strain hysteresis loop in shape memory alloys.⁸¹ The basic assumption of the Preisach model is that the complete hysteresis curve can be thought of as a summation of elementary hysteresis operators (or *hysterons*) defined in figure 5.4. The switching operator $\gamma_{\alpha\beta}$ is chosen such that $\gamma_{\alpha\beta} \times T$ is either 0 or 1, where T is the input. The value of the hysteresis operator switches to 1 at $T = \alpha$ on the temperature increasing cycle and switches back to 0 at $T = \beta$ during the temperature decreasing cycle. In the original model for describing the hysteresis in a ferromagnet, the output values of the hysteron switch between -1 to +1. However,

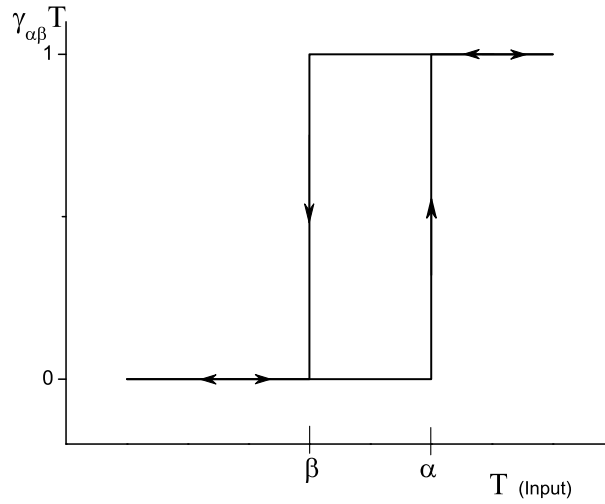


Figure 5.4: The definition of an elementary hysteresis operator according to the Preisach model for explaining the hysteresis in figure 5.1.

our hysteresis curve is limited to only the first quadrant and thus the definition of the hysteresis operator is chosen as shown in figure 5.4.

The output $\varepsilon(T)$ is then given by⁷⁸

$$\varepsilon(T) = \int \int_{\alpha \geq \beta} \mu(\alpha, \beta) [\gamma_{\alpha\beta} T] d\alpha d\beta, \quad (5.1)$$

where $\mu(\alpha, \beta)$ is the distribution function or the weight factor associated with each hysteresis operator. The schematic of this equation is shown in figure 5.5. In a normal hysteresis curve, the value of the input parameter at which the switching takes place during the forward cycle is always larger than that during the reverse cycle. Thus the limit of integration is within the domain $\alpha \geq \beta$. The entire hysteresis curve can be described if the distribution function $\mu(\alpha, \beta)$ is known.

The equivalence of the landscape picture and the Preisach model comes from the assumption of the Preisach model that each of the hysterons has its own hysteresis, i.e. independent α and β values. This particular assumption appears to be valid, at least on the micrometre length scales, for samples undergoing first order transition. Local imaging of phase coexistence across first order transition has established that different pockets of the sample undergo transition at different values of the driving

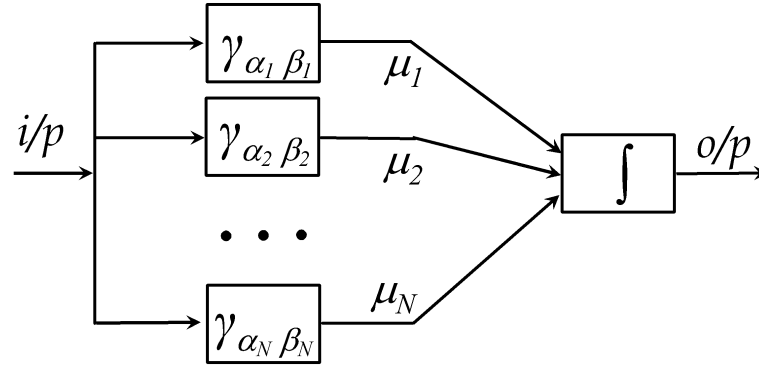


Figure 5.5: A pictorial representation of the Preisach model given in equation 5.1.

force like temperature or magnetic field.^{51–53} During the back transformation, the sample volume which transforms first during the forward cycle is the last to transform back to the original state.^{52,53} This observation clearly shows that each of the sample pockets has its own hysteresis, which validates the applicability of the Preisach model to first order transitions.

5.5 Modeling of minor hysteresis loops

The central problem now is to identify a proper distribution function from the bulk measurements which will explain the hysteresis and the behaviour of MHLs under multiple cycling. For this purpose, we analyze the *first order reversal curves* (FORC), or the first reversal curves which are initiated on the envelope heating curve. To obtain any FORC, the temperature is increased monotonically in to the hysteretic region from below the reversible region on the low temperature side. The temperature below which the strain is reversible is denoted as β_0 . The temperature is increased to a value α , where the value of strain is ε_α (see figure 5.6(a)). After reaching α , the direction of the temperature change is ‘reversed’ (i.e. decreased) till a value β . The value of the output on this FORC is then denoted as $\varepsilon_{\alpha\beta}$. This notation is chosen to take in to account the initial and final values of the temperature history to reach to a particular value of output.

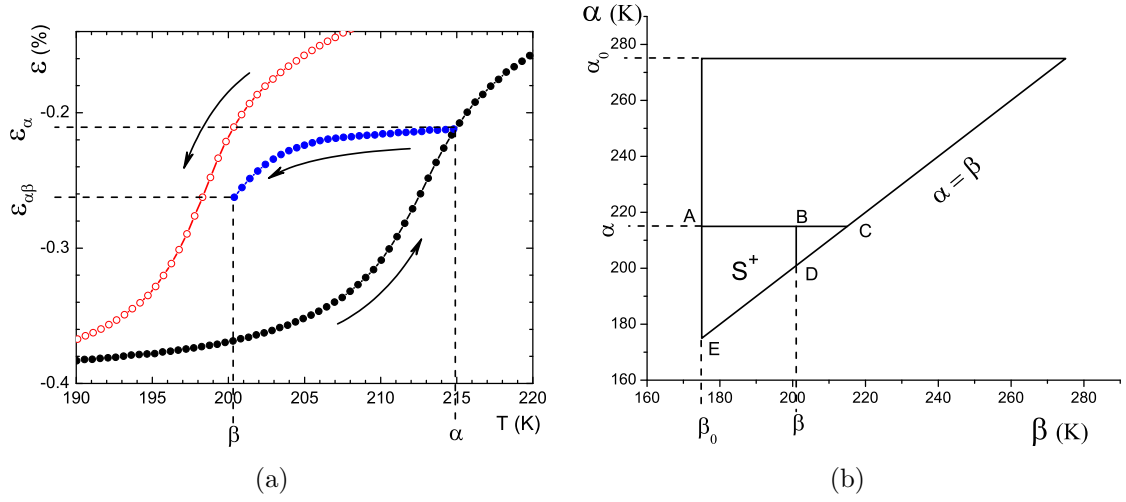


Figure 5.6: (a) One example of the first order reversal curve across the first order transition in $\text{Fe}_{0.955}\text{Ni}_{0.045}\text{Rh}$ and (b) The equivalent construction of the thermal cycling in the $\alpha\beta$ plane.

The same temperature excursion can be represented in the $\alpha\beta$ plane as in figure 5.6(b). The triangle in the $\alpha\beta$ plane is bound by $x = \beta_0$, $y = \alpha_0$ and $\alpha = \beta$ lines. The domain of integration of equation 5.1 lies within this triangle for the entire major loop or the envelope curve. Each temperature increase is represented by a horizontal line moving from bottom to top and each temperature decrease is represented by a vertical line moving from the right to left. For the FORC in figure 5.6(a), the first temperature increase from below β_0 to α is shown by the horizontal line ‘A-B-C’. The output strain ε_α on the envelope heating curve for this temperature cycle is then given by equation 5.1, with the domain of integration as the triangle ‘A-C-E’. All the hysterons which belong to the triangle ‘A-C-E’ will have switched their state from 0 to +1. When the temperature is decreased from α to β , the path in the $\alpha\beta$ plane moves along the vertical line ‘B-D’ towards the left hand side. The hysterons in the triangle ‘B-C-D’ will switch their states back to zero and the value of the measured output will decrease. The output strain $\varepsilon_{\alpha\beta}$ is now given again by equation 5.1, with the domain of integration denoted by S^+ , which is the region bound by ‘A-B-D-E’. The region ‘A-B-D-E’ can be constructed by subtracting the area of triangle ‘B-C-D’ from that of the triangle ‘A-C-E’. This subtraction allows us to define a function

$F(\alpha, \beta)$, such that

$$F(\alpha, \beta) = \varepsilon_\alpha - \varepsilon_{\alpha\beta}. \quad (5.2)$$

This definition is similar to the one used in case of stress-strain hysteresis curve.⁸¹ In case of the hysteresis in ferromagnets, the function $F(\alpha, \beta)$ is taken to be half of what is given in the above equation.⁷⁸ This difference arises because the hysteresis in our case is contained only in the first quadrant and can be explained by a 0 to 1 switch, in place of -1 to +1.

From the above definition, it can be seen that

$$F(\alpha, \beta) = \int \int_{B-C-D} \mu(\alpha, \beta) [\gamma_{\alpha\beta} T] d\alpha d\beta, \quad (5.3)$$

where B-C-D is the triangular region shown in figure 5.6(b).

Differentiating first with respect to β' and then α' , we get

$$\mu(\alpha', \beta') = -\frac{\partial^2 F(\alpha', \beta')}{\partial \alpha' \partial \beta'}. \quad (5.4)$$

Here we have replaced the dummy variables to α' and β' .

So if a collection of all the FORC is available for all the α, β values, then the distribution function can be determined. However, the practical difficulty in this approach is that any noise in the experiment gets amplified due to the double derivative and it may become quite impossible to obtain any meaningful information.

The MHLs can be determined without actually using equation 5.4 if the definition of $F(\alpha, \beta)$ from equation 5.3 is used along with the geometric construction for each temperature excursion as shown in figure 5.6(b). Figure 5.7(a) shows two minor hysteresis loops or a loop within a loop. The bigger MHL is generated by decreasing the temperature from α_1 to β_1 , then increasing the temperature to α_2 and finally reducing the temperature to below β_1 . The inner MHL is generated by following the

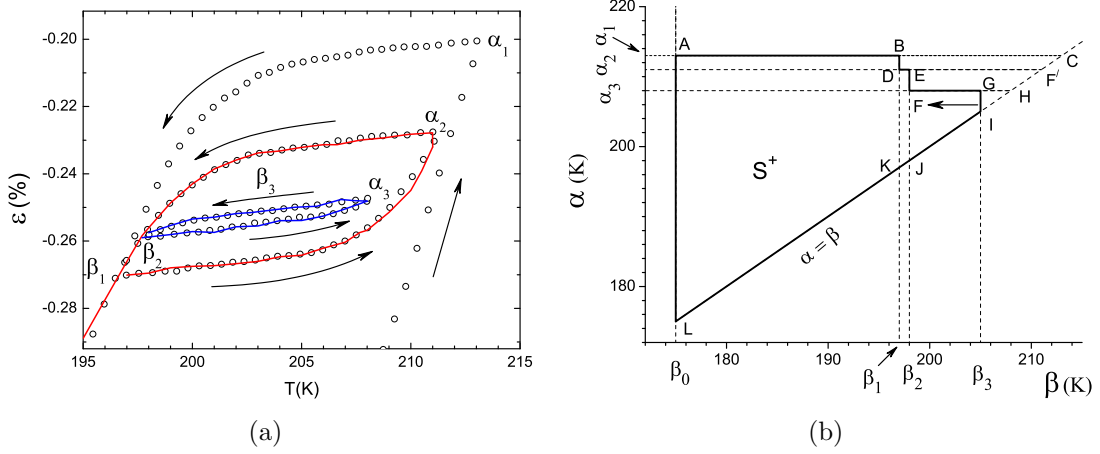


Figure 5.7: (a) A larger and smaller minor hysteresis loop showing the end-point-memory and wiping out property respectively in $\text{Fe}_{0.955}\text{Ni}_{0.045}\text{Rh}$. The solid lines are calculated using equations 5.7 and 5.9. (b) The geometric construction in the α, β plane showing the temperature excursion for the inner minor hysteresis loop.

path $\alpha_1\text{-}\beta_1\text{-}\alpha_2\text{-}\beta_2\text{-}\alpha_3$ and then reducing the temperature to β_3 . The EPM is observed at β_1 and the wiping out of the memory of the smaller excursion between β_2 to α_3 and back, is observed at β_2 . The geometric representation of the temperature excursion for obtaining this inner MHL is shown in figure 5.7(b). Each horizontal line represents the increase of temperature and the vertical line represents the decrease of temperature. The final decrease is along the line ‘G-I’ which moves to the left as the temperature is decreased. The value of the output strain is then given by equation 5.1 with the domain of integration bound by the region S^+ which is the area ‘A-B-D-E-F-G-I-L-A’. This area S^+ can be constructed as a summation of smaller trapezoids like ‘A-B-K-L’, ‘D-E-J-K’ and so on. The area ‘A-B-K-L’ is obtained by subtracting the area of triangle BCK from the triangle ACL. The triangle ACL is bound by α_1, β_0 and is denoted by $\Delta(\alpha_1, \beta_0)$. Similarly the triangle BCK is bound by α_1, β_1 and is denoted by $\Delta(\alpha_1, \beta_1)$. If the temperature is increased up to α_1 and then decreased to β_1 , the output strain will be given by:

$$\varepsilon_{\alpha_1\beta_1} = \int \int_{A-B-K-L} \mu(\alpha, \beta) [\gamma_{\alpha\beta} T] d\alpha d\beta, \quad (5.5)$$

which can be rearranged as:

$$\varepsilon_{\alpha_1\beta_1} = \int \int_{\Delta(\alpha_1, \beta_0)} \mu(\alpha, \beta) [\gamma_{\alpha\beta} T] d\alpha d\beta - \int \int_{\Delta(\alpha_1, \beta_1)} \mu(\alpha, \beta) [\gamma_{\alpha\beta} T] d\alpha d\beta, \quad (5.6)$$

which is just equal to $F(\alpha_1, \beta_0) - F(\alpha_1, \beta_1)$ as can be seen from the definition of $F(\alpha, \beta)$ in equation 5.3. The output strain related to the other trapezoids in figure 5.7(b) can be calculated in a similar manner. In general the output strain in terms of $F(\alpha, \beta)$ can be written as:

$$\varepsilon(T) = \sum_{i=0}^{N-1} \left[F(\alpha_{i+1}, \beta_i) - F(\alpha_{i+1}, \beta_{i+1}) \right], \quad (5.7)$$

where the last term β_N contains the temperature (or the input). Representing in this form allows one to avoid the double derivative which can lead to noise. Also, there is no adjustable parameter involved in this calculation and all the data are used from the measured FORC initiated at closely spaced temperature intervals. Figure 5.7(a) shows two calculated curves using equation 5.7, α_2 to β_1 and α_3 to β_3 , on the temperature decreasing path. The experimental data on the temperature decreasing cycle is described quite well using this equation. In equation 5.7, the current temperature is β_N . The value of the last term is $\varepsilon_{\alpha_N} - \varepsilon_{\alpha_N\beta_N}$. This means that the temperature-decreasing portion of the curve can be obtained from the first reversal curve initiated at α_N on the envelope heating curve.

We now see the calculation for the temperature increasing cycle. Figure 5.8(a) shows a MHL initiated on the envelope cooling cycle at a temperature β_1 . In the $\alpha\beta$ plane this decrease is represented by a vertical line ‘B-C-I’ (see figure 5.8(b)). The temperature increase till α_2 is shown by the line ‘C-D-E’. The earlier discussion for arriving at equation 5.7 holds here also except that the term for the last temperature increase has to be added separately. The output strain due to the last temperature

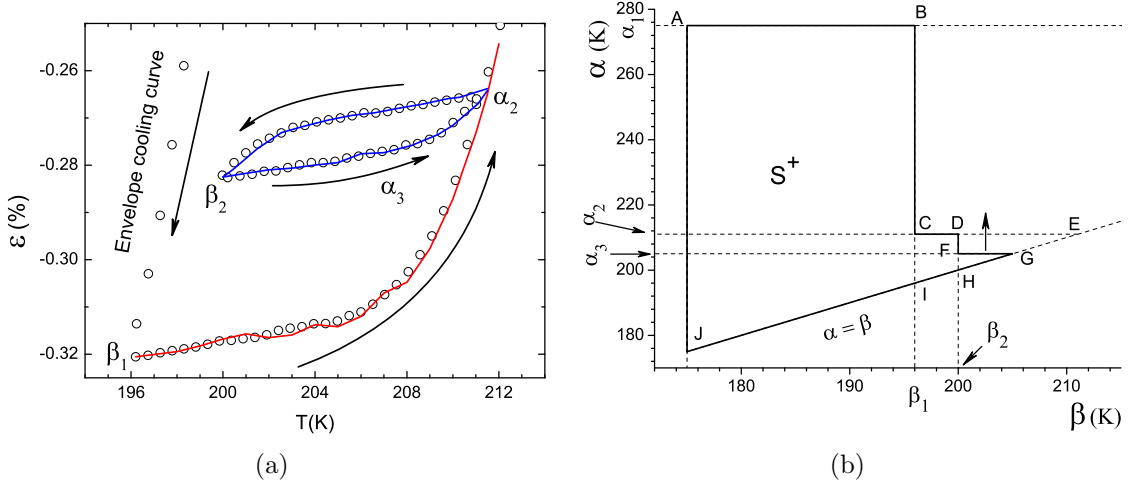


Figure 5.8: (a) MHL initiated on the envelope cooling curve in $\text{Fe}_{0.955}\text{Ni}_{0.045}\text{Rh}$. The solid lines are calculated using equations 5.7 and 5.9. (b) Geometrical representation of the temperature cycling in the $\alpha\beta$ plane.

increase from β_2 to (or along) α_3 is given by equation 5.1 with the domain of integration as the triangle ‘F-G-H’. The last temperature increase is represented by the horizontal line ‘F-G’ moving upwards. The triangle ‘F-G-H’ is bound by α_3, β_2 and thus from the discussion on equation 5.3, the output strain for the last temperature increase will be just $F(\alpha_3, \beta_2)$.

The total output strain will then be:

$$\varepsilon(T) = \sum_{i=0}^N \left[F(\alpha_{i+1}, \beta_i) - F(\alpha_{i+1}, \beta_{i+1}) \right] + F(\alpha_3, \beta_2). \quad (5.8)$$

Adding and subtracting $F(\alpha_0, \beta_0)$, the total output strain for the last temperature increase will be:

$$\varepsilon(T) = F(\alpha_0, \beta_0) - \sum_{i=0}^N \left[F(\alpha_i, \beta_i) - F(\alpha_{i+1}, \beta_i) \right]. \quad (5.9)$$

Here α_{N+1} is the current temperature. The solid lines in figures 5.7(a) and 5.8(a) are calculated using the combination of equations 5.7 and 5.9 for the temperature decreasing and temperature increasing curves respectively. The calculated curves

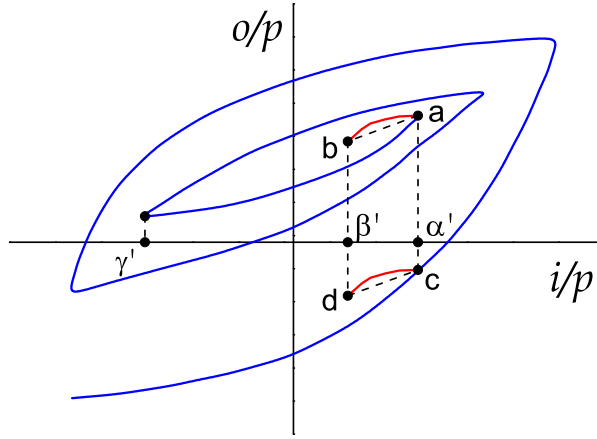


Figure 5.9: Schematic of minor hysteresis loops to explain the meaning of ‘congruency’.

also show EPM and the wiping out property which is a natural outcome of the Preisach model.⁷⁸ Thus the applicability of the Preisach model to first order phase transition not only is justified from the basic equivalence of the landscape picture and the hysterons, but also from the outcome of this assumption like the EPM and wiping out property. The reasonably good description of the experimental results by the calculation comes from the congruence of the MHLs with the FORC generated on the envelope curve.⁷⁸ The last terms in both the summations in equations 5.7 and 5.9 contain the temperature dependence of the output strain when the curve is initiated on the envelope heating curve. This clearly means that an MHL generated inside the hysteretic region is self-similar or congruent to the curve generated with the same temperature values on the envelope curve. An example of congruence is shown in figure 5.9 where the output curves ‘a-b’ and ‘c-d’ between the temperatures α' and β' are similar to each other irrespective of the input history followed to reach to the starting point.

5.6 Deviations from the Preisach model

The observation of congruence however breaks down for large temperature excursions along the MHL as we see in figure 5.10. Figure 5.10 shows two MHLs generated

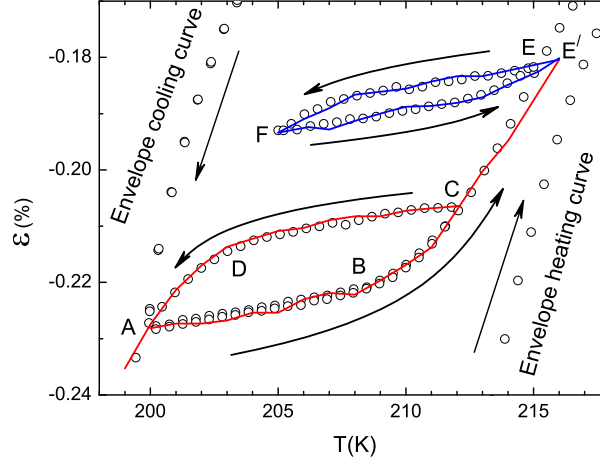


Figure 5.10: Results of calculation (solid lines) using equations 5.7 and 5.9 along with the experimental data (open circles) of $\text{Fe}_{0.955}\text{Ni}_{0.045}\text{Rh}$ which show the breakdown of Preisach model for larger temperature excursions.

on the envelope cooling curve. The first MHL is along the path ‘A-B-C-D-A’ and further cooling. The second one is along ‘A-B-C-E-F-E’ and further heating. For the first MHL, the calculation matches quite well with the experimental data with both the data and calculation showing EPM. For the second MHL, the calculation starts deviating around 213 K and then consistently gives lower values of output strain compared to the experimental data. However, the EPM is observed in the experiment at the temperature E. In the calculation, the EPM is still retained and is observed at E’ instead of E. This behaviour is consistently observed for all the MHLs when the temperature excursion goes beyond 213 K on the heating cycle and 195 K on the cooling cycle.

It was also noted by other authors⁸² that the Preisach model explains the MHLs better only somewhere near the *middle* of the transition but not near the *tails*. We feel that this failure comes due to the lack of congruency between the FORC on the envelope curve and the MHLs when there is a crossover from the nucleation dominated process to the growth oriented process across the transition. It appears that the EPM is always retained irrespective of the range of temperature cycling, i.e. irrespective of the underlying physical process of nucleation or growth, whereas the congruency

is lost. The congruency may be lost during the growth because different pockets of the transformed phase now merge together, which may thus contradict the basic assumption of the Preisach model of independent hysteresis operators. Probably after a particular length scale of coalescence, the different pockets of the transformed phase may influence each other and no longer remain independent.

This observation poses interesting questions about the phenomena occurring during first order phase transitions which are influenced by disorder. Does the EPM occur over smaller length scales (over a few nanometres) also where the hysterons can still be treated as independent, or the observed EPM in bulk measurements is just an ensemble average of all the uncorrelated stochastic events? The congruency appears to be independent of EPM in the experimental observation, whereas both of them are related in the original Preisach model.⁷⁸ Similar questions have been posed for the case of hysteresis in ferromagnets.⁷⁹ It was shown there that the EPM is a result of an ensemble average and does not occur on the local scale.⁷⁹ By carefully controlling the disorder in ferromagnetic films, it was shown that the microscopic EPM does not occur in *clean* samples but is partially recovered by increasing the disorder, though the macroscopic EPM is observed for all the samples.⁸⁰ Our results presented here show that similar experiments are now required for first order phase transitions in presence of carefully controlled disorder which will probe for EPM and congruency at various length scales.

5.7 Summary

As an extension to the results presented in the earlier chapters, we have measured the linear strain as a function of temperature and magnetic field across the first order transition in $\text{Fe}_{0.955}\text{Ni}_{0.045}\text{Rh}$. The presence of phase coexistence across the transition is inferred using the technique of minor hysteresis loops. These minor

hysteresis loops are found to retain the memory of the last reversal of temperature change, over the entire temperature range and irrespective of the temperature history followed to reach the point of initiation. The smaller temperature excursion is wiped out by a larger excursion if the larger excursion contains one of the extrema of the smaller excursion. The picture of landscape of transition temperatures, which arises in a disorder influenced first order phase transition as seen in the earlier chapters, is correlated with the Preisach model of hysteresis. The assumptions used in the earlier chapter to infer the phase fraction from bulk measurements across a first order transition (i.e. different locations of the sample having their own hysteresis) appear to be reasonably valid. The Preisach model appears to fail beyond a certain range of temperature excursion, most probably due to a crossover from nucleation to growth across the transition. Our observations pose certain questions on the retention of memory of a temperature cycling, which need further experiments at various length scales on samples prepared with carefully controlled disorder. We believe that these future experiments could provide further information which is useful for tuning the functional properties of smart materials whose applications are based on first order phase transition.

Publications based on this chapter

- 1) Thermo-magnetic history effects in the giant magnetostriction across the first order transition and minor hysteresis loops modeling in $\text{Fe}_{0.955}\text{Ni}_{0.045}\text{Rh}$ alloy
M. Manekar, V. K. Sharma and S. B. Roy
J. Phys.: Condens. Matter, **24**, [216004](#) (2012).

Chapter 6

Thermomagnetic history effects in the multi-functional properties of Fe-Rh based alloys

6.1 Introduction

In the earlier chapters we first established the presence of phase coexistence and metastability across the first order transition through local imaging and bulk measurements. The nucleation and growth dynamics along with the identification of the phase fraction during transformation were also studied. This understanding was then used to study the history effects inside the hysteretic region of the temperature driven transition. The history effects during the transition caused by a single external variable like temperature was modeled by using the Preisach model of hysteresis. In this chapter we study the history effects and their influence on the functional properties when the first order transition can be driven by two thermodynamic variables like the temperature and magnetic field. The functional properties we study are the giant magnetocaloric effect and giant magnetostriction. This study of the thermomagnetic

history effects helps in solving the long standing problem of the vanishing magnetocaloric effect in Fe-Rh as we had mentioned in chapter 1 as a part of our motivation behind this work. The physical properties that are measured to study these history effects are mainly the field and temperature dependent dc magnetization and linear strain.

We observe interesting thermomagnetic history effects, which are interpreted in terms of a disorder influenced first order phase transition and associated features like phase coexistence and metastability. The importance of understanding these history effects is highlighted in the context of achieving repeatable functional properties of the Fe-Rh alloy in particular, and any other material which undergoes a first order magneto-structural transition, in general.

6.2 Thermomagnetic history effects in magnetization measurements

Thermomagnetic history effects across a first order magneto-structural transition have been studied extensively in recent years in a variety of materials.^{83–85} (Also see Roy and Chaddah¹¹ for an extensive review). Recently, some interesting thermomagnetic history effects in Fe-Rh epitaxial thin films have been reported.⁸⁶ These history effects were interpreted in terms of complex nucleation processes that occur across a first order transition. It has also been stated that though Fe-Rh exhibits a giant MCE close to room temperature, the magnetocaloric effect vanishes after the first field cycle.^{25,30,31} This observation makes it necessary to further investigate the effect of temperature and field cycles on the Fe-Rh alloy system and verify the above result. In this chapter, we show that Fe-Rh indeed exhibits a repeatable behaviour and does not lose its magnetic properties if the starting point of the field cycle in the $H - T$ phase space is chosen properly. As our discussion is based only on the generic features

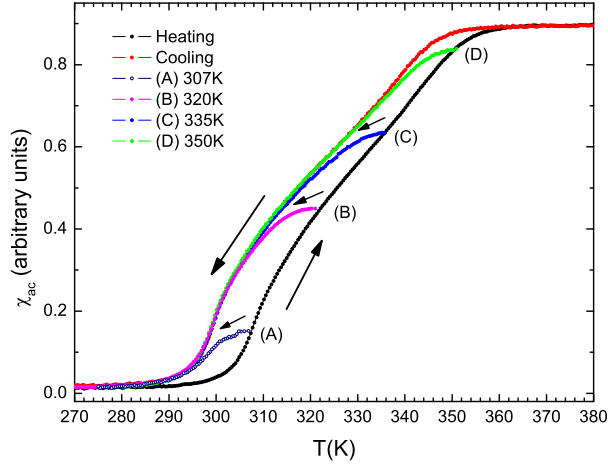


Figure 6.1: Ac susceptibility of $\text{Fe}_{48}\text{Rh}_{52}$ as a function of temperature in a magnetic field of 3.4×10^{-4} T rms. The temperatures of initiation of the minor hysteresis loops are marked as A, B, C and D. See text for details.

like phase coexistence and metastability across a first order transition and not on the specific microscopic interaction, the history effects are not limited to only the Fe-Rh system. Such history effects should be seen in other systems as well which undergo a similar first order magneto-structural transition.

Figure 6.1 shows ac susceptibility of $\text{Fe}_{48}\text{Rh}_{52}$ as a function of temperature both while heating and cooling the sample. The measurement is performed in the temperature range from 80 K to 380 K, but only the temperature range which shows the antiferromagnetic to ferromagnetic transition is presented here for clarity. The onset of the antiferromagnetic to ferromagnetic transition during warming occurs at about 300 K. The conversion from the antiferromagnetic phase to ferromagnetic phase is completed at around 365 K, beyond which the susceptibility shows a reversible behaviour. On cooling, a thermal hysteresis of about 10 K is observed across the transition and the conversion from ferromagnetic to antiferromagnetic phase gets completed at around 280 K. This indicates that the ferromagnetic phase can be supercooled down to 280 K. It is well known that the transition parameters like the onset temperatures and the width of the transition are quite sensitive to the heat treatment schedule.²⁴ Since our sample has been subjected to prolonged annealing, the transition occurs

over a broader temperature interval compared to the case of a quenched sample.²⁴ The difference of temperatures between the two reversible regions, low temperature antiferromagnetic and the high temperature ferromagnetic, is quite large (≈ 85 K). This indicates that (as discussed in the earlier chapters), both while heating and cooling, the transition proceeds through a heterogeneous nucleation of the product phase in the parent matrix. The sample is thus in a phase coexistent state between the two reversible regions. The MHLs highlight the presence of phase coexistence. As we have discussed in the earlier chapter, the temperature change has to be strictly unidirectional to observe an MHL. Oscillation of temperature around the temperature set-point is prevented by slowly ramping the temperature and recording the data dynamically instead of stabilizing at each temperature. Typically, the temperature is ramped at a rate of 0.6 K/min or less. In such a situation where the temperature is not allowed to stabilize, it is important to minimize the lag between the temperature sensor and the sample. This has been ensured for our set-up in different temperature ranges.^{43,44} We show four representative MHLs in figure 6.1 which are initiated on the warming cycle. As the MHLs are initiated on the warming cycle, the area enclosed by each MHL is proportional to the amount of the growing ferromagnetic phase. The relationship between the onset and completion temperatures of the phases involved in the transition show that the transition is influenced by disorder (See the discussion related to figure 1.7).

Figure 6.2 shows temperature dependent magnetization measurement in $\text{Fe}_{48}\text{Rh}_{52}$, both while warming and cooling, performed in a field of 1 T. The application of field shifts the onset temperature of the antiferromagnetic to ferromagnetic transition to about 295 K. The magnetization is reversible below 265 K, which indicates that the ferromagnetic phase can be supercooled down to 265 K in presence of 1 T field. Similarly, application of higher fields shifts the onset temperatures to even lower values. The application of 2 T field changes the onset of the antiferromagnetic to ferromag-

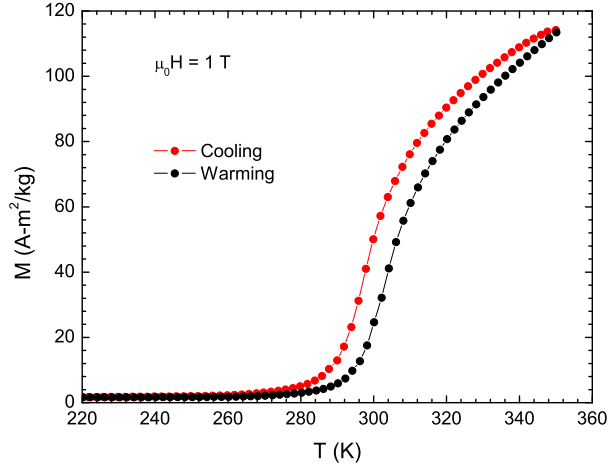


Figure 6.2: Magnetization of $\text{Fe}_{48}\text{Rh}_{52}$ as a function of temperature in a magnetic field of 1 T.

netic transition to about 282 K and the ferromagnetic phase can be supercooled down to almost 245 K. All the magnetization curves show reproducible behaviour irrespective of the number of temperature cycles experienced by the sample. This is in contrast with the observation made by Annaorazov et al.²⁵ where the transition parameters stabilized only after about 10 cycles. Their sample was quenched from 1000 °C in ice cold water whereas our sample was cooled slowly at a rate of 2 °C from the annealing furnace.

Having established the presence of phase coexistence and the effect of applied magnetic field across the temperature driven transition, we now study the effect of field variation at constant temperatures. The antiferromagnetic to ferromagnetic transition is also known to be induced by the isothermal application of magnetic field.¹⁶ Thus, it would be interesting to study the effect of magnetic field on a phase coexistent state.

Figure 6.3 shows one such isothermal magnetization measurement at 270 K. The sample was warmed from below 200 K up to this temperature in zero field. With this temperature and field history, the sample is expected to be entirely in the antiferromagnetic state as can be seen from figure 6.1. The onset of the field-induced antiferromagnetic to ferromagnetic transition (metamagnetic transition) occurs at

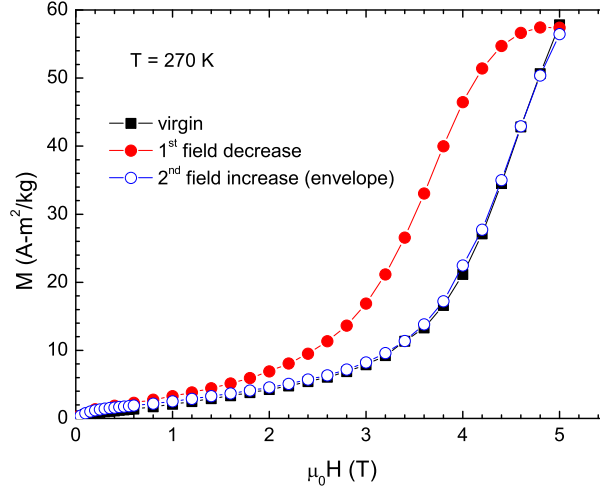


Figure 6.3: Magnetization of $\text{Fe}_{48}\text{Rh}_{52}$ as a function of field at 270 K.

around 3 T and the transition is still incomplete till 5 T, which is the highest possible field in our magnetometer. On decreasing the field, there is a large hysteresis across the transition. The curve for the next field increase (envelope curve) is obtained after the first field cycle both in the positive and negative direction is completed. The envelope curve nearly follows the virgin magnetization curve (within experimental error) and this envelope curve is retraced in subsequent cycles.

Figure 6.4 shows the magnetization measurement at $T = 290$ K. As before, the sample was warmed up to this temperature in zero field. The temperature 290 K is still below the onset of the antiferromagnetic to ferromagnetic transition (see fig. 6.1) and the sample is expected to be a single phase antiferromagnet in zero field. The onset of the metamagnetic transition is around 1.4 T. Since the starting conditions of figure 6.3 and 6.4 are the same, it is expected that same result of a nearly overlapping envelope and virgin curve should be reproduced. However, we see that the magnetization on the envelope curve is distinctly higher than that of the virgin curve and we get a situation where the virgin curve lies outside the envelope curve. The virgin curve can be recovered back only by first cooling the sample in zero field below 200 K and then coming back to 290 K in zero field.

Figure 6.5 shows the isothermal $M-H$ curve at 305 K. At this temperature, in zero

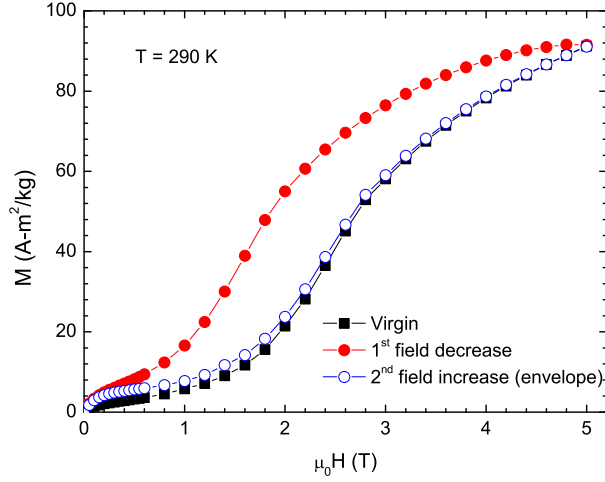


Figure 6.4: Magnetization of $\text{Fe}_{48}\text{Rh}_{52}$ as a function of field at 290 K.

field, the conversion from the antiferromagnetic to ferromagnetic phase has already started and the sample is in the phase coexistent state as can be seen from figure 6.1. The starting condition for the $M - H$ curve in figure 6.5 is thus quite different from that in figure 6.4 where the sample was entirely in the antiferromagnetic state. Here the onset of the metamagnetic transition cannot be defined in a unique manner as some fraction of ferromagnetic phase is already present. However, we see a slight change of curvature in the virgin curve at around 0.8 T which probably is due to a large fraction of sample getting converted from the antiferromagnetic to ferromagnetic state. Here again the field induced transition is not completed till 5 T. Though the initial condition of the $M - H$ curve in figure 6.5 is completely different compared to that in figure 6.4, we see a similar behaviour of the virgin curve lying outside the envelope curve. Only the difference of magnetization between the envelope and virgin curve is much larger at 305 K, which is due to the stable ferromagnetic phase coexisting with the antiferromagnetic phase even before the field is applied.

To further probe the nature of this phase coexistence, relaxation measurements at various fields are performed at $T = 305$ K on the virgin magnetization curve and envelope curve. figure 6.6 shows the results of such measurements. For relaxation measurements on the virgin curve (see figure 6.6(a)), the sample is first warmed up to

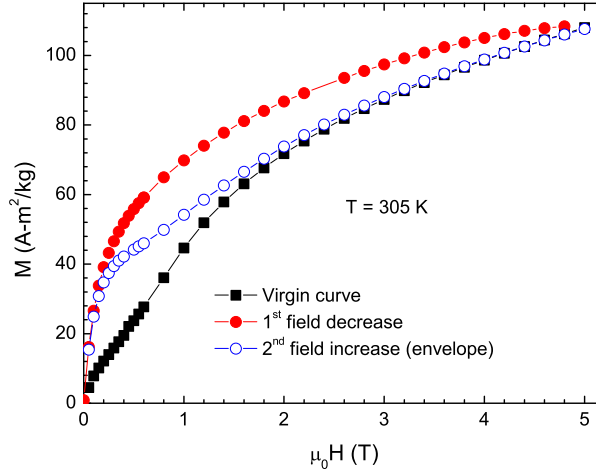


Figure 6.5: Magnetization of $\text{Fe}_{48}\text{Rh}_{52}$ as a function of field at 305 K.

305 K in zero field from below 200K. The field at which the measurement is performed (say 0.4 T) is achieved with the same field steps as shown in figure 6.5. Magnetization is then measured as a function of time after stabilizing the field. For measurements at other fields, the sample is again cooled below 200K in zero field and then warmed back to 305 K. The desired field value is achieved with the same protocol of field variation used in figure 6.5 and then the magnetization is measured as a function of time. A finite relaxation towards higher magnetization is seen at all the field values presented in figure 6.6(a). This indicates that the antiferromagnetic phase is metastable (superheated) and gets converted to the stable ferromagnetic phase. The degree (amount) of relaxation is lesser at higher fields, which shows that most of the conversion from the metastable antiferromagnetic phase to the stable ferromagnetic phase has taken place. Also the degree of relaxation increases initially up to 0.6 T and then gradually reduces at higher fields, which is typical of a disorder influenced first order transition.¹⁰

The relaxation on the envelope curve (see figure 6.6(b)) is measured by achieving the same field history for a particular field value as obtained in figure 6.5. For each measurement, the sample is first warmed up to 305 K from below 200 K and then the field cycle is completed both for the positive and negative values of field. This way

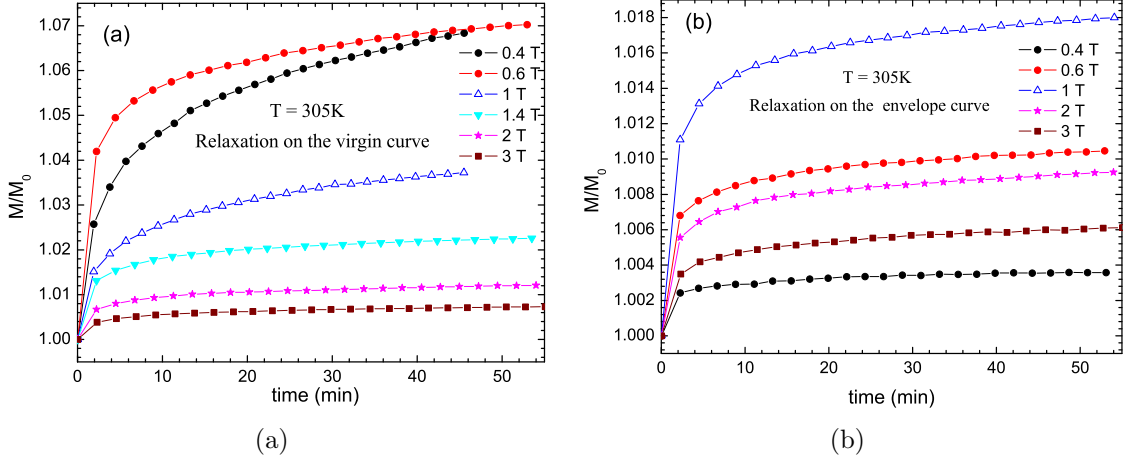


Figure 6.6: Magnetic relaxation measurements on $\text{Fe}_{48}\text{Rh}_{52}$ at 305 K. (a) Relaxation on the virgin curve. (b) Relaxation on the envelope curve. M_0 is the value of magnetization for the first measurement.

each field point on the envelope curve is obtained and then magnetization is measured as a function of time for that field value. Here again we see a finite relaxation from the antiferromagnetic state to the ferromagnetic state. However, it should be noted that the maximum change in magnetization (relaxation in 1 T field, see figure 6.6(b)) is less than 2% on the envelope curve whereas the maximum change of magnetization on the virgin curve is about 7% (see figure 6.6(a)). This clearly indicates that large amount of the metastable antiferromagnetic phase has been converted to stable ferromagnetic phase during one field cycle. Thus the envelope curve in figure 6.5 corresponds to a state where more quantity of the ferromagnetic phase is present in the sample and therefore lies above the virgin magnetization curve.

$M - H$ measurements performed at various temperatures show a varying amount of the virgin curve lying outside the envelope curve. Figure 6.7 shows ΔM (the difference of magnetization on the envelope and virgin curves) as a function of field at various temperatures. As the temperature increases, there is an initial increase in the maximum value of ΔM and then there is a gradual drop. In the following discussion we attempt to relate this behaviour of the virgin curve with the growing fraction of the ferromagnetic phase as a function of temperature.

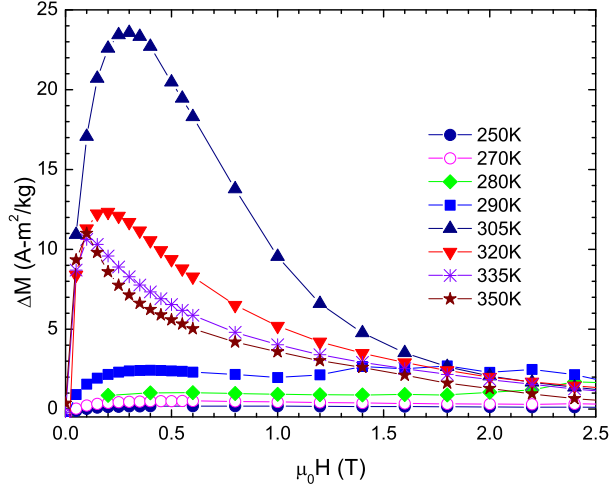


Figure 6.7: Difference of magnetization of $\text{Fe}_{48}\text{Rh}_{52}$ on the envelope curve and the virgin curve as a function of temperature.

Virgin curve can lie outside the envelope curve due to the kinetic arrest of a first order phase transition as seen in the case of CeFe_2 based alloys,^{83,87} Gd_5Ge_4 ,⁸⁸ MnSi ,⁸⁹ Nd_7Rh_3 ,⁹⁰ and manganites.^{85,91} However, we see a finite relaxation on the virgin as well as the envelope curve (see figure 6.6), which does not follow the usual stretched exponential behaviour for glassy dynamics and thus rules out the possibility of a kinetic arrest of the transition. (We shall discuss the results on the arrested kinetics of a first order transition in the next chapter.)

We discuss below the possibility of the virgin curve lying outside the envelope curve in terms of generic features of a disorder broadened first order transition. In such cases, the transition line in the $H - T$ phase diagram becomes a band of transition temperatures and fields.⁸⁷ An $H - T$ phase diagram for our sample (see figure 6.8) is constructed from the actual experimental data on isothermal and isofield magnetization as follows. The field and temperature values for the limit of supercooling of the ferromagnetic phase are determined from the zero-field ac susceptibility and temperature dependent magnetization measurements in finite fields. (See the discussion on figures 6.1 and 6.2).

These values are used to plot the (H^*, T^*) line, which represents the limit of

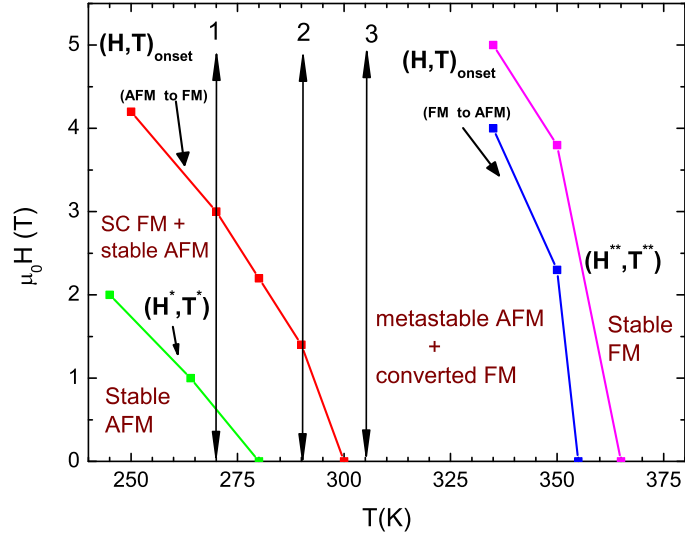


Figure 6.8: $H - T$ phase diagram of $\text{Fe}_{48}\text{Rh}_{52}$ constructed from magnetization measurements.

metastability for the ferromagnetic phase, following the standard notation.⁷ Below this line it is not possible to retain the ferromagnetic phase in the supercooled (metastable) state. Similarly from the zero field susceptibility and the isothermal field-dependent magnetization at various temperatures, the field and temperature values are determined beyond which the magnetization is reversible in the stable ferromagnetic state. These values are used to plot the (H^{**}, T^{**}) line which indicates the upper limit of metastability of the antiferromagnetic phase.⁷ Beyond this line the antiferromagnetic phase cannot be superheated and the entire sample is in the stable ferromagnetic phase. The region between the (H^*, T^*) and the (H^{**}, T^{**}) lines is that region where both the antiferromagnetic and ferromagnetic phases coexist.

We now see the details of this phase coexistent region. The onset temperatures of the antiferromagnetic to ferromagnetic transition at various fields are obtained from the ac susceptibility and temperature dependent magnetization measurements as discussed before. These values give the $(H, T)_{\text{onset}}$ (AFM to FM) line. Below the $(H, T)_{\text{onset}}$ (AFM to FM) line, the antiferromagnetic phase is still stable as it has not undergone any transformation either by increasing the field or temperature. However, during the back transformation from ferromagnetic to antiferromagnetic

phase, some amount of the ferromagnetic phase can remain supercooled (*SC FM*) between the (H^*, T^*) line and the $(H, T)_{onset}$ (AFM to FM) line as the field and temperature values are still not below the (H^*, T^*) line. So the region between the (H^*, T^*) and the $(H, T)_{onset}$ (AFM to FM) line represents that state of the sample where both the stable antiferromagnetic and supercooled ferromagnetic phases are possible. The supercooled ferromagnetic state is possible only during the field or temperature reduction cycles from the stable ferromagnetic state. Similarly there will be a line just below the (H^{**}, T^{**}) line (marked as $(H, T)_{onset}$ (FM to AFM)) which represents the onset of the back transformation from the ferromagnetic to antiferromagnetic phase.

Above the $(H, T)_{onset}$ (AFM to FM) line and below the (H^{**}, T^{**}) line, the conversion from antiferromagnetic to ferromagnetic phase has started and some fraction of the antiferromagnetic phase remains metastable as can be seen from the relaxation measurements in figure 6.6. For the sake of brevity, we have confined our attention only on the zero-field-cooled history of the sample where we have always approached from the low temperature antiferromagnetic state. So this region of the phase diagram is marked as metastable AFM + converted FM. The $(H, T)_{onset}$ (AFM to FM) line will coincide with the (H^{**}, T^{**}) line only in case of ideal first order transitions, which is rarely the case for real samples. During the back transformation by reducing the field or temperature, the same region would have metastable ferromagnetic phase coexisting with converted antiferromagnetic phase.

From the phase diagram shown in figure 6.8, the anomalous features in the isothermal magnetization measurements can be explained as follows. In zero field at 270 K (figure 6.3), the initial state of the sample is the stable antiferromagnetic state. During an isothermal magnetization measurement, the sample follows the path 1 shown in figure 6.8. When the field is reduced back to zero, the sample crosses the limit of metastability for the ferromagnetic phase and is completely converted back to single

phase antiferromagnet. This state is just the same state as the starting point of field cycle in figure 6.3, where the sample was a single phase antiferromagnet. The magnetization thus retraces the same path in subsequent field cycles as that of the virgin curve and the envelope curve overlaps the virgin curve in figure 6.3.

For the magnetization measurement shown in figure 6.4, the starting condition is completely antiferromagnetic (as the $SC\ FM$ state is not accessible for the zero-field-cooled history). The sample follows path 2 in the H - T plane during the first field increase (virgin curve). When the field is reduced back to zero, some amount of the ferromagnetic phase can be supercooled as the sample cannot cross the (H^*, T^*) line. The sample has now the stable antiferromagnetic phase coexisting along with the supercooled ferromagnetic phase. This supercooled ferromagnetic phase is then carried over in the subsequent field cycles and results in a higher magnetization compared to the virgin curve. The virgin curve thus lies outside the envelope curve and is lost for subsequent isothermal field cycles at this temperature. To get back the virgin curve, the sample has to be cooled in zero field well below (H^*, T^*) line, where it would be in stable antiferromagnetic phase, and then warmed back to the desired temperature in zero field.

At 305 K (figure 6.5), the conversion from the antiferromagnetic to ferromagnetic phase has already started and some fraction of the sample is in the superheated antiferromagnetic phase (see figure 6.6(a) and related discussion). During the isothermal field excursion, the sample follows path 3 in the $H - T$ plane. With the application of field, most of the superheated antiferromagnetic phase state gets converted to stable ferromagnetic phase and a very little portion still remains in the antiferromagnetic state (the transition is not yet complete till 5 T). On reducing the field back to zero, the stable ferromagnetic phase only gets partially converted back to the antiferromagnetic state and gives rise to a situation where a stable ferromagnetic phase is now coexisting along with a reduced amount of metastable antiferromagnetic phase

(see figure 6.6(b)). The subsequent field cycles now start with this situation as the starting condition and thus the envelope curve has a higher magnetization than the virgin curve. The virgin curve is then lost for isothermal field excursion at 305 K.

The extent of the virgin curve lying outside the envelope curve would thus depend on the initial condition of the two competing phases in the $H - T$ phase space. This can be seen from figure 6.7. As the temperature increases, the fraction of the ferromagnetic phase starts growing. At higher temperatures, the magnetization mostly arises due to the dominant ferromagnetic phase thus giving rise to a lower value of ΔM in figure 6.7.

It can thus be seen that the interesting thermomagnetic history effects can be explained suitably on the basis of a disorder broadened first order transition. Similar history effects like the virgin magnetization curve lying outside the envelope curve have been observed in case of epitaxial films of Fe-Rh grown on various substrates.⁸⁶ The history effects for those samples can also be explained if the corresponding H - T phase diagram is constructed in a similar fashion as we have described above. The above discussion does not assume any arrest of the reverse ferromagnetic to antiferromagnetic transition^{83,85,87-91} or any special nucleation dynamics related to the microscopic interaction or microstructure⁸⁶ and relies only on generic features across a disorder influenced first order transition. Our interpretation of the history effects seen in Fe-Rh shows that a thorough understanding of the $H - T$ phase diagram for a system undergoing first order magneto-structural transition is important if a proper initial state in the $H - T$ phase space has to be decided for any technological application.

6.3 Influence of history effects on the functional properties

Having explained the thermomagnetic history effects in the $\text{Fe}_{48}\text{Rh}_{52}$ alloy in terms of phase coexistence across a disorder influenced first order magneto-structural transition, we now study how these history effects have an impact on the functional properties like the giant magnetocaloric effect and giant magnetostriction. These history effects highlight the importance of understanding the general properties of a phase coexistent state if such a material is to be used for technological applications which demand repeatable behaviour. We see that if the initial state of the temperature or field cycle is beyond the limits of metastability, repeatability can be achieved irrespective of the number of cycles.

6.3.1 Magnetocaloric effect in $\text{Fe}_{48}\text{Rh}_{52}$

Magnetic refrigeration using the magnetocaloric effect (MCE) in solids has attracted attention because of its higher efficiency and for being safer for the environment in comparison to the conventional vapour compression cycle.^{30,92,93}

The *conventional* magnetocaloric effect refers to the refrigeration (cooling) achieved by an adiabatic decrease of magnetic field (known as adiabatic demagnetization). To achieve refrigeration in a sample, the magnetic field is first applied *isothermally* to align the magnetic moments in the direction of the field. This reduces the entropy of the spin degree of freedom. The sample (or the working material) is then isolated thermally from the surroundings to create an adiabatic environment. The field is then reduced back to zero. This removal of field misaligns the magnetic moments and the spin entropy increases. However, in an adiabatic process the entropy is conserved and the increase in spin entropy is compensated by the decrease in the lattice entropy. This leads to a drop in temperature of the lattice and thus the working material. The

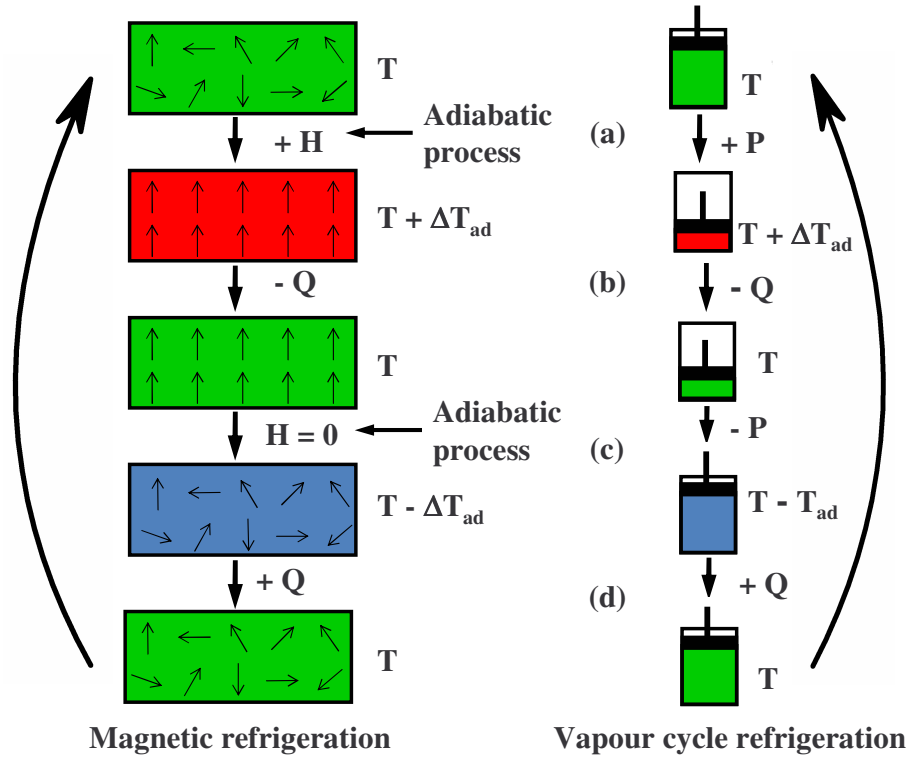


Figure 6.9: Schematic of magnetic refrigeration based on the magnetocaloric effect and a comparison with the conventional vapour compression cycle. Reproduced from http://en.wikipedia.org/wiki/Magnetic_refrigeration

schematic of the field temperature cycle to achieve refrigeration with a comparison to the vapour compression cycle is shown in figure 6.9. In this schematic, a refrigeration cycle based on only the adiabatic (instead of isothermal) application of field and the adiabatic demagnetization (leading to refrigeration) are shown for presenting an analogy with the vapour compression cycle.

Materials which show a large MCE near room temperature are of particular interest for commercial refrigeration.^{92,93} Quite a few materials are now identified which show a large MCE at or near room temperature.^{93–96} The common underlying cause of a large MCE in all these materials is thought to be a first order magneto-structural phase transition. In such cases it is estimated that the change in the lattice entropy accounts for almost half of the total entropy change across the transition.⁹⁷

The Fe-Rh alloy which undergoes a magneto-structural transition is also known to exhibit a giant MCE near room temperature.²⁵ However, it was believed that the

giant MCE in Fe-Rh vanishes after the virgin cycle and does not show reproducibility.^{25,30,31,95} In the previous section we have seen that the virgin magnetization curve lying outside the envelope curve is just an outcome of a disorder influenced first order phase transition and is not limited to only the Fe-Rh alloy system. Fe-Rh indeed shows reproducible magnetic-field and temperature response if the starting point of the experimental cycle is chosen properly in the $H - T$ phase space. The reproducible response was however confined to the temperature range below 270 K, where the value of MCE is quite small and thus not of much technological importance. At temperatures above 270 K, the virgin magnetization curve is lost after the first field cycle, which was thought to be the reason of vanishing of MCE in Fe-Rh.^{25,30,31} Building on the earlier understanding of the reason behind the thermomagnetic history effects in $\text{Fe}_{48}\text{Rh}_{52}$, we now estimate the MCE in $\text{Fe}_{48}\text{Rh}_{52}$ for various such histories. We show explicitly that $\text{Fe}_{48}\text{Rh}_{52}$ can give rise to reproducible MCE around 300 K even if the virgin $M - H$ curve lies outside the envelope magnetization curve. This reproducible MCE can be achieved by a proper combination of the isothermal and adiabatic field variation cycles, which depend on the history of the sample in the $H - T$ phase space.

The magnetic entropy is estimated by using the integral Maxwell relation approximated for the $M - H$ curves measured at discrete temperature intervals:⁹⁸

$$\Delta S_m \approx \frac{1}{\Delta T} \left[\int_0^H M(T + \Delta T, H') dH' - \int_0^H M(T, H') dH' \right] \quad (6.1)$$

Thus the area under the isothermal $M - H$ curve from 0 to upper limit H (5 T in our case) at a particular temperature T can be subtracted from the area under the $M - H$ curve at a higher temperature $T + \Delta T$ to estimate the change in magnetic entropy at the temperature $(T + \Delta T/2)$. As seen from the $H - T$ phase diagram in figure 6.8, if the working temperature of $\text{Fe}_{48}\text{Rh}_{52}$ is to be confined between 280 K and 360 K, which could be of interest for magnetic refrigeration near room temperature, the virgin curve will always be outside the envelope curve (see for example figures

6.4 and 6.5). Each isothermal measurement during the field-increasing cycle thus gives two curves, the virgin curve and the envelope curve. This gives rise to four mathematical combinations for calculating the ΔS_m . These are,

- 1) area under the virgin $M - H$ curve at T to be subtracted from area under the virgin $M - H$ curve at $T + \Delta T$,
- 2) area under the virgin $M - H$ curve at T to be subtracted from area under the envelope $M - H$ curve at $T + \Delta T$,
- 3) area under the envelope $M - H$ curve at T to be subtracted from area under the virgin $M - H$ curve at $T + \Delta T$, and
- 4) area under the envelope $M - H$ curve at T to be subtracted from area under the envelope $M - H$ curve at $T + \Delta T$.

The MCE in Fe-Rh is inverse, i.e. the sample cools by the adiabatic increase of field instead of adiabatic demagnetization.²⁵ If the adiabatic field-increasing cycle is started at the zero-field point of path 3 in figure 6.8, the sample reaches at the $\mu_0 H = 5$ T point at a lower temperature (say path 2). When the field is reduced isothermally along path 2, some amount of ferromagnetic phase will remain trapped (supercooled) as discussed earlier. This means that even if the adiabatic cycle is started in the virgin state at higher temperature, the low temperature state corresponds to the envelope curve. Thus the second mathematical possibility of subtracting the area under the virgin $M - H$ curve at T from the area under the envelope curve at $T + \Delta T$ cannot be achieved physically and has to be ruled out. Also, the first possibility from the above list would be difficult to achieve physically but we still retain it for the sake of comparison.

Figure 6.10 shows the change in entropy ΔS_m as a function of T for the three possible histories listed above for a field excursion of 5 T. The variation in MCE clearly shows history dependence. Such history dependence in MCE has earlier been observed in case of $\text{Ni}_{50}\text{Mn}_{34}\text{In}_{16}$.⁹⁹ It can be clearly seen that when the difference

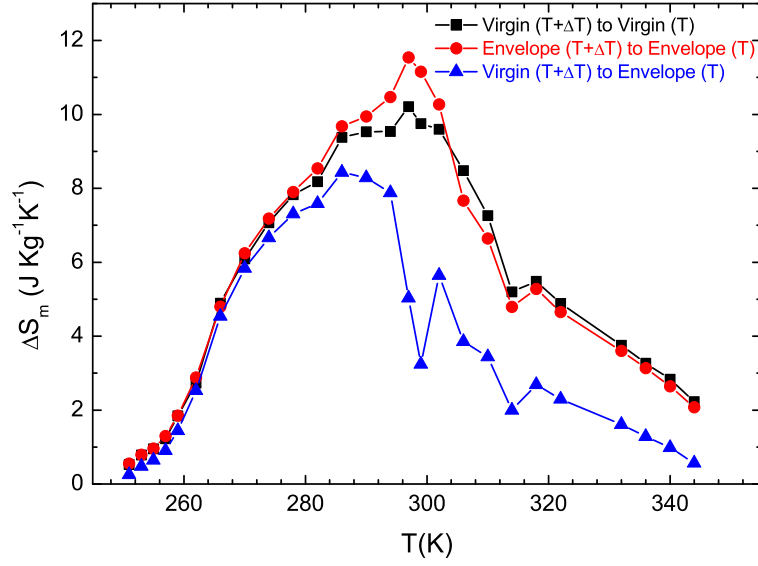


Figure 6.10: Magnetocaloric effect (change in entropy) in $\text{Fe}_{48}\text{Rh}_{52}$ as a function of temperature for a maximum field excursion of $\mu_0 H = 5\text{T}$. The change in entropy is calculated for three possible histories of the sample. See text for details.

between the areas of a) the virgin curve at higher temperature and b) the envelope curve at lower temperature is taken, the MCE reduces drastically compared to the differences in areas of the virgin curves at the same temperatures. This is exactly what was noted by Annaorazov et al.²⁵ and has later been accepted generally. Annaorazov et al. had to cool their sample below 270 K and come back to the working temperature to achieve a the same value of magnetocaloric effect, which they had interpreted as a vanishing of the magnetocaloric effect. We however see that if the difference of areas between two envelope curves is taken, the MCE actually increases marginally compared to the virgin cycle. Thus for a refrigeration cycle using $\text{Fe}_{48}\text{Rh}_{52}$, the first field-increasing and decreasing cycle at higher temperature needs to be isothermal. The adiabatic field-increasing cycle can then be carried out during the second field increase to achieve a high entropy change. The other advantage of using the second field cycle for magnetic cooling is that the hysteresis loss is reduced compared to the loss on the virgin cycle. This can be seen from figure 1, where the envelope curve encloses a smaller area compared to the virgin curve.

If the envelope curve is used for magnetic cooling, the refrigerant capacity of our $\text{Fe}_{48}\text{Rh}_{52}$ alloy is estimated to be 378.62 J kg^{-1} by using the method given by Pecharsky et al.¹⁰⁰ with $T_{hot} = 311.8 \text{ K}$ and $T_{cold} = 268.6 \text{ K}$. The T_{hot} and T_{cold} are taken to be those temperatures where ΔS_m is half of the peak value of ΔS_m on the envelope curve in figure 6.10. The average hysteresis loss in the temperature range between T_{hot} and T_{cold} on the envelope curve is 54.2 J kg^{-1} . If the hysteresis loss is subtracted from the refrigerant capacity, the R_{eff} turns out to be 324.42 J kg^{-1} which is larger than that of $\text{Gd}_5\text{Si}_2\text{Ge}_2$ and quite comparable to that of Fe doped $\text{Gd}_5\text{Si}_2\text{Ge}_2$.¹⁰¹ Furthermore, the advantage of $\text{Fe}_{48}\text{Rh}_{52}$ is that the working temperature is around 300K which is important if this system is to be used for magnetic refrigeration near room temperature. Schemes for cooling cycle¹⁰² and heat-pump cycles¹⁰³ using the Fe-Rh alloy have been proposed recently. Our study on the history dependence of MCE in $\text{Fe}_{48}\text{Rh}_{52}$ could be used to suitably modify the isothermal and adiabatic cycles for magnetic refrigeration.

By studying the history dependence of the magnetocaloric effect in the giant magnetocaloric $\text{Fe}_{48}\text{Rh}_{52}$ alloy, we have solved a long standing problem of the vanishing MCE in this material. The history dependence in magnetization is explained in terms of generic features observed across a first order transition like phase-coexistence and metastability, without considering any microscopic interaction specific to $\text{Fe}_{48}\text{Rh}_{52}$. Contrary to the long held belief, the magnetocaloric effect in the Fe-Rh alloy system does not vanish if the field-temperature history of the sample is chosen properly. Reproducibility in magnetocaloric effect can be achieved if the envelope curve is used instead of the virgin curve for magnetic cooling.

6.3.2 Large refrigerant capacity in $\text{Fe}_{0.975}\text{Ni}_{0.025}\text{Rh}$

Having established the dependence of MCE on the thermomagnetic history followed to reach the starting point of a refrigeration cycle, we now see if the working temperature

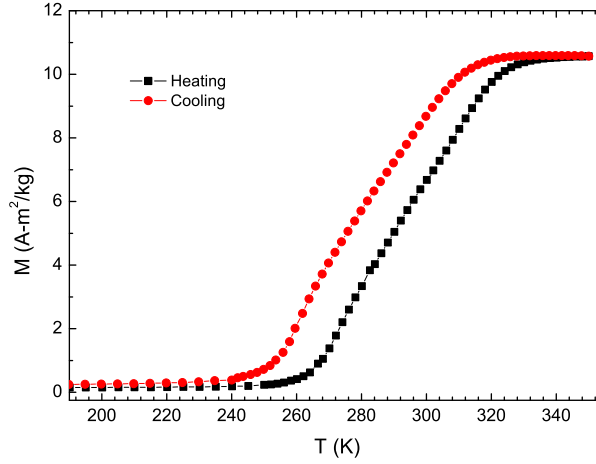


Figure 6.11: Magnetization of $\text{Fe}_{0.975}\text{Ni}_{0.025}\text{Rh}$ as a function of temperature in a magnetic field of 10 mT.

range can be tuned by appropriate substitution of the elements. It is known that addition of small amount of Ni leads to the lowering of the antiferromagnetic to ferromagnetic transition temperature.²¹

This tunability of the first order transition makes this alloy system an interesting candidate for room temperature refrigeration. In this section, we present the results of MCE measurements on $\text{Fe}_{0.975}\text{Ni}_{0.025}\text{Rh}$ by using isothermal field-dependent magnetization in two protocols and also temperature-dependent magnetization in constant magnetic fields and compare all these three methods. The importance of choosing the starting point of the magnetization cycle by taking into account the thermomagnetic history effects has recently been addressed in a few other systems,¹⁰⁴ where the earlier reports had grossly overestimated the MCE. These case studies¹⁰⁴ and our work discussed above highlight that the MCE can be either overestimated or underestimated if the thermomagnetic history effects are not taken into account during the calculation of MCE. A similar effect was seen in case of Ni-Mn-In alloy where the refrigerant capacity depends on the protocol chosen to reach the starting point of the field-temperature cycle.⁹⁹

Figure 6.11 shows the $M - T$ curve in an applied field of $\mu_0 H = 0.01$ T. The sample was first cooled down to 4.2 K in zero field and the field was applied after-

wards. The measurement was done during warming the sample up to 350 K. For brevity, only the region near the phase transition is shown in figure 6.11. The onset of the antiferromagnetic to ferromagnetic transition takes place at about 260 K and proceeds over a large temperature interval of about 80 K. A large thermal hysteresis is observed across the transition while cooling, which confirms the first order nature of the transition. The quasi-continuous transition also enables to estimate the MCE using the Maxwell's thermodynamic relation without the complications of handling the mathematical discontinuities during differentiation.¹⁰⁴

The Maxwell relation to estimate the change in entropy is given by:

$$\Delta S_m = \int_0^H \left(\frac{\partial M}{\partial T} \right)_{H'} dH', \quad (6.2)$$

which, for isothermal magnetization measurements at discrete temperatures can be expressed as equation 6.1. We first use equation 6.1 to estimate the change in entropy from isothermal $M - H$ measurements. ΔT in our case is 1 K. Figure 6.12 shows two representative isothermal $M - H$ curves at $T = 250$ K and $T = 270$ K. For all the $M - H$ measurements, the sample was first cooled in zero field down to a temperature well below 150 K where the sample is completely in the antiferromagnetic state (see figure 6.11). The temperature was then increased unidirectionally till the desired value in zero field. The onset of the antiferromagnetic to ferromagnetic metamagnetic transition at 250 K takes place at about $\mu_0 H = 1.5$ T. A large hysteresis is observed during the field-decreasing cycle which indicates that the ferromagnetic phase can be supercooled.¹⁰⁵ As we have seen in the earlier section on thermomagnetic history effects, the supercooled ferromagnetic phase persists even when the field is reduced to zero and thus the final state of the first field cycle is no longer the same as the initial antiferromagnetic state. During the second field increase (the envelope curve), the persisting ferromagnetic phase gives a higher value of magnetization compared to the virgin state as we have seen earlier in the case of the parent Fe-Rh alloy. Subsequent

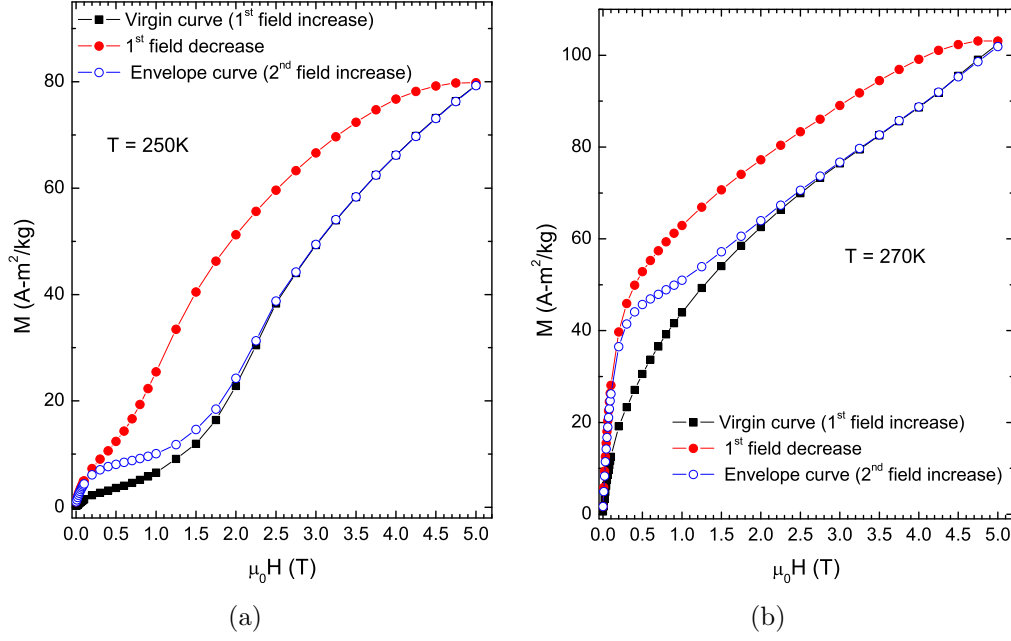


Figure 6.12: Magnetization of $\text{Fe}_{0.975}\text{Ni}_{0.025}\text{Rh}$ as a function of field at (a) 250 K and (b) 270 K.

field cycling retraces the envelope curve and the virgin curve is lost for that particular isothermal $M - H$ curve.

Figure 6.12(b) shows the $M - H$ curve at $T = 270$ K, where the conversion from the antiferromagnetic to ferromagnetic phase has already started. At 270 K the sample is in the phase coexistent state even at zero field (see figure 6.11). Thus the initial condition is quite different as compared to that of the $M - H$ curve at 250 K. Once again during the field decreasing curve, some portion of the ferromagnetic phase remains supercooled till $\mu_0 H = 0$ and gives a higher magnetization on the envelope curve. Thus all the isothermal $M - H$ measurements in the temperature regime covering the range from just below the antiferromagnetic to ferromagnetic transition till the completion of the transition, give rise to two different sets of field-increasing curves. This leads to four possibilities of using the $M - H$ curves for estimating the entropy change as we discussed earlier. We had shown earlier that the envelope curves are more suitable for the estimation of MCE as the virgin curve is lost after the first field cycle.

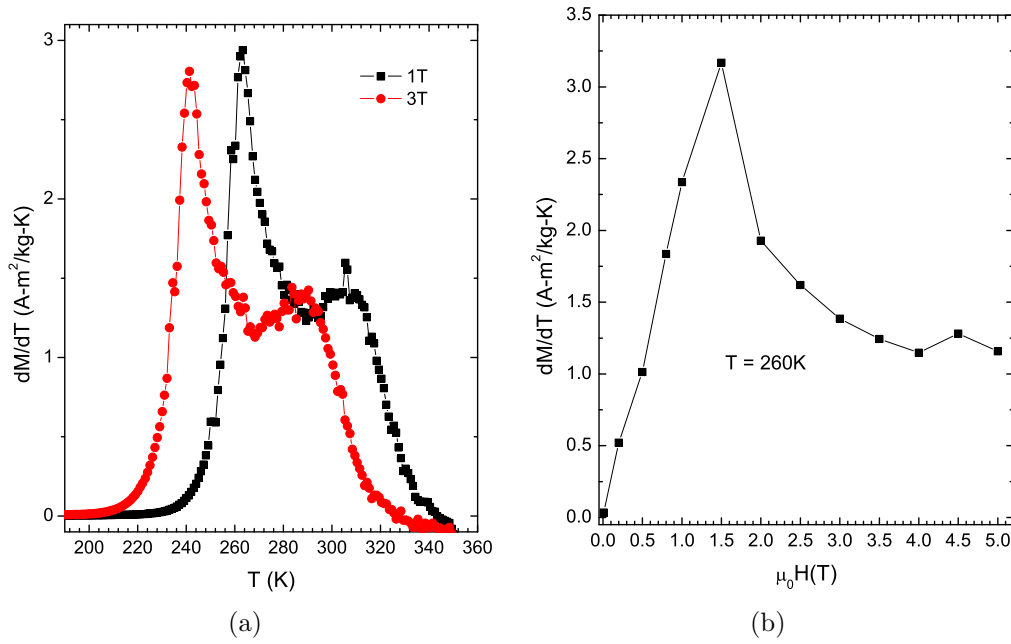


Figure 6.13: (a) Derivative of magnetization of $\text{Fe}_{0.975}\text{Ni}_{0.025}\text{Rh}$ with respect to temperature at two representative fields $\mu_0 H = 1\text{T}$ and 3T . (b) Plot of derivative of magnetization with respect to temperature at $T = 260\text{K}$ as a function magnetic field.

Another method to estimate the MCE is to use equation 6.2 directly by measuring temperature dependent magnetization in various fields. In this method, the derivatives of magnetization with respect to temperature at various fields are calculated first. Figure 6.13(a) shows the plots of derivatives of magnetization with respect to temperature at two representative field values. The values of the derivatives ($\partial M/\partial T$) at a particular temperature are then plotted as a function of magnetic field. Figure 6.13(b) shows one such representative curve at 260 K. The area under the curve of the $\partial M/\partial T$ as a function of H , thus gives the entropy change as described in equation 6.2. It should be noted here that the $M - T$ curves which are used for the estimation of MCE are the warming curves which start from the lowest temperature where the sample is in the stable antiferromagnetic state. Thus the estimated values of MCE using this method can differ from the values estimated from the isothermal $M - H$ curves, where at some temperatures the starting point of the field cycle is the phase coexistent state.

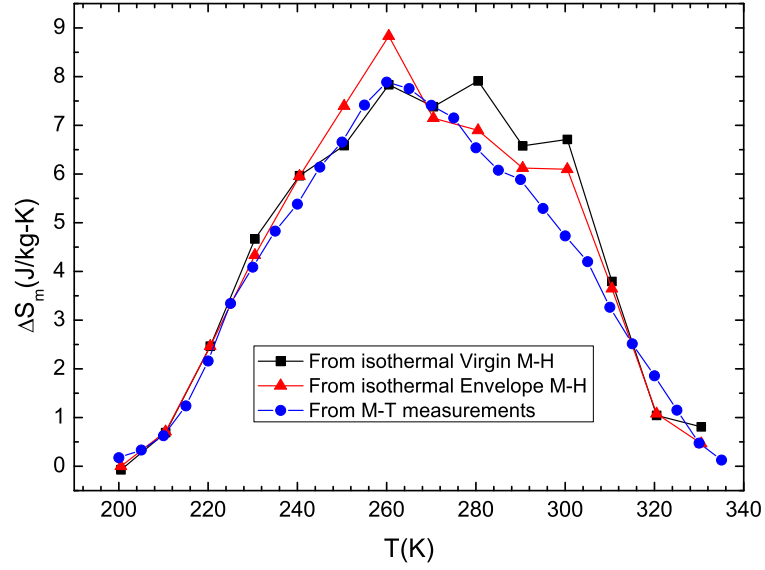


Figure 6.14: The magnetocaloric effect in $\text{Fe}_{0.975}\text{Ni}_{0.025}\text{Rh}$ as a function of temperature for a field excursion of $\mu_0 H = 5T$, estimated from isothermal $M - H$ and constant field $M - T$ curves. See text for details.

Figure 6.14 shows the MCE as a function of temperature for a field excursion of $\mu_0 H = 5 \text{ T}$ calculated by using both the $M - T$ as well as the $M - H$ measurements. As discussed earlier, four different mathematical possibilities exist for the estimation of MCE using the $M - H$ curves, out of which only two are physically possible. One of the physically possible field cycles to achieve cooling, where the virgin curve at $T + \Delta T$ and the envelope curve at T are used, appears to drastically reduce the MCE (see figure 6.10). Therefore, this possibility is not considered in figure 6.14. However, one mathematical possibility, i.e. the use of virgin $M - H$ curves at both $T + \Delta T$ and T is considered along with one physically possible cycle of using the envelope $M - H$ curves at both $T + \Delta T$ and T . The MCE estimated in two different protocols by using the $M - H$ curves is compared with the MCE estimated from $M - T$ measurements. The MCE is slightly overestimated when isothermal $M - H$ curves are used for calculation, but does not differ drastically with the value calculated from $M - T$ curves. Also it should be noted that there is no counterpart of the envelope $M - H$ curve in the $M - T$ measurements as these two are done under entirely different thermomagnetic histories. As we had argued in the earlier discussion, the envelope curve is the most

Table 6.1: Refrigerant capacities of Fe-Rh based alloys for a field excursion of 5 T.

Material	Method of estimation	T_{hot} (K)	T_{cold} (K)	R_C (J kg ⁻¹)	R_{eff} (J kg ⁻¹)
Fe ₄₈ Rh ₅₂	$M_{env}(H)$	311.8	268.6	378.62	324.42
Fe _{0.975} Ni _{0.025} Rh	$M_{env}(H)$	307.1	230.5	542.95	492.8
Fe _{0.975} Ni _{0.025} Rh	$M(T)$	305.7	229	473.41	—

suitable for achieving a reproducible refrigeration cycle. It also yields the maximum MCE out of the three different methods of estimation.

The refrigerant capacity can be calculated by taking the full width at half maximum of the $\Delta S_m(T)$ curve following the method by Pecharsky et al.¹⁰⁰ The comparison of the refrigerant capacity for the parent Fe-Rh and Fe_{0.975}Ni_{0.025}Rh for a field excursion of $\mu_0 H = 5$ T is shown in table 6.1. The refrigerant capacity estimated from the virgin curve is about 510.45 J kg⁻¹, with the hot end at about 309.8 K and the cold end at about 227.2 K. However, the virgin cycle cannot be used for practical purpose and we have not included it for the sake of comparison in the table. As we can see from the $M - H$ curves in figure 6.12, the hysteresis is smaller when the envelope curves are considered. The average hysteresis loss on the envelope curves in the working temperature range is about 50.15 J kg⁻¹ which gives an effective refrigerant capacity of 492.8 J kg⁻¹ for a field excursion of 5 T. For comparison, we consider the refrigerant capacities of two well known systems which show a large MCE near room temperature, namely Gd₅Ge_{1.9}Si₂Fe_{0.1} and MnFeP_{0.45}As_{0.55}. The effective refrigerant capacity estimated by following the same method¹⁰⁰ in case of Gd₅Ge_{1.9}Si₂Fe_{0.1} is 355 J kg⁻¹ for a field excursion of 5 T.¹⁰¹ The refrigerant capacity in case of MnFeP_{0.45}As_{0.55} is about 390 to 400 J kg⁻¹ for a field excursion of 5 T.⁹⁴ However, the hysteresis losses are not reported in case of MnFeP_{0.45}As_{0.55} and the effective refrigeration capacity would be lesser than this value. The effective refrigerant

capacity in the parent Fe-Rh alloy from our earlier work is about 324.4 J kg^{-1} . Thus Ni doping seems to provide a considerable improvement in terms of the refrigerant capacity of the Fe-Rh based alloy system.

One of the possible reasons for the increase in the refrigerant capacity of Fe-Rh by the addition of Ni, is the influence of disorder on the width of the first order transition. It was shown that quenched disorder can round-off the discontinuity across an ideal first order transition, resulting in a broad transformation regime.⁴ It appears that small amount of Ni adds to significant amount of disorder in the alloy composition, giving rise to a broader transition compared to that of the parent alloy. In case of the parent Fe-Rh alloy prepared under identical conditions of melting and subsequent heat treatment used for the present sample, the onset of the antiferromagnetic to ferromagnetic transition takes place at nearly 300 K and is completed by about 360 K (see figure 6.1). In case of the Ni doped sample, the onset of the antiferromagnetic to ferromagnetic transition takes place at nearly 260 K and gets completed at about 340 K (the closure of hysteresis on heating, see figure 6.11). This extra 20 K width of the transition results in a large gain in the refrigerant capacity, even though the peak value of the MCE is slightly reduced compared to the parent alloy (see figure 6.10). It is also interesting to see that Ni substitution does not merely add disorder to the parent alloy but also influences the electronic structure, thereby changing the onset of the antiferromagnetic to ferromagnetic transition temperature. Thus Ni substitution provides a method of not only tuning the working temperature range, but also the width of the transition which in turn results in a large refrigerant capacity. Similar effects have been observed in case of Fe substitution in $\text{Gd}_5\text{Ge}_2\text{Si}_2$.¹⁰¹

6.3.3 Thermomagnetic history effects in giant

magnetostriction of $\text{Fe}_{0.955}\text{Ni}_{0.045}\text{Rh}$

In this section we explore yet another functional property in a Fe-Rh based alloy, which is the giant magnetostriction. Magnetostrictive materials are a class of smart materials that can convert the magnetic energy to elastic energy and vice versa.¹⁰⁶ This useful property of such materials finds application in many diverse areas like linear and rotational motion control,^{107,108} sonar transducers,¹⁰⁸ tuning of superconducting radio frequency cavities¹⁰⁹ etc. Most of these applications are based on the *conventional* phenomenon of ferromagnetic domain alignment with the application of magnetic field that leads to a volume change (see figure 6.15). Some of the ferromagnetic shape memory alloys, which undergo an austenite to martensite transition also show a very large linear striction of the order of 9.5% which is due to the rearrangements of crystallographic variants in the martensitic phase by the application of magnetic field.¹¹⁰ The coupling of magnetic and elastic degrees of freedom, which is the basic requirement for magnetostriction, opens up a possibility of observing field and temperature induced strain across first order magneto-structural transition where large volume changes in the lattice are accompanied with a change in magnetic structure. Thus the study of magnetostriction in Fe-Rh alloy could be particularly interesting. In the previous chapter we have seen a large strain across the temperature driven transition in $\text{Fe}_{0.955}\text{Ni}_{0.045}\text{Rh}$. The history effects for multiple temperature cycling inside the hysteretic region were modeled by correlating the Preisach model of hysteresis with the framework of disorder influenced first order transition.

Earlier in this chapter we have seen the history effects in magnetization when the first order transition is driven by two thermodynamic variables like temperature and magnetic field. Here we show similar thermomagnetic history effects in the giant magnetostriction, which could provide important information related to the technological application of such materials. Figure 6.16 shows the linear strain in $\text{Fe}_{0.955}\text{Ni}_{0.045}\text{Rh}$ as

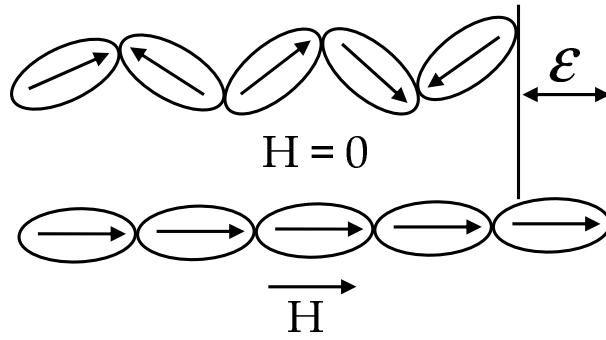


Figure 6.15: Schematic of the conventional magnetostriction.

a function of temperature in the presence of different values of applied magnetic field. The transition temperature shifts to lower values by the application of field. This indicates a possibility of a field-induced transition at constant temperature. Figure 6.17 shows the strain as a function of magnetic field at 170 K, where the sample is in the stable antiferromagnetic phase at zero field (see figure 5.1). The temperature was approached by first cooling down the sample in zero field to well below 100 K and then by heating unidirectionally till 170 K. Here the strain is defined with respect to the value of length in zero field at the temperature of measurement. An abrupt increase in strain is seen at around $\mu_0 H = 2$ T which marks the onset of a field induced transition.

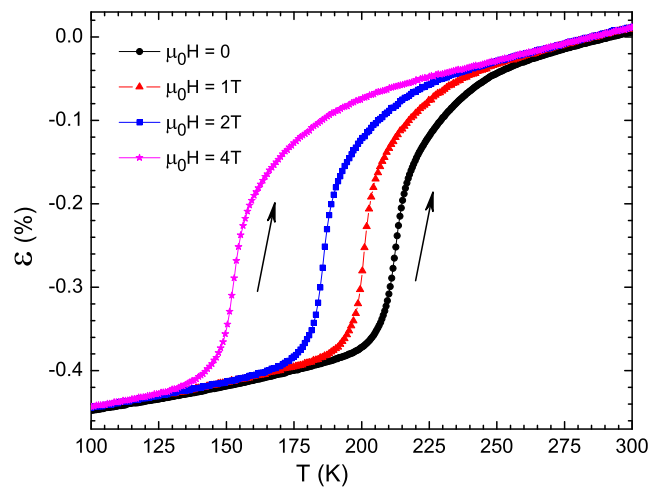


Figure 6.16: Linear strain in $\text{Fe}_{0.955}\text{Ni}_{0.045}\text{Rh}$ as a function of temperature in different values of applied magnetic field.

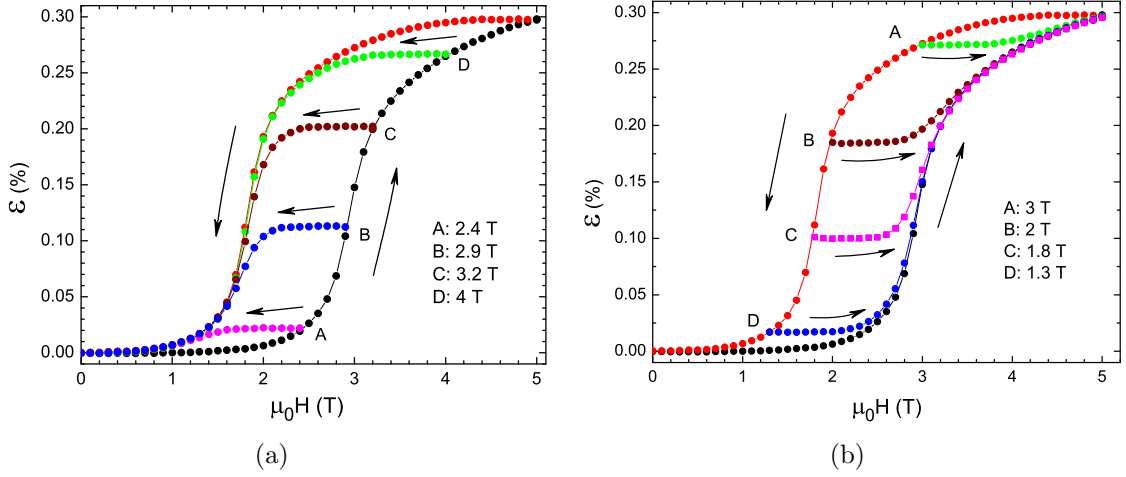


Figure 6.17: Strain as a function of magnetic field in $\text{Fe}_{0.955}\text{Ni}_{0.045}\text{Rh}$ at 170 K. (a) Minor hysteresis loops initiated on the field increasing cycle and (b) Minor hysteresis loops initiated on the field decreasing cycle.

The transition is quite broad and is not completed till the maximum field limit of our apparatus (5 T). A giant magnetostriction of about 0.3% is seen at 170 K. The MHLs during both the field increasing and decreasing cycle once again indicate the presence of phase coexistence across the transition. The transition is reversible and the strain is completely recovered when the field is reduced back to zero.

Figure 6.18 shows strain as a function of field at 200 K and 240 K. For both these measurements, the same protocol of reaching the desired temperature explained for figure 6.17 was followed. In both these measurements we see that the strain is only recovered partially on the field decreasing cycle. The subsequent measurements lead to only a smaller change in the strain compared to the first field increasing cycle. The first field increasing cycle or the virgin curve is lost for that particular temperature of measurement. To recover back the virgin curve, the sample has to be cooled well below 170 K in zero field and then heated back to the desired temperature. We have discussed similar thermomagnetic history effects in magnetization measurements on the parent Fe-Rh alloy in the earlier part of the chapter.

These thermo-magnetic history effects can be understood by using the $H - T$ phase diagram shown in figure 6.19 which is quite similar to figure 6.8. This diagram

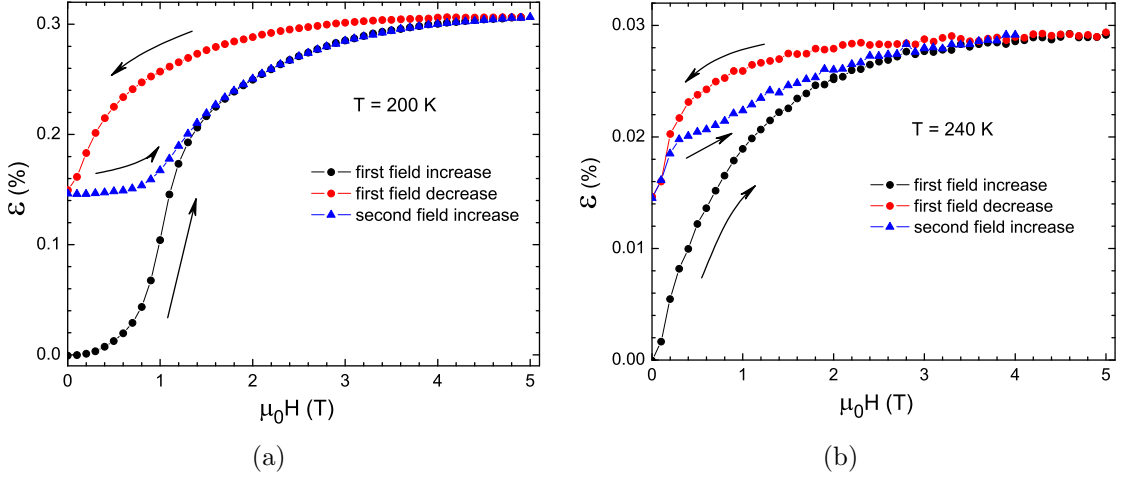


Figure 6.18: Strain in $\text{Fe}_{0.955}\text{Ni}_{0.045}\text{Rh}$ as a function of field at (a) $T = 200\text{K}$ and (b) $T = 240\text{K}$.

is constructed by measuring the values of the four onset temperatures (described in the earlier chapter) during $\varepsilon(T)$ measurements in various fields. The same notation of (H^*, T^*) , $(H, T)_{\text{onset}}(\text{AFM to FM})$, $(H, T)_{\text{onset}}(\text{FM to AFM})$ and (H^{**}, T^{**}) is used here as well.

The isothermal measurements in figures 6.17 and 6.18 are shown as vertical lines 1, 2 and 3 in this diagram. The isothermal path at 170 K starts from a stable antiferromagnetic phase and returns back to the same stable state. Thus the strain is completely recovered in that isothermal measurement cycle. The isothermal path at 200 K starts just at the onset of the antiferromagnetic to ferromagnetic transition in zero field and thus almost entire sample is in the stable antiferromagnetic phase in zero-field. However, during the field decreasing cycle, the sample does not transform completely back to the antiferromagnetic phase as it does not cross the (H^*, T^*) line. Some portion of supercooled ferromagnetic phase still persists, which leads to a higher value of strain at zero field. The subsequent field increase starts from this higher value of strain due to the phase coexistence of stable antiferromagnetic and unconverted ferromagnetic phase. This leads to the virgin cycle getting lost after the first field decrease. At 240 K in zero field, the conversion from the antiferromagnetic

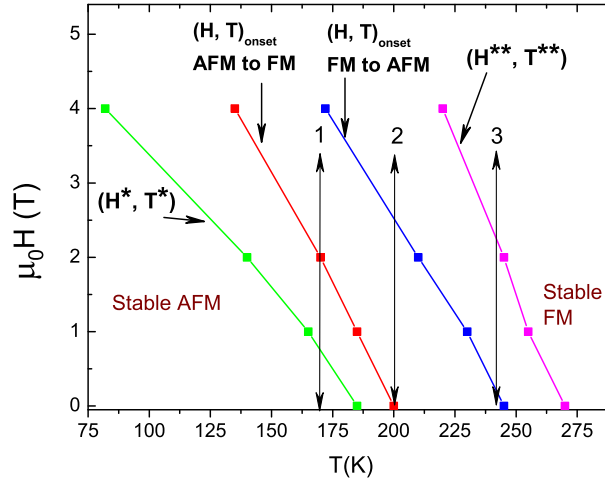


Figure 6.19: Field-temperature phase diagram of $\text{Fe}_{0.955}\text{Ni}_{0.045}\text{Rh}$ constructed from strain measurements in different fields. The vertical arrows represent the isothermal measurements shown in figures 6.17 and 6.18.

to ferromagnetic phase has already started. The starting point of the isothermal cycle is itself not a stable single phase state. On the return path, only a small amount of the ferromagnetic phase gets converted to antiferromagnetic phase and the sample does not return back to its initial condition. These thermomagnetic history effects, which arise due to the influence of disorder on the first order transition, thus govern the functional use of the material. A proper path in the $H - T$ phase space needs to be chosen to reach a proper initial condition so as to get the desired value of the output parameter.

6.4 Summary

The thermomagnetic history effects discussed in this chapter highlight the importance of understanding the influence of disorder on first order transitions. The study of the history effects in magnetization enabled us not only to solve a long standing problem of the vanishing magnetocaloric effect in Fe-Rh alloy, but also allowed us to propose a proper path to be followed in the field-temperature phase space to reach the initial condition of a reproducible refrigeration cycle. This discussion was

shown to be applicable for any material which undergoes a first order transition as a function of temperature and magnetic field as we did not consider any microscopic interaction specific to only Fe-Rh alloy. The tunability of the magnetocaloric effect was also shown by adding small amounts of Ni in the parent alloy. A large effective refrigerant capacity at room temperature, which is probably one of the largest achieved so far in this temperature range, was observed and the role of disorder was discussed in this connection. Interesting history effects were also observed in the giant magnetostriction which are quite similar to those observed in magnetization. Understanding these history effects should enable us to predict the behaviour of materials undergoing multiple field-temperature cycles, which is necessary for any technological application. We believe that our studies presented here will provide information which will be useful in tuning the functionalities of materials undergoing first order phase transitions.

Publications based on this chapter

- 1) Thermomagnetic history effects across the first order magneto-structural transition in the giant magnetocaloric Fe-Rh alloy
M. Manekar and S. B. Roy, Eur. J. Phys. B **64**, 19 (2008).
- 2) Reproducible room temperature giant magnetocaloric effect in Fe-Rh
M. Manekar and S. B. Roy, J. Phys. D: Appl. Phys. **41**, 192004 (2008).
- 3) Very large refrigerant capacity at room temperature with reproducible magnetocaloric effect in $\text{Fe}_{0.975}\text{Ni}_{0.025}\text{Rh}$
M. Manekar and S. B. Roy, J. Phys. D: Appl. Phys. **44**, 242001 (2011).
- 4) Thermo-magnetic history effects in the giant magnetostriction across the first order transition and minor hysteresis loops modeling in $\text{Fe}_{0.955}\text{Ni}_{0.045}\text{Rh}$ alloy
M. Manekar, V. K. Sharma and S. B. Roy, J. Phys.: Condens. Matter **24**, 216004 (2012).

Chapter 7

Glassy dynamics in magnetization across the first order phase transition in $\text{Fe}_{0.955}\text{Ni}_{0.045}\text{Rh}$

7.1 Introduction

In the earlier chapters we have seen the influence of disorder on the first order phase transition and how the functional properties, especially their repeatability, depend on the history effects that arise as a result of disorder. We also saw that by adding disorder one could tune the working temperature range and the width of the transition to obtain desirable properties. However, increasing the disorder may not always tune the desired properties in a monotonic manner but can lead to an entirely new phenomenon as we see in this chapter. Here we present the results of magnetization relaxation measurements across the ferromagnetic to antiferromagnetic transition in $\text{Fe}_{0.955}\text{Ni}_{0.045}\text{Rh}$. The higher concentration of Ni appears to have an effect of arresting the kinetics of the first order ferromagnetic to antiferromagnetic phase transition. This kinetic arrest of the first order phase transition gives rise to a glass-like nonequilibrium state. As we discuss in this chapter, the crossover from crystallization-like dynamics to glassy dynamics can be tracked by measuring isothermal time dependent

magnetization at various constant temperatures on the temperature decreasing cycle across this ferromagnetic to antiferromagnetic transition.

A structural glass is defined as that state of liquid where the viscosity has increased due to the slowdown of molecular motion to an extent that is beyond the laboratory time scales.¹¹¹ This phenomenon is not limited to only liquids but has also been observed in other systems like amorphous solids¹¹² and orientational glass.^{113,114} Recently a similar kinetic arrest of first order ferromagnetic to antiferromagnetic transitions in a wide variety of systems has been reported.^{47,60,85,87,89,91,115,116} This generality of the observed phenomenon in case of magnetic transitions, which is irrespective of the underlying interactions, has lead to the coining of a new term known as the magnetic-glass.^{60,115–117} This magnetic-glass has a different magnetic response as compared to the conventional reentrant spin glass.¹¹⁸

The inference of a magnetic-glass state has been based mostly on the thermomagnetic history effects across the ferromagnetic to antiferromagnetic transition, with relatively few studies^{60,115,116} highlighting the nature of time dependence of magnetization across the glassy transition. In this chapter we present the results of magnetic relaxation measurements on $\text{Fe}_{0.955}\text{Ni}_{0.045}\text{Rh}$ as the sample transforms from the ferromagnetic state to the antiferromagnetic state. We see a combination of two types of relaxation processes which can be inferred to arise from a crystallization-like dynamics (the conversion from the ferromagnetic to antiferromagnetic state) and the viscous slowdown or the kinetic arrest of the ferromagnetic to antiferromagnetic transition. We study the details of the dynamics across the first order ferromagnetic to antiferromagnetic transition to see if such crossover of relaxation processes is indeed a general phenomenon encompassing a newer kind of glassy system i.e. the magnetic-glass. The magnetic-glass state has been recently identified through its characteristic thermomagnetic irreversibility in the Pd doped Fe-Rh alloy.¹¹⁹ Here we show that Ni doping in Fe-Rh can also lead to the formation of magnetic-glass.

7.2 Thermomagnetic irreversibility in magnetization of $\text{Fe}_{0.955}\text{Ni}_{0.045}\text{Rh}$

Figure 7.1 shows magnetization as a function of temperature in an applied field of 10 mT under different thermomagnetic histories. In the zero-field-cooled (ZFC) protocol, the sample is cooled from above 300 K to the lowest temperature in zero field. The field is then switched on and magnetization is measured during warming up the sample. After reaching above 300 K, the magnetization is measured while cooling the sample unidirectionally without switching off the field. This measurement protocol is known as field-cooled-cooling (FCC). Once the lowest temperature is reached during the FCC, the sample is warmed up again in the same constant applied field. The resulting $M - T$ curve is denoted as the field-cooled-warming (FCW) curve.

The rise in magnetization at around 180 K (see inset of fig. 7.1) in the ZFC curve), marks the onset of the transition from the antiferromagnetic to the ferromagnetic phase. On cooling from above 300 K there is a marked hysteresis across the transition, which is typical of a first order transition. On further cooling down to the lowest temperature, we observe that the transition is not complete and the FCC magnetization curve does not merge with the ZFC magnetization curve (see inset of fig. 7.1). The FCC magnetization curve would have merged with the ZFC magnetization curve in the event of completion of the ferromagnetic to antiferromagnetic transition. This thermomagnetic irreversibility (TMI) gives the first indication that the kinetics of the ferromagnetic to antiferromagnetic transition are arrested.^{60,87} However, such TMI between the ZFC and FCC magnetization curves can also arise in case of a spin glass¹²⁰ and in case of systems with long range ferromagnetic order.¹²¹ The possibility of a spin glass transition or ferromagnetic impurity is ruled out in the present system in our subsequent discussion as we see the results of $M - T$ measurements in higher field. The FCW magnetization curve deviates from the FCC curve at around 75 K

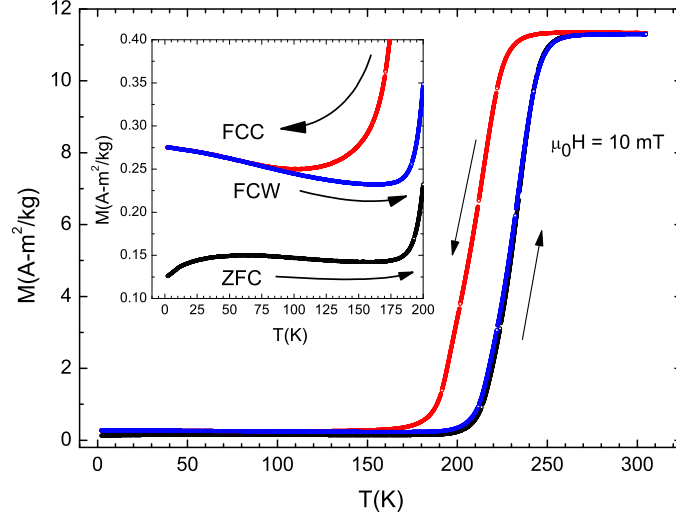


Figure 7.1: Magnetization of $\text{Fe}_{0.955}\text{Ni}_{0.045}\text{Rh}$ as a function of temperature in an applied field of 10 mT. Inset shows the thermomagnetic irreversibility on an expanded scale at lower temperatures. See text for details related to measurement protocols.

and then merges with the ZFC curve much above 225 K.

The TMI between the ZFC and FCC curves, which was visible only on an expanded scale at 10 mT, opens up with the application of higher fields as can be seen from the $M - T$ measurement presented in figure 7.2. The applied field in this case is 5 T. At intermediate values of applied field, the irreversibility between the ZFC and FCC magnetization curves increases with the increase of field. This nature of TMI is clearly opposite to the trend observed in case of spin glass¹¹⁸ and ferromagnets.¹²¹ It has been shown that such thermomagnetic history effects are the outcome of the kinetics of the first order transition getting arrested by the application of magnetic field,¹¹⁸ resulting in a magnetic-glass. The antiferromagnetic to ferromagnetic transition temperature also shifts down to lower values with the application of higher fields. Such lowering of transition temperature in Ni doped Fe-Rh with the application of field has also been observed earlier in the work of other authors as well.²¹

We now focus on the kinetics of the ferromagnetic to antiferromagnetic transition in the $\text{Fe}_{0.955}\text{Ni}_{0.045}\text{Rh}$ alloy during the FCC protocol by observing the time dependent magnetization at certain representative temperatures. The temperatures at which

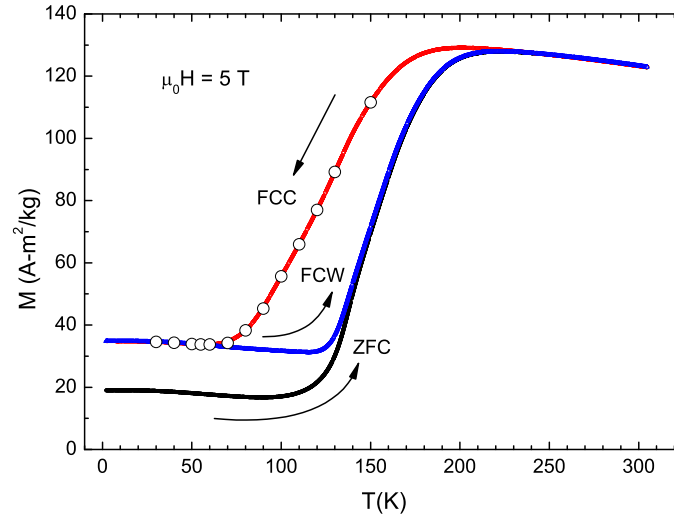


Figure 7.2: Magnetization of $\text{Fe}_{0.955}\text{Ni}_{0.045}\text{Rh}$ as a function of temperature in a magnetic field of 5 T. The open circles indicate the temperatures at which, magnetic relaxation measurements are performed during the field-cooled-cooling cycle.

these measurements are performed are indicated as open circles on the FCC curve in figure 7.2. Each of these temperatures was approached by cooling unidirectionally from 300 K in a field of 5 T. Once the target temperature was reached with minimal undershoot (about 0.4K), magnetization was measured as a function of time for a period of about 4000 sec.

7.3 Time dependence of magnetization in

$\text{Fe}_{0.955}\text{Ni}_{0.045}\text{Rh}$

Figure 7.3 shows the normalized magnetization as a function of time at two relatively high temperatures where the conversion from the ferromagnetic to antiferromagnetic phase is in the initial stages. All the measured values of magnetization are normalized with respect to the magnetization at time $t = 0$, i.e. the first measurement point after the stabilization of temperature. The normalized magnetization can be very

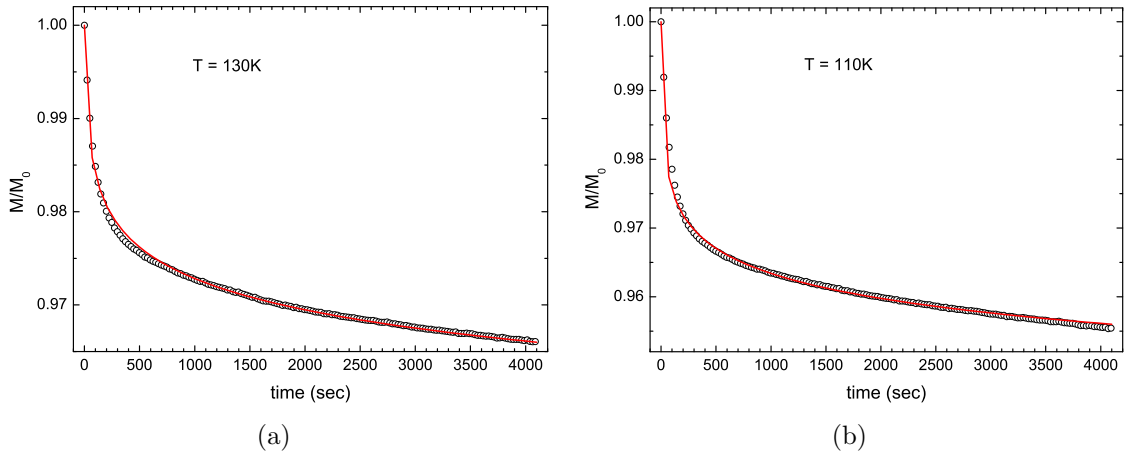


Figure 7.3: Normalized magnetization of $\text{Fe}_{0.955}\text{Ni}_{0.045}\text{Rh}$ as a function of time on the FCC cycle at (a) 130 K and (b) 110 K. The solid line is the fit to the data using equation 7.1.

well fitted with a power law given by the following equation:

$$M(t)/M_0 = -1 + 2t^\gamma. \quad (7.1)$$

The value of γ is negative when the transition takes place on the cooling cycle i.e. from the higher magnetization state to the lower magnetization state. In chapter 4, which discussed the nucleation and growth dynamics across the first order transition in Ni doped Fe-Rh, we had shown the same power law to hold true for a relaxation process when one of the phases is a ferromagnet (see equation 4.1). This power law relaxation is thus a manifestation of the metastability across a first order transition, a process similar to the crystallization of solid from melt when the melt is sufficiently undercooled.⁶⁶

On reducing the temperature further, the relaxation no longer can be explained using equation 7.1 but has to be fitted with a combination of two kinds of relaxation laws. As can be clearly seen from figure 7.4, the initial rapid decrease of magnetization within the first few seconds of measurement has now changed to a much gradual fall. This indicates a crossover from a short-time relaxation process to a long-time process. The relaxation in this intermediate temperature range, instead of a single law, can

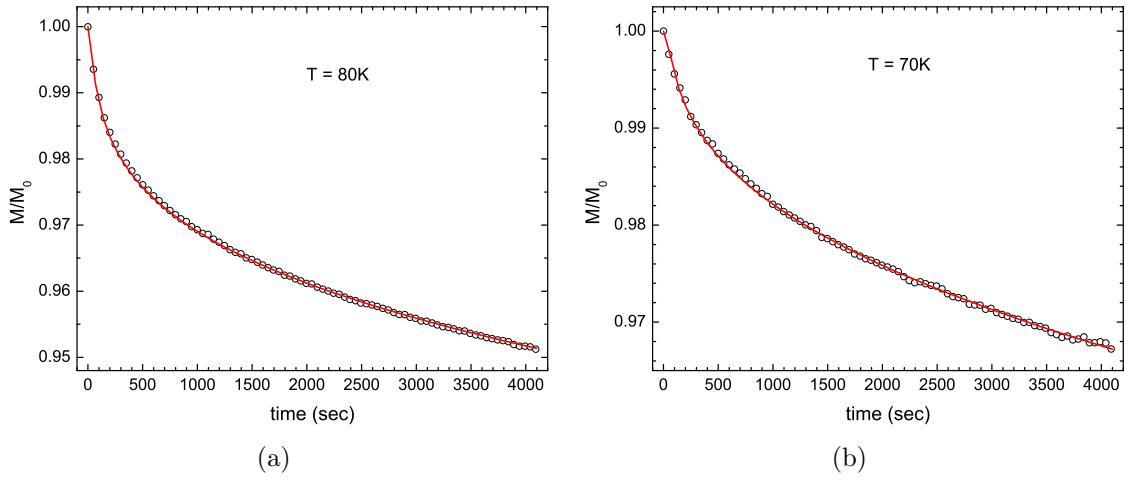


Figure 7.4: Normalized magnetization of $\text{Fe}_{0.955}\text{Ni}_{0.045}\text{Rh}$ as a function of time at a) $T = 80$ K and b) $T = 70$ K. The solid is the fit to the data using the combination of power law and stretched exponential given in equation 7.2.

be explained with a combination of the following laws:

$$M(t)/M_0 = A_1(T)(-1 + 2t^\gamma) + A_2(T)(\exp[-(t/\tau)^\beta]), \quad (7.2)$$

where β ranges from 0.6 to 0.9 and τ is the time constant of the relaxation process. At higher temperatures, β is more close to 0.6 whereas it goes near 0.9 at lower temperatures. β appears to increase with decreasing temperature but the trend does not seem to be strictly monotonic.

$A_1(T)$ and $A_2(T)$ are the temperature dependent weight factors for the power law and stretched exponential parts of equation 7.2 respectively, which give an indication of which relaxation process is dominant at a particular temperature. The stretched exponential function is a characteristic of glassy dynamics,¹¹¹ and has been used earlier for explaining the time dependence of magnetization observed during the formation of magnetic-glass in various systems like doped CeFe_2 alloys,⁶⁰ NiMnIn based off-stoichiometric Heusler alloys,¹¹⁵ and Gd_5Ge_4 .¹¹⁶ The use of the stretched exponential in equation 7.2 is justified from the nature of thermomagnetic irreversibility shown in figures 7.1 and 7.2 and the inferred glassy state during the corresponding

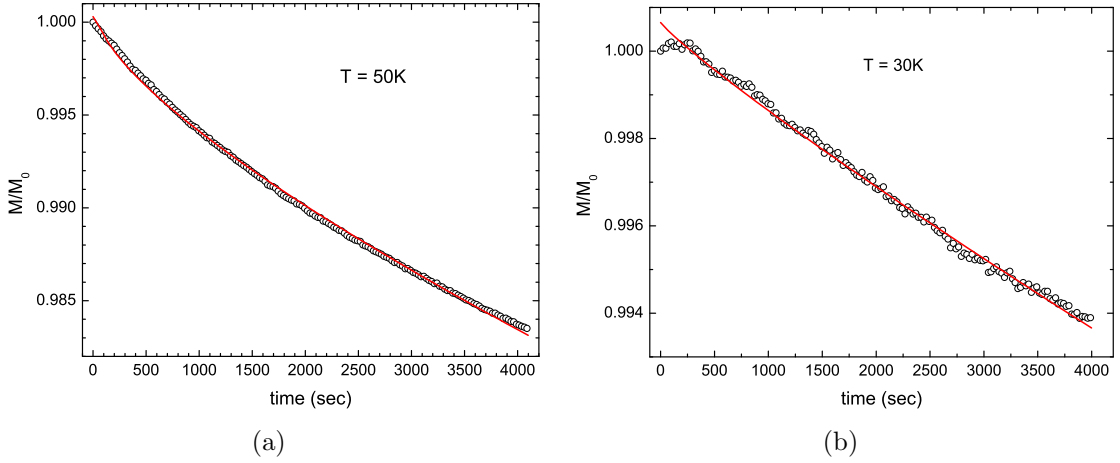


Figure 7.5: Normalized magnetization of $\text{Fe}_{0.955}\text{Ni}_{0.045}\text{Rh}$ as a function of time at a) $T = 50\text{K}$ and b) $T = 30\text{K}$. The stretched exponential term in equation 7.2 dominates over the power law, indicating a complete arrest of the phase transition.

discussion. The power law in equation 7.1 is retained in equation 7.2 as the glassy state has not completely formed as can be seen from the magnetization results presented in figure 7.2. The validity of equation 7.1 is shown theoretically for interacting ferromagnetic dots⁶⁸ and the use of stretched exponential is shown to apply for various classes of glass forming materials.¹¹¹ Such two kinds of relaxation behaviour have been observed during the simulation of nucleation and growth of solid copper from liquid.¹²² A similar crossover between two different kinds of relaxation patterns during the crystallization and glass formation process in certain organic liquids has been observed experimentally.¹²³

At further lower temperatures, the stretched exponential completely dominates over the power law indicating a complete arrest of the transition (see figure 7.5). At very low temperatures, the overall change in magnetization is quite less and is close to the noise level and drift of our magnetometer. A proper fit to the experimental data becomes quite difficult to achieve in this temperature regime. However, it is observed that the relaxation takes place over time constants (τ) well beyond the laboratory time scales, indicating the well formed glassy state.¹¹¹

7.4 Metastabilities of two kinds in $\text{Fe}_{0.955}\text{Ni}_{0.045}\text{Rh}$

Before dealing with the temperature dependence of the time constant τ in the stretched exponential of equation 7.2, we look into the temperature dependence of both the weighing factors $A_1(T)$ and $A_2(T)$ in figure 7.6. The factor A_1 is the coefficient of the power law term in equation 7.2. Thus A_1 represents that amount of the metastable phase which is not arrested or follows the normal crystallization process. Here the conversion of the ferromagnetic state to the antiferromagnetic state is taken to be analogous to the crystallization of solid from melt as discussed earlier. Similarly A_2 , which is the coefficient of the stretched exponential term, represents the fraction of the metastable state which follows glassy dynamics. In the fitting procedure of the experimental relaxation data, A_1 and A_2 are constrained by the condition $A_1 + A_2 = 1$ over the entire temperature range so that they can be related to the relative weights of the two relaxation processes across the transition. However, it should be noted that A_1 and A_2 added together do not represent the entire sample volume and thus they do not signify the individual phase fractions relative to the entire sample volume. Rather, they individually indirectly signify those fractions *within* the metastable unconverted ferromagnetic phase that follow either the crystallization-like or glassy dynamics.

A plot of A_1 and A_2 as a function of temperature in figure 7.6 thus gives a qualitative picture of how the crystalline and glassy phases evolve with temperature out of the unconverted ferromagnetic phase. It can be seen that the glassy dynamics appear just below 110 K, after a substantial amount of ferromagnetic phase has already been converted to the equilibrium antiferromagnetic state (See figure 7.2). We come back to these evolutions of A_1 and A_2 with temperature and correlate those with the dynamics within the unconverted ferromagnetic phase, during the subsequent discussion.

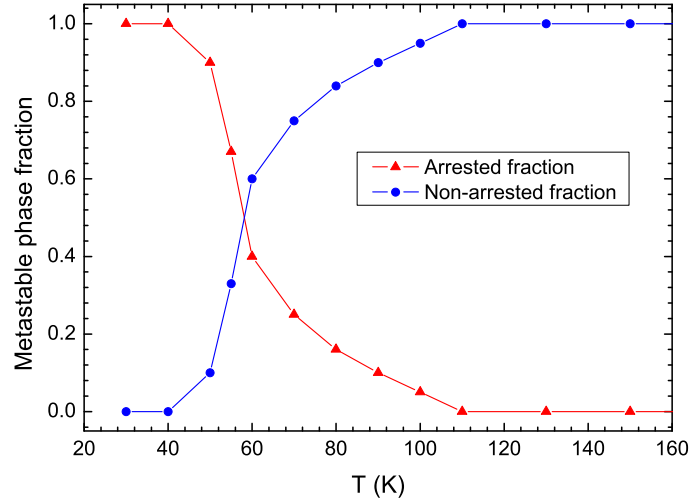


Figure 7.6: The metastable phase fraction as a function of temperature in $\text{Fe}_{0.955}\text{Ni}_{0.045}\text{Rh}$. The non-arrested fraction is the value of the weighing factor A_1 of the power law in equation 7.2. The arrested fraction is the value of A_2 which is the coefficient of the stretched exponential term in equation 7.2. See text for details.

7.5 Competition between growth and arrest in $\text{Fe}_{0.955}\text{Ni}_{0.045}\text{Rh}$

Figure 7.7 shows the temperature dependence of the absolute value of γ which is the exponent of the power law described in equation 7.1. The value of γ indicates the extent of relaxation over a certain time period. A non-monotonic behaviour of γ as a function of temperature shows a crossover from nucleation to growth of the crystalline phase as we had discussed in chapter 4. As we had argued there, the extent of relaxation increases during the initial stages of transition where the formation of newer nuclei is the dominating process. At later stages of the transition, these nuclei coalesce to form bigger clusters and the growth of the product phase now dominates over the creation of newer nuclei. This leads to a non-monotonic extent of relaxation as a function of temperature. Similar nucleation and growth dynamics is the basis of the Avrami model for crystallization of solid from melt,⁶⁶ which we discussed in chapter 4. It is interesting to note that the peak in γ occurs at nearly 80 K (see figure 7.7), till which the formation of newer nuclei of the crystallization process is still

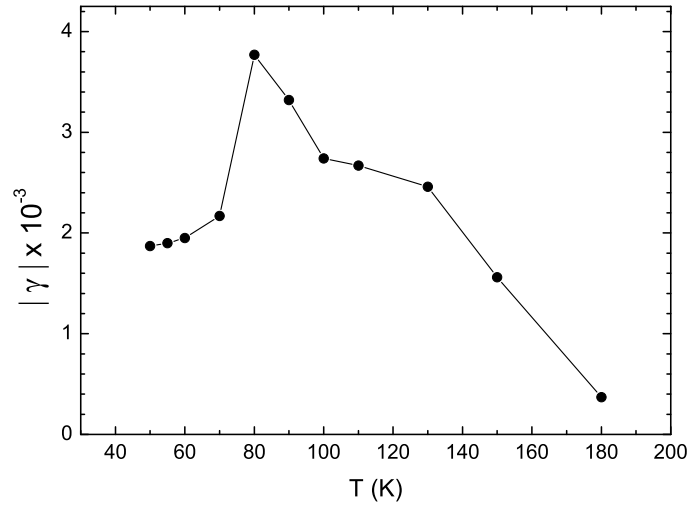


Figure 7.7: The temperature dependence of the absolute value of γ which is the exponent of power law in equation 7.1. The line is a guide to the eyes.

the dominating process during cooling. While the nucleation of the product phase is mostly dominated by the competition of the surface tension and free energy, the growth of the crystalline phase depends largely on the viscosity of the background matrix in which the nucleus has to expand.¹²⁴ Thus crystallization usually proceeds at the rate of the slowest process, nucleation or growth.¹²⁴ Therefore, the drop in the value of γ (fig. 7.7) can be taken as a crossover from nucleation to growth of the antiferromagnetic phase. At nearly similar temperatures (or slightly below), there is a substantially rapid increase of the arrested (glassy) phase within the metastable phase (see figure 7.6).

The rapid formation of the glassy phase almost coinciding with the crossover from nucleation to growth can be understood if we take into account the heterogeneous nucleation arising in a disorder influenced first order transition.⁴ The heterogeneous nucleation creates interfaces between the coexisting phases involved in the transition. The onset of kinetic arrest or glassy dynamics is linked to the decrease in mobility of these interfaces of the coexisting phases.¹²⁵ The growth also can be arrested because different mismatched crystallites come into contact with each other leading to an overall slowdown of the crystal domain growth.¹²⁴ Such a situation has indeed been

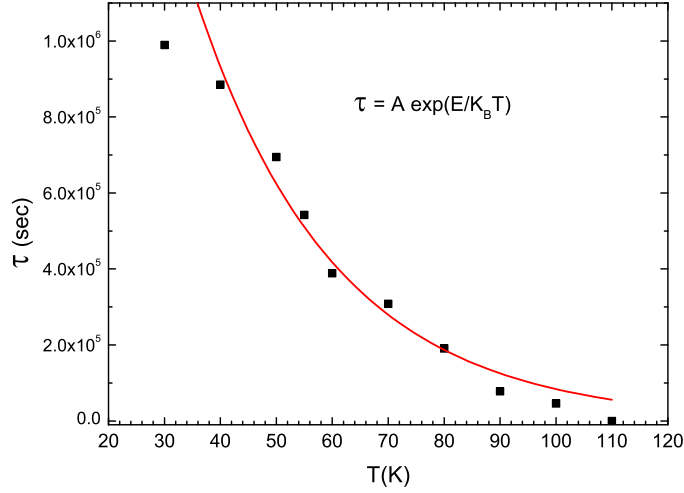


Figure 7.8: The temperature dependence of the time constant τ in the stretched exponential term of equation 7.2. The solid squares are the experimental data. The solid line is a fit to the data using equation 7.3. See text for details.

observed experimentally by local imaging using a scanning probe microscope in case of lamellar growth of crystals in a semicrystalline-amorphous polymer blend.¹²⁶ The combined results of figures 7.7 and 7.6 indicate a similar situation where the growth of the product phase actually influences the kinetic arrest of the transition itself. This observation marks a departure from the KJMA model of crystallization where it was assumed that the growth of the crystalline phase is proportional to only the *untransformed* phase and is not hindered by the previous growth. Our results show that if a substantial amount of disorder is present, it can lead to a situation where the growth of the product phase itself prohibits the further growth of the stable low temperature phase. Further experiments are now required to correlate this observation of hindered growth with the famous Kauzmann paradox (or the entropy crisis) where the system prefers to fall out of equilibrium to avoid a situation where the crystalline phase may have negative entropy at low temperatures.¹¹¹

Liquids which undergo glassy transitions are categorized as strong or fragile depending on the how the viscosity or the time constant of the stretched exponential varies with temperature.¹¹¹ With analogy to this framework, in our case the liquid state corresponds to the ferromagnetic phase.

The temperature dependence of τ follows the Arrhenius function given by:¹¹¹

$$\tau = Ae^{(E/K_BT)}, \quad (7.3)$$

where E is the activation energy and K_B is the Boltzmann constant. Figure 7.8 shows the temperature dependence of τ along with the fit to equation 7.3. The Arrhenius functionality of the time constant indicates that the ferromagnetic phase behaves as a strong glass forming liquid. This is in contrast with the case of the Ce(Fe, 4% Ru)₂ alloy that behaves as a fragile magnetic-glass former.⁶⁰

7.6 Summary

To study the effect of increasing disorder on the first order transition, we have studied the magnetic relaxation behaviour across the ferromagnetic to antiferromagnetic transition in Fe_{0.955}Ni_{0.045}Rh alloy. We see a distinct crossover from the power law corresponding to the crystallization process to the stretched exponential behaviour corresponding to glassy dynamics. The time constant of the stretched exponential follows the Arrhenius functionality which is similar to the case of strong glass forming liquids. The temperature dependence of the exponent in the power law relaxation corresponding to the crystallization process exhibits a distinct non-monotonic behaviour indicating a crossover from nucleation to growth mechanism. A substantially rapid increase of the arrested (glassy) fraction within the metastable phase almost coincides with this crossover from nucleation to growth. We conjecture that this coincidence results from the disorder influenced nature of the first order ferromagnetic to antiferromagnetic phase transition in the Fe_{0.955}Ni_{0.045}Rh alloy. The heterogeneous nucleation in such disorder influenced first order phase transition is expected to create interfaces between coexisting phases. The onset of kinetic arrest or glassy dynamics in the Fe_{0.955}Ni_{0.045}Rh alloy is possibly linked to the decrease in mobility of these inter-

faces, indicating to a situation where the growth of the product phase influences the kinetic arrest of the transition itself. This observation is a marked departure from the Avrami model of crystallization where the transformation rate is independent of the product phase. This observation could be useful for optimizing the level of disorder to be introduced to achieve the desirable functional properties.

Publications based on this chapter

- 1) Glassy dynamics in magnetization across the first order ferromagnetic to anti-ferromagnetic transition in $\text{Fe}_{0.955}\text{Ni}_{0.045}\text{Rh}$

M. Manekar, M. K. Chattopadhyay and S. B. Roy

J. Phys.: Condens. Matter **23**, 086001 (2011).

Chapter 8

Summary and future outlook

8.1 Summary

The work presented in this thesis was primarily motivated with the need to understand the unsolved problem in literature of the vanishing magnetocaloric effect in the Fe-Rh alloy system. It was known earlier that this alloy system undergoes a first order magneto-structural transition occurring as a function of temperature and magnetic field. Some of the technologically important functional properties like the giant elastocaloric effect, giant magnetostriction, giant magnetoresistance and thermally assisted magnetic recording with artificial structures based on Fe-Rh, were also known from the literature. We believed that such wide range of functionalities could possibly be governed by the underlying first order magneto-structural phase transition. Based on our earlier background knowledge in the area of disorder influenced first order transitions and the related history effects (see for example the review by Roy and Chaddah¹¹), the Fe-Rh alloy system provided a natural choice to extend these ideas and understand the core issue behind the vanishing magnetocaloric effect.

Our approach in this thesis has been to follow the thread of disorder influenced first order transitions and the associated concepts of phase coexistence and metastability. In this work, the phase coexistence and metastability across the first order transition

in the parent Fe-Rh alloy were imaged at sub-micron length scales to highlight the fact that these features are generic to any first order transition and are not limited to only manganites showing colossal magnetoresistance. The correlation between the elastic and electronic degrees of freedom, which is essential for giving rise to multi-scale phase coexistence, was explicitly imaged using magnetic force microscopy. Theoretical models originally proposed for manganites to explain phase coexistence were shown to be applicable to the Fe-Rh alloy system, highlighting the generality of this phenomenon.

The other generalization that was attempted, was to find the similarity between the nucleation and growth dynamics across a first order transition with the crystallization process of solids. We proposed a conjecture to take the area of the minor hysteresis loops across the hysteretic region as a measure of the phase fraction of the product phase during the transition. This conjecture enabled us to generalize the nucleation and growth dynamics as a function of time during the crystallization process of solids, to that of a general first order transition that is driven by temperature and magnetic field. The identification of phase fraction from bulk measurements was based on the assumption of individual pockets of the sample having their own independent hysteresis loops across the transition. This assumption was tested by modeling the minor hysteresis loops generated under multiple temperature cycling across the first order transition in one of the Fe-Rh based alloy. The Preisach model of hysteresis, which was originally proposed for explaining the hysteresis in ferromagnets, was correlated with the *landscape* picture^{9,64} of transition temperatures during a first order transition. History effects in the physical properties when the transition is driven by a single variable could be modeled reasonably well.

The history effects in Fe-Rh when the transition is driven by two variables like the temperature and magnetic field were explained within the framework of disorder influenced first order transition. It was shown that any material which undergoes

a first order transition induced by two thermodynamic variables would show similar history effects. The magnetocaloric effect was estimated by following different histories in the field-temperature phase space and it was shown that the vanishing of the magnetocaloric effect was actually a misinterpretation of the thermomagnetic history effects. A protocol was also proposed to achieve a reproducible magnetocaloric effect by approaching the initial condition of the field temperature cycle in a proper manner. We could thus solve this long-standing problem, which was the primary motivation behind this thesis. The understanding of these history effects was used to obtain a large refrigerant capacity at room temperature in a Ni doped Fe-Rh alloy, which is probably the largest in any material at this temperature. Similar thermomagnetic history effects were also observed during the magnetostriction measurements.

Different kind of thermomagnetic history effects were observed across the temperature driven transition when the amount of disorder is increased in form of higher concentration of Ni doping. The kinetics of the first order ferromagnetic to antiferromagnetic phase transition appear to be arrested in such cases. It was found that the product phase itself might influence its further growth thereby leading to the arrest of the kinetics of the first order phase transition, which is similar to a glass-like state. This result is of particular importance as it shows that mere addition of disorder may not always lead to a desirable tuning of the functional property of interest, but may actually lead to an entirely new phenomenon.

8.2 Future outlook

The utility of disorder in tuning the functional properties of materials, especially Fe-Rh based alloys, undergoing first order transition was established during the course of the work presented in this thesis. As a natural outcome of the present work, the future work would be to characterize the exact nature of this disorder and attempts to make

samples with controlled disorder. During the measurements of physical properties of these future *control* samples, some of the heuristic arguments presented in this thesis would hopefully be rigourously tested. As we had pointed out in chapter 5, the effect of disorder on the dynamics of a first order transition at different length scales can provide interesting information for achieving the desired properties from such materials. Another direction of the future experiments could be related to the understanding of the nature of microscopic interactions between the elements of solids undergoing first order magneto-structural transitions, so that newer materials can be designed with desired functionalities.

Bibliography

- [1] L. E. Reichl, *A modern course in statistical physics* (John Wiley & Sons, Inc., New York, 1998), 2nd ed. [1](#), [2](#), [7](#), [8](#)
- [2] R. M. White and T. H. Geballe, *Long range order in solids* (Academic Press, New York, 1979). [2](#), [5](#), [46](#)
- [3] V. K. Pecharsky, K. A. Gscheidner, Jr., and D. Fort, *Scr. Mater.* [35](#), [843](#) (1996). [2](#)
- [4] Y. Imry and M. Wortis, *Phys. Rev. B* [19](#), [3580](#) (1979). [3](#), [4](#), [41](#), [108](#), [125](#)
- [5] L. Landau and E. Lifshitz, *Statistical physics, Part 1*, vol. 5 of *Course of theoretical physics* (Pergamon Press, Oxford, 1980), 3rd ed. [5](#)
- [6] G. F. Mazenko, *Fluctuations, order, and defects* (John Wiley & Sons, Hoboken, N.J., 2003). [6](#)
- [7] P. M. Chaikin and T. C. Lubensky, *Principles of condensed matter physics* (Cambridge University Press, Cambridge, 1995). [7](#), [8](#), [9](#), [10](#), [12](#), [65](#), [92](#)
- [8] A. P. Levanyuk and A. S. Sigov, *Defects and structural phase transitions* (Gordan and Breach Science Publishers, New York, 1988). [10](#), [11](#)
- [9] K. H. Ahn, T. Lookman, and A. R. Bishop, *Nature* [428](#), [401](#) (2004). [11](#), [33](#), [34](#), [42](#), [43](#), [66](#), [130](#)

- [10] M. K. Chattopadhyay, S. B. Roy, A. K. Nigam, K. J. S. Sokhey, and P. Chaddah, Phys. Rev. B. **68**, 174404 (2003). 11, 12, 66, 67, 89
- [11] S. B. Roy and P. Chaddah, Phase Transitions **77**, 767 (2004). 13, 83, 129
- [12] M. E. Gruner, E. Hoffmann, and P. Entel, Phys. Rev. B. **67**, 064415 (2003). 14
- [13] J. S. Kouvel and C. C. Hartelius, J. Appl. Phys. **33 suppl.**, 1343 (1962). 14
- [14] G. Shirane, R. Nathans, and C. W. Chen, Phys. Rev. **134**, A1547 (1964). 14
- [15] V. L. Moruzzi and P. M. Marcus, Phys. Rev. B. **46**, 2864 (1992). 14
- [16] A. I. Zakharov, A. M. Kadomtseva, R. Z. Levitin, and E. G. Ponyatovskii, Sov. Phys. JETP **19**, 1348 (1964), online version not available. 14, 15, 38, 42, 66, 86
- [17] C. Kittel, Phys. Rev. **120**, 335 (1960). 15
- [18] J. B. McKinnon, D. Melville, and E. W. Lee, J. Phys. C: Solid State Phys. **3**, S46 (1970). 15
- [19] J. S. Kouvel, J. Appl. Phys. **37**, 1257 (1966). 15
- [20] C. J. Schinkel, R. Hartog, and F. Hochstenbach, J. Phys. F: Met. Phys. **4**, 1412 (1974). 15
- [21] N. V. Baranov and E. A. Barabanova, J. Alloys Compd. **219**, 139 (1995). 15, 45, 47, 102, 118
- [22] M. Lederman, G. A. Gibson, and S. Schultz, J. Appl. Phys. **73**, 6961 (1993). 15, 42
- [23] G. Ju, Phys. Rev. Lett. **93**, 197403 (2004). 15, 42
- [24] S. A. Nikitin, G. Myalikhgulyev, A. M. Tishin, M. P. Annaorazov, K. A. Asatryan, and A. L. Tyurin, Phys. Lett. A. **148**, 363 (1990). 15, 84, 85

- [25] M. P. Annaorazov, S. A. Nikitin, A. L. Tyurin, K. A. Asatryan, and A. K. Dovletov, J. Appl. Phys. **79**, 1689 (1996). 15, 16, 83, 86, 97, 98, 99, 100
- [26] S. A. Nikitin, G. Myalikhgulyev, M. P. Annaorazov, A. L. Tyurin, R. W. Myn-dyev, and S. A. Akopyan, Phys. Lett. A. **171**, 234 (1992). 15
- [27] M. R. Ibarra and P. A. Algarabel, Phys. Rev. B **50**, 4196 (1994). 15
- [28] P. A. Algarabel, M. R. Ibarra, C. Marquina, A. D. Moral, J. Galibert, M. Iqbal, and S. Askenazy, Appl. Phys. Lett. **66**, 3061 (1995). 15
- [29] J. Thiele, S. Maat, and E. E. Fullerton, Appl. Phys. Lett. **82**, 2859 (2003). 15
- [30] V. K. Pecharsky and K. A. Gschneidner, Jr., J. Magn. Magn. Mater. **200**, 44 (1999). 16, 83, 96, 98
- [31] V. K. Pecharsky and K. A. Gschneidner, Jr., Phys. Rev. Lett. **78**, 4494 (1997). 16, 83, 98
- [32] S. Yuasa, H. Miyajima, and Y. Otani, J. Phys. Soc. Jpn. **63**, 3129 (1994). 19
- [33] B. D. Cullity, *Elements of x-ray diffraction* (Addison-Wesley, Reading, Mas-sachusetts, 1978), 2nd ed. 20
- [34] L. Chen and D. W. Lynch, Phys. Rev. B. **37**, 10503 (1988). 21
- [35] Y. Leng, *Materials characterization: Introduction to microscopic and spectro-scopic methods* (John Wiley & Sons (Asia) Pte. Ltd., Singapore, 2008). 21, 22
- [36] Quantum Design Inc., *MPMS 5, Hardware and Software reference manual*, San Diego (1992). 24
- [37] A. Barone and G. Paterno, *Physics and applications of the Josephson effect* (John Wiley & Sons, New York, 1982). 23, 24

- [38] G. B. Donaldson, J. Clarke, and J. C. Macfarlane, in *Concise encyclopedia of magnetic & superconducting materials*, edited by J. Evetts (Pergamon Press, Oxford, 1992). 24
- [39] M. Mcelfresh, *Fundamentals of magnetism and magnetic measurements: Featuring Quantum Design's Magnetic Property Measurement System*, Quantum Design Inc., San Diego (1992), URL <http://www.qdusa.com/sitedocs/appNotes/mpms/FundPrimer.pdf>. 24
- [40] B. D. Cullity and C. D. Graham, *Introduction to magnetic materials* (IEEE Press, John Wiley & Sons, Hoboken, New Jersey, 2009), 2nd ed. 25, 69
- [41] Quantum Design Inc., *Vibrating sample magnetometer: Application notes*, URL http://www.qdusa.com/sitedocs/appNotes/vsmappnote_5-09.pdf. 25
- [42] V. K. Sharma, Ph.D. thesis, Homi Bhabha National Institute, Raja Ramanna Centre for Advanced Technology, Indore (2012), URL http://www.hbni.ac.in/phdthesis/thesis_aug2012/PHYS03200704003_VKSharma.pdf. 27
- [43] M. Manekar, S. B. Roy, and P. Chaddah, J. Phys.: Condens. Matter **12**, L409 (2000). 27, 46, 47, 67, 85
- [44] K. J. S. Sokhey, M. Manekar, M. K. Chattopadhyay, R. Kaul, S. B. Roy, and P. Chaddah, J. Phys. D: Appl. Phys. **36**, 1366 (2003). 27, 47, 85
- [45] M. Couach and A. F. Khoder, in *Magnetic susceptibility of superconductors and other spin systems*, edited by R. A. Hein, T. L. Francavilla, and D. H. Liebenberg (Plenum Press, New York, 1991). 27
- [46] Y. Zhu, ed., *Modern techniques for characterizing magnetic materials* (Kluwer Academic Publishers, Boston, 2005), chap. 11. 28, 30, 31

- [47] W. Wu, C. Israel, N. Hur, S. Park, S. Cheong, and A. Lozanne, Nat. Mater. **5**, 881 (2006). 30, 34, 43, 46, 116
- [48] E. Dagotto, *Nanoscale phase separation and colossal magnetoresistance: The physics of manganites and related compounds* (Springer, Berlin, 2003). 33
- [49] E. Dagotto, N. J. Phys. **7**, 67 (2005). 33
- [50] M. Uehara, S. Mori, C. H. Chen, and S.-W. Cheong, Nature **399**, 560 (1999). 33, 34, 46
- [51] S. B. Roy, G. K. Perkins, M. K. Chattopadhyay, A. K. Nigam, K. J. S. Sokhey, P. Chaddah, A. D. Caplin, and L. F. Cohen, Phys. Rev. Lett **92**, 147203 (2004). 33, 54, 66, 72
- [52] J. D. Moore, G. K. Perkins, Y. Bugoslavsky, L. F. Cohen, M. K. Chattopadhyay, S. B. Roy, P. Chaddah, K. A. Gschneidner, Jr., and V. K. Pecharsky, Phys. Rev. B. **73**, 144426 (2006). 33, 34, 54, 66, 72
- [53] V. K. Sharma, J. D. Moore, M. K. Chattopadhyay, K. Morrison, L. F. Cohen, and S. B. Roy, J. Phys.: Condens. Matter **22**, 016008 (2009). 33, 66, 72
- [54] L. Zhang, C. Israel, A. Biswas, R. L. Greene, and A. Lozanne, Science **298**, 805 (2002). 33, 34, 46
- [55] J. Burgy, A. Moreo, and E. Dagotto, Phys. Rev. Lett **92**, 097202 (2004). 33, 34, 42
- [56] Y. Murakami, J. H. Yoo, D. Shindo, T. Atou, and M. Kikuchi, Nature **423**, 965 (2003). 34, 46
- [57] C. Renner, G. Aeppli, B.-G. Kim, Y.-A. Soh, and S.-W. Cheong, Nature **416**, 518 (2002). 34, 46

- [58] S. Kartha, J. A. Krumhansl, J. P. Sethna, and L. K. Wickham, Phys. Rev. B. **52**, 803 (1995). 42
- [59] H. Seto, Y. Noda, and Y. Yamada, J. Phys. Soc. Jpn. **59**, 978 (1990). 42
- [60] M. K. Chattopadhyay, S. B. Roy, and P. Chaddah, Phys. Rev. B. **72**, 180401(R) (2005). 43, 116, 117, 121, 127
- [61] J. W. Christian, *The theory of transformations in metals and alloys* (Pergoman Press, Amsterdam, 2002), 3rd ed. 46
- [62] D. A. Porter and K. E. Easterling, *Phase transformation in metals and alloys* (Chapman & Hall, London, 1992), 2nd ed. 46
- [63] E. Zeldov, D. Majer, M. Konczykowski, V. B. Geshkenbein, V. M. Vinokur, and H. Shtrikman, Nature **375**, 373 (1995). 46
- [64] A. Soibel, E. Zeldov, M. Rappaport, Y. Myasoedov, T. Tamegai, S. Ooi, M. Konczykowski, and V. B. Geshkenbein, Nature **406**, 282 (2000). 46, 67, 130
- [65] X. Granados, J. Fontcuberta, X. Obradors, and J. B. Torrence, Phys. Rev. B **46**, 15683 (1992). 46
- [66] M. Avrami, J. Chem. Phys **7**, 1103 (1939). 47, 51, 52, 53, 58, 120, 124
- [67] S. B. Roy and P. Chaddah, Physica C **279**, 70 (1997). 47
- [68] L. C. Sampaio, R. Hyndman, F. S. de Menezes, J. P. Jamet, P. Meyer, J. Gierak, C. Chappert, V. Mathet, and J. Ferre, Phys. Rev. B. **64**, 184440 (2001). 49, 122
- [69] William. D. Callister, Jr., *Materials science and engineering: An introduction* (John Wiley & Sons, Inc., New York, 2007), 7th ed. 54

- [70] Y. Yamada, N. Hamaya, J. D. Axe, and S. M. Shapiro, Phys. Rev. Lett. **53**, 1665 (1984). 54
- [71] Y. Ivshin and T. J. Pence, Int. J. Eng. Sci. **32**, 681 (1994). 54, 55
- [72] J. Farjas and P. Roura, Acta Mater. **54**, 5573 (2006). 55
- [73] P. Krüger, J. Phys. Chem. Solids **54**, 1549 (1993). 55
- [74] A. R. Massih and L. O. Jernkvist, Modell. Simul. Mater. Sci. Eng. **17**, 055002 (2009). 55
- [75] D. C. Jiles, IEEE Trans. Magn. **28**, 2602 (1992). 57
- [76] H. Orihara, S. Hashimoto, and Y. Ishibashi, J. Phys. Soc. Jpn. **63**, 1031 (1994). 59, 61
- [77] W. Lu, N. T. Nam, and T. Suzuki, IEEE Trans. Magn. **45**, 4011 (2009). 59
- [78] I. Mayergoyz, *Mathematical models of hysteresis and their applications* (Elsevier Science, New York, 2003), 2nd ed. 64, 70, 71, 74, 78, 80
- [79] M. S. Pierce, R. G. Moore, L. B. Sorensen, S. D. Kevan, O. Hellwig, E. E. Fullerton, and J. B. Kortright, Phys. Rev. Lett. **90**, 175502 (2003). 69, 80
- [80] M. S. Pierce, C. R. Buechler, L. B. Sorensen, J. J. Turner, S. D. Kevan, E. A. Jagla, J. M. Deutsch, T. Mai, O. Narayan, J. E. Davies, et al., Phys. Rev. Lett. **94**, 017202 (2005). 69, 80
- [81] J. Ortin, J. Appl. Phys. **71**, 1454 (1992). 70, 74
- [82] Z. Bo and D. C. Lagoudas, Int. J. Eng. Sci. **37**, 1205 (1999). 79
- [83] M. Manekar, S. Chaudhary, M. K. Chattopadhyay, K. J. Singh, S. B. Roy, and P. Chaddah, J. Phys.: Condens. Matter **14**, 4477 (2002). 83, 91, 95

- [84] H. Tang, V. K. Pecharsky, K. A. Gschneidner Jr., and A. O. Pecharsky, Phys. Rev. B **69**, 064410 (2004).
- [85] R. Rawat, K. Mukherjee, K. Kumar, A. Banerjee, and P. Chaddah, J. Phys.: Condens. Matter **19**, 256211 (2007). **83**, **91**, **95**, **116**
- [86] S. Maat, J. U. Thiele, and E. E. Fullerton, Phys. Rev. B. **72**, 214432 (2005). **83**, **95**
- [87] M. A. Manekar, S. Chaudhary, M. K. Chattopadhyay, K. J. Singh, S. B. Roy, and P. Chaddah, Phys. Rev. B. **64**, 104416 (2001). **91**, **95**, **116**, **117**
- [88] M. K. Chattopadhyay, M. A. Manekar, A. O. Pecharsky, V. K. Pecharsky, K. A. Gschneidner, Jr., J. Moore, G. K. Perkins, Y. V. Bugoslavsky, S. B. Roy, P. Chaddah, et al., Phys. Rev. B. **70**, 214421 (2004). **91**
- [89] S. B. Roy and M. K. Chattopadhyay, Europhys. Lett. **79**, 47007 (2007). **91**, **116**
- [90] K. Sengupta and E. V. Sampathkumaran, Phys. Rev. B. **73**, 020406(R) (2006). **91**
- [91] K. Kumar, A. K. Pramanik, A. Banerjee, P. Chaddah, S. B. Roy, S. Park, C. L. Zhang, and S.-W. Cheong, Phys. Rev. B. **73**, 184435 (2006). **91**, **95**, **116**
- [92] V. K. Pecharsky and K. A. Gschneidner, Jr., Adv. Mater. **13**, 683 (2001). **96**, **97**
- [93] K. A. Gschneidner, Jr., V. K. Pecharsky, and A. O. Tsokol, Rep. Prog. Phys. **68**, 1479 (2005). **96**, **97**
- [94] O. Tegus, E. Bruck, K. H. J. Buschow, and F. R. de Boer, Nature **415**, 150 (2002). **107**

- [95] N. K. Sun, W. B. Cui, D. Li, D. Y. Geng, F. Yang, and Z. D. Zhang, Appl. Phys. Lett. **92**, 072504 (2008). 98
- [96] V. K. Sharma, M. K. Chattopadhyay, A. Khandelwal, and S. B. Roy, Phys. Rev. B **82**, 172411 (2010). 97
- [97] V. K. Pecharsky, A. P. Holm, K. A. Gschneidner, Jr., and R. Rink, Phys. Rev. Lett. **91**, 197204 (2003). 97
- [98] R. D. McMichael, J. J. Ritter, and R. D. Shull, J. Appl. Phys. **73**, 6946 (1993). 98
- [99] M. K. Chattopadhyay, V. K. Sharma, and S. B. Roy, Appl. Phys. Lett. **92**, 022503 (2008). 99, 102
- [100] V. K. Pecharsky and K. A. Gscheindner, Jr., J. Appl. Phys. **90**, 4614 (2001). 101, 107
- [101] V. Provenzano, A. J. Shapiro, and R. D. Shull, Nature **429**, 853 (2004). 101, 107, 108
- [102] M. P. Annaorazov, K. Barner, and S. Yalcin, J. Alloys Compd. **372**, 52 (2004). 101
- [103] M. P. Annaorazov, M. Unala, S. A. Nikitin, A. L. Tyurin, and K. A. Asatryan, J. Magn. Magn. Mater. **251**, 61 (2002). 101
- [104] L. Caron, Z. Q. Oub, T. T. Nguyen, D. T. CamThanh, O. Tegus, and E. Bruck, J. Magn. Magn. Mater. **321**, 3559 (2009). 102, 103
- [105] M. K. Chattopadhyay and S. B. Roy, J. Phys.: Condens. Matter **20**, 025209 (2008). 103

- [106] M. J. Dapino, in *Encyclopedia of smart materials*, edited by M. Schwartz (John Wiley & Sons, Inc., New York, 2002). 109
- [107] G. Engdahl, ed., *Handbook of giant magnetostrictive materials* (Academic Press, San Diego, 2000). 109
- [108] A. Olabi and A. Grunwald, *Mater. Des.* **29**, 469 (2008). 109
- [109] A. Mavanur, C.-Y. Tai, C. H. Joshi, E. Daly, and K. Davis, *IEEE Trans. Appl. Supercond.* **15**, 2405 (2005). 109
- [110] A. Sozinov, A. A. Likhachev, N. Lanska, and K. Ullakko, *Appl. Phys. Lett.* **80**, 1746 (2002). 109
- [111] P. G. Debenedetti and F. H. Stillinger, *Nature* **410**, 259 (2001). 116, 121, 122, 126, 127
- [112] C. A. Angell, K. L. Ngai, G. B. McKenna, P. F. McMillan, and S. W. Martin, *J. Appl. Phys.* **88**, 3113 (2000). 116
- [113] S. Brawer, *Relaxation in viscous liquids and glasses: Review of phenomenology, molecular dynamics simulations, and theoretical treatment* (American Ceramic Society, Westerville, OH, 1985). 116
- [114] J. K. Kruger, P. Alnot, J. Baller, R. Bactavatchalou, S. Dorosz, M. Henkel, M. Kolle, S. P. Kruger, U. Muller, M. Philipp, et al., in *Ageing and the glass transition*, edited by M. Henkel, M. Pleimling, and R. Sanctuary (Springer, Berlin, 2007), chap. 3. 116
- [115] V. K. Sharma, M. K. Chattopadhyay, and S. B. Roy, *Phys. Rev. B.* **76**, 140401(R) (2007). 116, 121

- [116] S. B. Roy, M. K. Chattopadhyay, P. Chaddah, J. D. Moore, G. K. Perkins, L. F. Cohen, K. A. Gschneidner, Jr., and V. K. Pecharsky, Phys. Rev. B. **74**, 012403 (2006). 116, 121
- [117] P. Chaddah, K. Kumar, and A. Banerjee, Phys. Rev. B **77**, 100402(R) (2008). 116
- [118] S. B. Roy and M. K. Chattopadhyay, Phys. Rev. B. **79**, 052407 (2009). 116, 118
- [119] P. Kushwaha, A. Lakhani, R. Rawat, and P. Chaddah, Phys. Rev. B **80**, 174413 (2009). 116
- [120] J. A. Mydosh, *Spin Glasses* (Taylor & Francis, London, 1992). 117
- [121] S. B. Roy, A. K. Pradhan, P. Chaddah, and B. R. Coles, Solid State Commun. **99**, 563 (1996). 117, 118
- [122] H. Pang, Z. H. Jin, and K. Lu, Phys. Rev. B. **67**, 094113 (2003). 122
- [123] K. Fukao, Y. Miyamoto, and H. Miyajit, J. Phys.: Condens. Matter **3**, 5451 (1991). 122
- [124] A. Cavagna, Phys. Rep. **476**, 51 (2009). 125
- [125] P. A. Sharma, S. El-Khatib, I. Mihut, J. B. Betts, A. Migliori, S. B. Kim, S. Guha, and S.-W. Cheong, Phys. Rev. B. **78**, 134205 (2008). 125
- [126] C. Basire and D. A. Ivanov, Phys. Rev. Lett. **85**, 5587 (2000). 126